

# Quantum transport in bilayer graphene: Fabry-Pérot interferences and proximity-induced superconductivity

Zur Erlangung des akademischen Grades eines  
DOKTORS DER NATURWISSENSCHAFTEN  
durch die Fakultät für Physik  
des Karlsruher Instituts für Technologie

genehmigte

DISSERTATION

von

MPhys. Renjun Du

aus Xi'an, China

Tag der mündlichen Prüfung: 30.10.2015  
Referent: Prof. Dr. Hilbert von Löhneysen  
Korreferent: Prof. Dr. Ralph Krupke



# *Abstract*

Charge carriers in bilayer graphene behave as massive chiral fermions. The peculiar band structure allows to tune the Fermi level within the conduction band or valence band, depending on the applied electrical field. It is possible to form p-n junctions in bilayer graphene. By applying a displacement field, the potentials in the top and bottom layers are modulated independently, resulting in an interlayer asymmetry. As a result, a band gap may open. Furthermore, the unique chirality of charge carriers in bilayers gives rise to anti-Klein tunneling behavior for electrons facing a sharp potential barrier in absence of an interlayer asymmetry.

In this work, we investigate bilayer graphene (BLG) p-n junctions. The devices are made of hBN-BLG-hBN (hexagonal boron nitride) heterostructures, which enables ballistic transport over long distances. Bilayer graphene is connected with two superconducting leads (Ti/Al) from its edges, leading to very transparent metal-graphene interfaces.

Ballistic graphene p-n junctions are ideal Fabry-Pérot interferometers. By analysis of the Fabry-Pérot fringes, we note that the conventional bilayer-like anti-Klein tunneling transits into single-layer-like Klein tunneling when tuning the Fermi level towards the band edges.

The proximity-induced superconductivity has been studied in bilayer graphene p-n junctions. In highly clean samples, a large induced supercurrent can flow through a 1  $\mu\text{m}$  long channel. The corresponding  $I_c R_n$  product depends on the charge carrier density. For example, we obtain  $0.72\Delta/e$  at a density  $2.23 \times 10^{12} \text{ cm}^{-2}$ . The large  $I_c R_n$  product indicates that the S/N interfaces are very transparent, which is attributed to the one-dimensional edge contacts. In the presence of the p-n junctions, the supercurrent is suppressed to a large extent because of the anisotropic transmission probability. Furthermore, at the band edges, the supercurrent is effectively suppressed, which yields an off-state of the superconductivity. By controlling the electrostatic field, we can switch on and off the supercurrent.

## *Kurzzusammenfassung*

Ladungsträger in zweilagigem Graphen (BLG) verhalten sich wie massebehaftete chirale Fermionen. Die besondere Bandstruktur ermöglicht es, das Fermi-Niveau durch ein angelegtes elektrisches Feld zwischen Leitungs- und Valenzband zu verschieben. Dadurch ist es möglich, pn-Übergänge innerhalb des zweilagigen Graphens zu erzeugen. Durch ein senkrecht zur Graphenebene angelegtes Verschiebungsfeld kann das elektrische Potenzial in der oberen und unteren Graphenlage unabhängig voneinander eingestellt werden. Dies führt zu einer Asymmetrie der beiden Lagen, und damit zur Öffnung einer Bandlücke. Des Weiteren ermöglicht die Chiralität der Ladungsträger in zweilagigem Graphen Anti-Klein-Tunneln von Ladungsträgern, die auf eine scharfe Potenzialbarriere treffen.

In dieser Arbeit untersuchen wir pn-Übergänge in zweilagigem Graphen. Die Proben bestehen aus hBN-BLG-hBN-Heterostrukturen, welche ballistischen Transport über lange Distanzen ermöglichen. Das zweilagige Graphen wurde mit supraleitenden Elektroden (Ti/Al) an den Kanten kontaktiert, wodurch ein besonders transparenter Metall-Graphen-Übergang erzielt wurde.

Ballistische Graphenproben mit pn-Übergängen sind ideale Fabry-Pérot-Interferometer. Durch die Analyse der Fabry-Pérot-Interferenzmuster konnten wir feststellen, dass das für zweilagiges Graphen typische Anti-Klein-Tunneln in das für einlagiges Graphen mit Klein-Tunneln erwartete Muster übergeht, wenn das Fermi-Niveau in die Nähe der Bandkante rückt.

Weiterhin wurde durch den Proximity-Effekt induzierte Supraleitung in pn-Übergängen in zweilagigem Graphen untersucht. In sehr sauberen Proben wurde ein Suprastrom über einen bis zu 1  $\mu\text{m}$  langen Kanal beobachtet. Das entsprechende Produkt aus kritischer Stromstärke und Widerstand im normalleitenden Zustand  $I_c R_n$  ist abhängig von der Ladungsträgerdichte. Bei einer Ladungsträgerdichte von  $2.23 \times 10^{12} \text{ cm}^{-2}$  erreichen wir  $0.72\Delta/e$ . Auch dieser relativ hohe Wert von  $I_c R_n$  ist ein Zeichen dafür, dass die Supraleiter-Normalleiter Grenzfläche sehr transparent ist, was wir auf die eindimensionale Kontaktierung an den Kanten zurückführen. Bei Vorhandensein von pn-Übergängen wird der Suprastrom aufgrund der richtungsabhängigen Transmissionswahrscheinlichkeit reduziert und kann sogar - ebenso wie an den Bandkanten - komplett unterdrückt werden. Wir können damit den Suprastrom durch Anlegen von elektrischen Feldern ein- und ausschalten.

# Contents

<b>Abstract</b>	<b>iii</b>
<b>Kurzzusammenfassung</b>	<b>iv</b>
<b>Contents</b>	<b>v</b>
<b>List of Figures</b>	<b>vii</b>
<b>Acknowledgements</b>	<b>ix</b>
<b>Introduction</b>	<b>1</b>
<b>1 Theoretical background</b>	<b>3</b>
1.1 Band structure of single-layer graphene . . . . .	3
1.2 Band structure of bilayer graphene . . . . .	6
<b>2 Experimental methods</b>	<b>11</b>
2.1 Sample fabrication . . . . .	11
2.1.1 Two-dimensional materials preparation and characterization . . . . .	12
2.1.2 Van der Waals assembly process . . . . .	15
2.1.3 Contacting the hBN-graphene-hBN heterostructure . . . . .	18
2.2 Measurement techniques . . . . .	20
<b>3 Fabry-Pérot interference in bilayer graphene p-n-p heterojunctions</b>	<b>23</b>
3.1 Introduction . . . . .	23
3.1.1 Klein tunneling in single-layer graphene . . . . .	24
3.1.2 Anti-Klein tunneling in bilayer graphene . . . . .	28
3.1.3 Berry phase in single-layer and bilayer graphene . . . . .	30
3.1.3.1 Berry phase in single-layer graphene and gapless bilayer graphene . . . . .	30
3.1.3.2 Berry Phase in gapped bilayer graphene . . . . .	33
3.2 Sample description . . . . .	33
3.3 Electrical transport in bilayer graphene p-n junctions . . . . .	35
3.3.1 Electrostatic model . . . . .	38
3.3.2 Interlayer asymmetry in bilayer graphene . . . . .	39
3.3.3 Contact resistance for one-dimensional edge contacts . . . . .	40

3.4	Fabry-Pérot interference in ballistic bilayer graphene p-n-p junctions . . .	41
3.5	Fabry-Pérot oscillations at low magnetic fields . . . . .	48
3.6	Conclusion . . . . .	50
<b>4</b>	<b>Proximity-induced superconductivity in bilayer graphene p-n-p junctions</b>	<b>51</b>
4.1	Introduction to proximity-induced superconductivity . . . . .	51
4.1.1	Josephson effect . . . . .	51
4.1.2	The resistively and capacitively shunted junction model . . . . .	53
4.1.3	Fraunhofer diffraction pattern . . . . .	55
4.1.4	Andreev reflection . . . . .	57
4.1.5	Blonder-Tinkham-Klapwijk (BTK) theory . . . . .	58
4.1.6	Multiple Andreev reflection . . . . .	62
4.1.7	Andreev reflection in magnetic field . . . . .	64
4.1.8	Proximity-induced superconductivity in graphene . . . . .	65
4.2	Normal state resistance . . . . .	68
4.3	Ballistic Josephson current in S-BLG-S junctions . . . . .	70
4.4	Multiple Andreev reflections . . . . .	72
4.5	$I_c R_n$ product . . . . .	75
4.6	Temperature dependence of the supercurrent . . . . .	76
4.7	Critical current oscillations due to the Fabry-Pérot interference . . . . .	77
4.8	Switching off the supercurrent . . . . .	77
4.9	Fraunhofer diffraction pattern . . . . .	80
4.10	Resistance peaks above $2\Delta$ . . . . .	83
4.11	Conclusion . . . . .	86
	<b>Conclusions</b>	<b>86</b>
	<b>A Matlab codes for calculating angular transmission probabilities in bilayer graphene</b>	<b>89</b>
	<b>B Matlab codes for extracting the Josephson current density</b>	<b>95</b>
	<b>Bibliography</b>	<b>99</b>

# List of Figures

1.1	Crystal lattices of single-layer graphene . . . . .	4
1.2	Band structure of single-layer graphene . . . . .	5
1.3	An example of ambipolar transports in graphene . . . . .	6
1.4	Crystal lattices of bilayer graphene . . . . .	7
1.5	Band structure of bilayer graphene . . . . .	8
1.6	Opening of a band gap in bilayer graphene . . . . .	9
2.1	Two-dimensional materials obtained by mechanical exfoliation . . . . .	13
2.2	Comparison of Raman spectra for monolayer graphene, bilayer graphene and graphite . . . . .	13
2.3	AFM images of a rough and an atomically smooth hBN surface . . . . .	14
2.4	Van der Waals assembly process of a hBN-graphene-hBN heterostructure	16
2.5	Transfer set-up . . . . .	17
2.6	A hBN-graphene-hBN heterostructure after thermal annealing . . . . .	17
2.7	The process of one-dimensional edge-contact fabrication . . . . .	18
2.8	AFM images of two p-n-p junctions made of hBN-BLG-hBN heterostruc- tures . . . . .	19
2.9	The improved method for making edge contacts . . . . .	20
2.10	Diagram of measurement circuit . . . . .	21
3.1	A sketch of a sharp potential barrier created by dual-gates in the npn regime . . . . .	25
3.2	The angular transmission probabilities in single-layer graphene for a sharp potential barrier . . . . .	26
3.3	The angular transmission probabilities in single-layer graphene for a smooth potential barrier . . . . .	27
3.4	The transmission probabilities as a function of the electron incident angle in bilayer graphene . . . . .	29
3.5	Sketch of a polarization vector on a Bloch sphere . . . . .	31
3.6	Pseudospin projections of electrons along the constant energy contours in single-layer and bilayer graphene . . . . .	32
3.7	Pseudospin in gapped bilayer graphene . . . . .	33
3.8	Sample description of bilayer graphene p-n-p junctions . . . . .	34
3.9	Characteristic of a bilayer graphene p-n-p junction . . . . .	37
3.10	Resistance versus top-gate voltage for various back-gate voltages . . . . .	40
3.11	Fabry-Pérot interferences observed in conductance measurements . . . . .	42
3.12	The potential profiles and the band diagrams in the cases of different charge polarity combinations . . . . .	44
3.13	Conductance oscillations in the pnpn regime measured on sample BL12D	46

3.14	The periods of conductance oscillations in the bipolar regime . . . . .	47
3.15	Effect of low magnetic fields on Fabry-Pérot oscillations at 4.2 K . . . . .	49
3.16	The angular transmission probability for a sharp potential . . . . .	49
4.1	Sketch of a Josephson junction . . . . .	52
4.2	Equivalent circuit for the resistively and capacitively shunted junction (RCSJ) model . . . . .	53
4.3	The damped motion of a quasiparticle in the tilted washboard potential . . . . .	54
4.4	The hysteresis behaviour of the $I - V$ curves for various $\beta_C$ . . . . .	55
4.5	Sketch of Fraunhofer diffraction pattern in an extended Josephson junction . . . . .	56
4.6	The schematics of a Andreev reflection process . . . . .	58
4.7	The reflection and transmission coefficient at the N/S interface for various barrier strength $Z$ . . . . .	60
4.8	Current versus voltage for various barrier strength $Z$ at zero temperature . . . . .	61
4.9	The process of multiple Andreev reflection in a SNS junction . . . . .	63
4.10	The differential resistance versus $eV/\Delta$ simulated for various temperatures . . . . .	63
4.11	Andreev reflection in magnetic fields . . . . .	64
4.12	Andreev reflection in graphene . . . . .	66
4.13	Bipolar supercurrent . . . . .	67
4.14	Resistance as a function of $V_{tg}$ and $V_{bg}$ at the normal state . . . . .	69
4.15	Supercurrent tuned by dual-gates for sample BL12C . . . . .	71
4.16	Simulation using RCSJ model for the voltage-current relation . . . . .	72
4.17	Excess current and subharmonic gap structure . . . . .	74
4.18	The normalized $I_c R_n$ product $eI_c R_n/\Delta$ tuned by the back-gate voltage $V_{bg}$ and the top-gate voltage $V_{tg}$ . . . . .	75
4.19	Temperature dependence of the supercurrent . . . . .	76
4.20	Critical current oscillations originating from Fabry-Pérot interferences . . . . .	77
4.21	The color scaled plots of Resistances as a function of $V_{tg}$ and $V_{bg}$ . . . . .	78
4.22	Sketch for the specular-like Andreev reflection near Dirac point . . . . .	79
4.23	Suppression of the supercurrent in the band gap . . . . .	80
4.24	Fraunhofer diffraction pattern . . . . .	81
4.25	The evolution of the subharmonic gap structures in the low magnetic field . . . . .	82
4.26	The critical current density along the junction . . . . .	83
4.27	The $I - V$ curve and the corresponding differential resistance measured for the sample BL12C . . . . .	83
4.28	The differential resistance as a function of the magnetic field and the voltage for the sample BL12C . . . . .	84
4.29	Highly resistive peaks above $2\Delta$ in differential resistance versus voltage curves . . . . .	85
4.30	The schematics of the Tomasch resonances and the McMillan-Rowell resonances . . . . .	86

# *Acknowledgements*

In 2011, I have been very lucky to get a grant from the Chinese Scholarship Council to do my PhD in Karlsruhe. I have studied in Institute of Nanotechnology for four years. At this moment, things happened in the last four year come back to my mind. I'm very grateful to people I have met in Karlsruhe and to all their help.

I appreciate very much that Prof. Dr. Hilbert v. Löhneysen gave me the opportunity to study under his supervision. His instructions helped me improve myself on the scientific research.

I would like to thank Prof. Dr. Ralph Krupke to be the second referee of my PhD thesis. I also enjoy the weekly unit meeting very much. The view points that he has shared with us opened my mind.

I appreciate Prof. Dr. Matthias Steinhauser for being my mentor. I have attended his Quantum Mechanics lectures, which helped me to understand more deeply my PhD topics.

I'm very grateful to Dr. Romain Danneau for teaching me in the past four years. He brought me to the interesting graphene world. I enjoyed all the time that we worked together.

I would like to thank my dear colleagues, Jens, Fan, Christian, Julien, Pablo, Rainer, Nicolai, Nicolas, Pranaav, Ruby, Nayancee, Wenshan, for their company, and help. I enjoyed the happy time with them no matter in working hours or after work.

I appreciate very much the support from my dear husband. He encouraged me to overcome all the difficulties.

I thank my parents for their love. They give me the best in the world. They are wonderful parents.



# Introduction

Graphene is a single-layer of carbon atoms arranged in hexagonal lattice, which is the building block of graphite. This two-dimensional material has been studied theoretically by P. R. Wallace [1] in 1947. However, the first isolated graphene has been found much later by A. Geim and K. Novoselov in 2004 [2, 3]. The experimental investigations on graphene show that the charge carriers can be tuned continuously between electrons and holes up to high densities of  $\sim 10^{13} \text{ cm}^{-2}$ . The mobility can exceed  $200,000 \text{ cm}^2\text{V}^{-1}\text{s}^{-1}$  at charge carrier densities of  $\sim 2 \times 10^{11} \text{ cm}^{-2}$  on suspended graphene devices [4]. The extraordinary electronic properties make graphene popular to investigate the ambipolar electric field effect [5, 6]. In condensed-matter physics, graphene is an unusual material, in which the charge carriers mimic the behavior of relativistic particles, which can be described by Dirac equations [7]. Therefore, some quantum relativistic phenomena, like Klein tunneling which has been theoretically predicted in high-energy physics, can now be probed in graphene [8].

Bilayer graphene (BLG) consists of two coupled layers of graphene on top of each other. Thus, both intralayer and interlayer transport is possible in bilayer graphene [9]. More importantly, compared to single-layer graphene (SLG), which is gapless, a band gap can be opened in bilayer by “simply” applying a displacement field, which induces an asymmetry between the two layers [10]. The presence of an induced band gap may strongly influence the quantum Hall regime [11] or quantum interference [12].

Despite the remarkable transport properties, it is challenging to obtain a pristine graphene sheet without disorder in experiments. Great efforts have been made in the last decade to improve the quality of the samples. Hexagonal boron nitride (hBN) has been found as a good substrate material for graphene, allowing to preserve its intrinsic properties [13]. Wang et. al. [14] have improved the technique to encapsulate graphene between two hBN multilayers, leading to an enhancement of the sample quality. This technique renews the life of graphene and enables us to investigate transport properties in ballistic regime for large scale samples.

In this work, we follow the sample fabrication method of Wang et. al. [14] in order to obtain high quality devices, which are based on bilayer graphene heterostructures. Bilayer graphene p-n junctions have been fabricated and their transport properties will be discussed in the following.

In Chapter 1, we introduce the theoretical background, band structure, of the single-layer and bilayer graphene based on the tight-bonding model [1, 9]. In particular, the band spectrum at low energies are most interested. We also discuss the theoretical background about the Landau levels of bilayer graphene.

In Chapter 2, we describe the sample fabrication procedure, in particular, the van der Waals assembly process, which allows us to make clean devices. The electrical measurement techniques at low temperatures are also described in details.

In Chapter 3, we discuss the normal-state properties for bilayer graphene p-n junctions. The devices possess the configuration of Fabry-Pérot interferometers, which are useful tools to detect the fundamental phenomena, such as Klein tunneling in monolayer graphene [8]. Here, we first introduce Klein tunneling in monolayer graphene, anti-Klein tunneling in bilayer graphene as well as the respective Berry phase. Then, we present our measurement results on Fabry-Pérot interference and discuss anti-Klein tunneling, especially when the interlayer symmetry between the top and bottom layers are broken.

In Chapter 4, we investigate the proximity-induced superconductivity in bilayer graphene devices. The supercurrent is measured at zero and the low magnetic field ( $< 10$  mT), respectively. The interlayer asymmetry makes that the superconductivity in bilayer graphene is of great interest. The reaction of supercurrent on the band gap is discussed. Furthermore, anti-Klein tunneling at the normal states results in the selective transmission probabilities. As a result, this affects the phase-coherent transport of Andreev bound states.

# Chapter 1

## Theoretical background

In this chapter, we introduce the basics of graphene. First of all, we present the band structures of single-layer and bilayer graphene at low energies. Then we discuss the Landau levels of bilayer graphene in two situations: with and without the interlayer asymmetry.

### 1.1 Band structure of single-layer graphene

Graphene is a single layer of carbon atoms arranged in a honeycomb lattice. The crystal structure is shown in Figure 1.1a.  $\mathbf{a}_1$  and  $\mathbf{a}_2$  are the primitive lattice vectors, which are defined as

$$\mathbf{a}_1 = \left( \frac{\sqrt{3}a}{2}, \frac{a}{2} \right), \quad \mathbf{a}_2 = \left( \frac{\sqrt{3}a}{2}, -\frac{a}{2} \right), \quad (1.1)$$

where  $a = |\mathbf{a}_1| = |\mathbf{a}_2| = 2.46 \text{ \AA}$  is the lattice constant. The distance between two adjacent carbon atoms is  $a_{AB} = a/\sqrt{3} = 1.42 \text{ \AA}$ . In graphene, each unit cell consists of two carbon atoms, which are non-equivalent in positions and therefore labeled as A and B sublattices. The strong in-plane  $\sigma$  bonds, formed by the  $sp^2$  hybridization of the valence electron orbitals  $p_x$ ,  $p_y$  and  $s$ , are responsible for the stability of graphene, but not for the electronic transport. The remaining electron with the  $p_z$  orbital forms the delocalized, covalent bond with its neighboring atoms, which makes up the  $\pi$  band. Each carbon atom contributes one electron to the  $\pi$  bands. Thus, a unit cell contains two valence electrons. The  $\pi$  band determines the electronic properties of graphene.

The reciprocal lattice of graphene is a hexagonal Bravais lattice, as shown in Figure 1.1b. The primitive reciprocal lattice vector are given by

$$\mathbf{b}_1 = \left( \frac{2\pi}{\sqrt{3}a}, \frac{2\pi}{a} \right), \quad \mathbf{b}_2 = \left( \frac{2\pi}{\sqrt{3}a}, -\frac{2\pi}{a} \right). \quad (1.2)$$

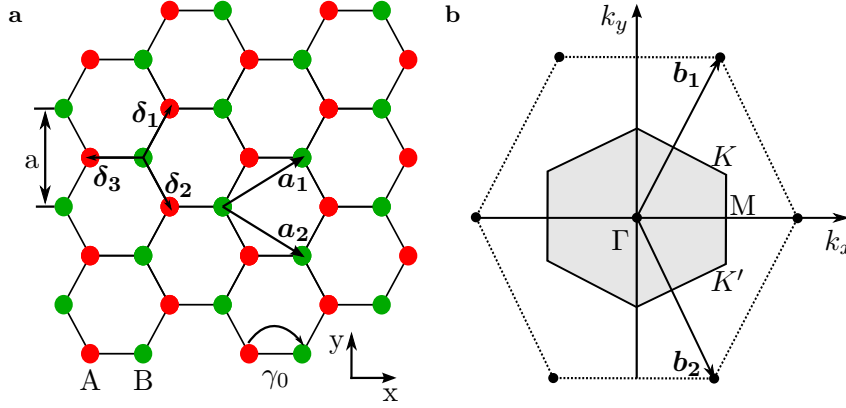


**Figure 1.1:** Crystal lattices of single-layer graphene (a) and the corresponding reciprocal lattice (b).  $\mathbf{a}_1$  and  $\mathbf{a}_2$  are the primitive lattice vectors.  $\mathbf{b}_1$  and  $\mathbf{b}_2$  are the primitive reciprocal lattice vectors. The shaded region in (b) indicates the first Brillouin zone. The center is labeled as  $\Gamma$ .  $K$  and  $K'$  are two non-equivalent corners.

The two non-equivalent points  $K$  and  $K'$ , located at the corners of the first Brillouin zone, are the Dirac points of graphene.

The band structure of graphene is approximately calculated by the tight-binding model [1]. Within the nearest-neighbor hopping approximation, the Hamiltonian can be expressed in the basis of the wavefunction amplitudes on the A and B sublattices,  $(\Psi_A, \Psi_B)$ , that is

$$H = -\gamma_0 \begin{pmatrix} 0 & \sum_j e^{i\mathbf{k}\cdot\delta_j} \\ \sum_j e^{-i\mathbf{k}\cdot\delta_j} & 0 \end{pmatrix}, \quad (1.3)$$

where  $\gamma_0 \approx 3.16$  eV is the nearest hopping parameter in the lattice plane,  $\mathbf{k}$  is an arbitrary wave vector in the Brillouin zone, and  $\delta_j$  are the vectors connecting the nearest neighbors, i.e.

$$\delta_1 = \frac{a}{2} \left( \frac{1}{\sqrt{3}}, 1 \right), \quad \delta_2 = \frac{a}{2} \left( \frac{1}{\sqrt{3}}, -1 \right), \quad \delta_3 = \frac{a}{2} \left( -\frac{2}{\sqrt{3}}, 0 \right). \quad (1.4)$$

The corresponding eigenvalues are given by

$$E(k_x, k_y) = \pm \gamma_0 \sqrt{3 + 4 \cos \left( \frac{\sqrt{3}ak_x}{2} \right) \cos \left( \frac{ak_y}{2} \right) + 2 \cos(ak_y)}. \quad (1.5)$$

The plus and minus signs represent the conduction and valence bands, respectively.

The energy band spectrum of single-layer graphene is depicted in Figure 1.2a. The cosine-like conduction and valence bands are symmetric, and connected at the Dirac points. The conduction (or valence) band exhibits six valleys at the corners of the first Brillouin zone. The energy bands exhibit conical structures near the Dirac points. The

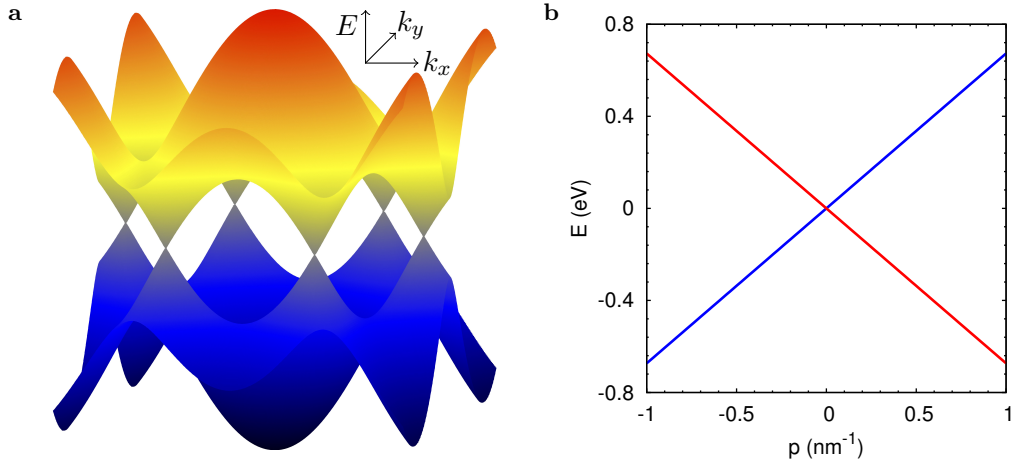


**Figure 1.2:** Band structure of single-layer graphene calculated with the tight-binding model. (a) The description of the  $\pi$ -bands. The band structure exhibits a large gap at the  $\Gamma$  point, but gapless at the corners of Brillouin zone. (b) The linearly dispersed energies around the  $K$  and  $K'$  points. The low-energy spectrum consists of two branches, denoted as red and blue curves, respectively.

eigenvalues are degenerate at the Dirac points, i.e.  $E_{\pm}(K) = E_{\pm}(K') = 0$ , which is due to the inversion symmetry of the honeycomb lattice.

In the low-energy range, the Hamiltonian of Equation (1.3) can be expanded with respect to the  $K$ -points by introducing a momentum  $\mathbf{p} = \hbar\mathbf{k} - \hbar\mathbf{K}$ , that is

$$H = v_F \boldsymbol{\sigma} \cdot \mathbf{p}. \quad (1.6)$$

Here,  $v_F = \frac{\sqrt{3}a\gamma_0}{2\hbar}$  is the Fermi velocity,  $\boldsymbol{\sigma} = (\sigma_x, \sigma_y)$  is the vector of the Pauli matrices

$$\sigma_x = \begin{pmatrix} 0 & i \\ -i & 0 \end{pmatrix} \quad \sigma_y = \begin{pmatrix} 0 & 1 \\ 1 & 0 \end{pmatrix} \quad \sigma_z = \begin{pmatrix} 1 & 0 \\ 0 & -1 \end{pmatrix}. \quad (1.7)$$

The energy dispersion is linear at low energies, which is given by

$$E(p) = \pm v_F |\mathbf{p}|. \quad (1.8)$$

As shown in Figure 1.2b, the band structure consists of two linear branches (denoted in red and blue, respectively), which originate from the sublattices A and B, respectively.

In single-layer graphene, the Hamiltonian of Equation (1.6) is formally identical to the Dirac Hamiltonian for relativistic electrons [15]. From the linear dispersion relation (Equation (1.8)), we note that quasiparticles in graphene behave as massless relativistic particles with momentum  $\mathbf{p}$ . Here, the Fermi velocity  $v_F \approx c/300$  plays the role of the speed of light. The quasiparticles in graphene are described by two-component

wavefunctions ( $\Psi_A, \Psi_B$ ), which take the contributions from the two sublattices A and B into consideration. This description resembles that of by spinor wavefunctions in quantum electrodynamics. But the role of spin is played by the two sublattices A and B rather than the real spin of electrons. Therefore,  $\sigma$  is not the spin and is referred to as pseudospin. The momentum is coupled to the pseudospin, which points in the same direction for electrons and holes belonging to the same branch of the energy spectrum. The pseudospin is parallel to the momentum for electrons but antiparallel for holes, leading to the positive and negative chirality for electrons and holes, respectively.

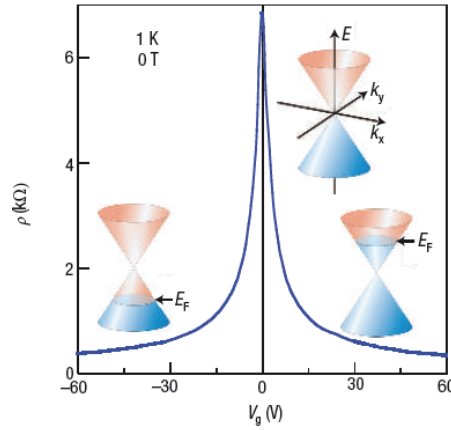


**Figure 1.3:** An example of ambipolar transports in graphene. Resistances vary with respect to back-gate voltages for single-layer graphene. The charge carriers can be electrons or holes by tuning the gate. Figure from Ref. [16].

Graphene can be viewed as a semimetal. The Fermi level may be tuned from the conduction band to the valence band; hence, the charge carriers can be electrons or holes [16], as shown in Figure 1.3. At the Dirac point, the minimum conductivity is finite,  $4e^2/h$  [16, 17], which comes from the random network of charge puddles at low charge carrier density. In ideal graphene, the minimum conductivity is  $\frac{4e^2}{\pi h}$  for width over length ratio  $W/L > 3$  [18]. Moreover, the peculiar chirality of charge carriers in graphene gives rise to Klein tunneling behavior when a charge carrier faces a sharp potential [8]. At high magnetic fields, graphene exhibits the integer quantum Hall effect, but the quantized conductivity plateaus appear at the half-integer of  $4e^2/h$  due to the Berry phase of  $\pi$  [3, 19]. The Klein tunneling and Berry phase are presented in more detail in Chapter 3.

## 1.2 Band structure of bilayer graphene

Bilayer graphene consists of two coupled monolayer graphene sheets. In Bernal stacked bilayer graphene, shown in Figure 1.4, the top layer is rotated  $60^\circ$  with respect to the

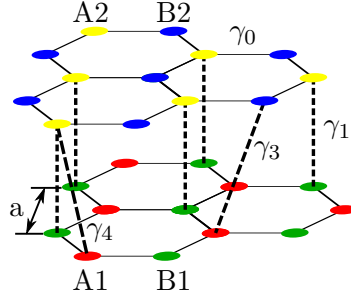


**Figure 1.4:** Crystal lattices of bilayer graphene.

bottom one. A unit cell contains four carbon atoms, which are labeled by A1, B1 on the bottom layer and A2, B2 on the top layer. The A2 sublattice sites directly on top of the B1 sublattice, resulting in a relatively strong interlayer coupling. As a result, the two atomic sites form ‘dimer’ sites. The other two atoms are referred to as ‘non-dimer’ sites. The tight-binding approach is employed to calculate the band structure of bilayer graphene [9]. In the basis  $(\Psi_{A1}, \Psi_{B1}, \Psi_{A2}, \Psi_{B2})$ , the effective four-band Hamiltonian at low energy is written as

$$H = \begin{pmatrix} -\frac{u}{2} & v\pi^\dagger & -v_4\pi^\dagger & v_3\pi \\ v\pi & -\frac{u}{2} & \gamma_1 & -v_4\pi^\dagger \\ v_4\pi & \gamma_1 & \frac{u}{2} & v\pi^\dagger \\ v_3\pi^\dagger & v_4\pi & v\pi & \frac{u}{2} \end{pmatrix}, \quad (1.9)$$

where  $\pi = p_x + ip_y$ ,  $\pi^\dagger = p_x - ip_y$ ,  $v = \frac{\sqrt{3}a\gamma_0}{2\hbar}$  is the band velocity,  $v_3 = \frac{\sqrt{3}a\gamma_3}{2\hbar}$  and  $v_4 = \frac{\sqrt{3}a\gamma_4}{2\hbar}$  are the effective velocities,  $\gamma_i$  are the tight-binding parameters for graphite [9], and  $u$  is the interlayer asymmetry parameter, which describes the difference in electrostatic potentials between the two layers.  $u$  can be numerically calculated according to Equation (3.29). Similarly to the case of monolayer graphene,  $\gamma_0$  represents the intralayer coupling between electronic orbitals, i.e.  $\gamma_0 = \gamma_{A1B1} = \gamma_{A2B2} \sim 3.16$  eV [20].  $\gamma_1$  represents the interlayer coupling between the ‘dimer’ sites, i.e.  $\gamma_1 = \gamma_{A2B1} \sim 0.381$  eV [20]. This term results in the largest difference between bilayer graphene and monolayer graphene. The interlayer coupling between the two ‘non-dimer’ sites is represented by  $\gamma_3 = \gamma_{A1B2} \sim 0.315$  eV [21]. The term  $\gamma_3$  generates the trigonal warping only at very low energies [9]. The  $v_4\pi$  term is proportional to  $\gamma_4$ , which represents the interlayer coupling between the ‘dimer’ and ‘non-dimer’ orbitals, A1 and A2 or B1 and B2. In the following, we neglect the influence of the  $\gamma_3$  and  $\gamma_4$  terms in order to focus on a minimal model, which is sufficient to understand the experiments in this thesis. The Hamiltonian of Equation

(1.9) is then described as

$$H = \begin{pmatrix} -\frac{u}{2} & v\pi^\dagger & 0 & 0 \\ v\pi & -\frac{u}{2} & \gamma_1 & 0 \\ 0 & \gamma_1 & \frac{u}{2} & v\pi^\dagger \\ 0 & 0 & v\pi & \frac{u}{2} \end{pmatrix}. \quad (1.10)$$

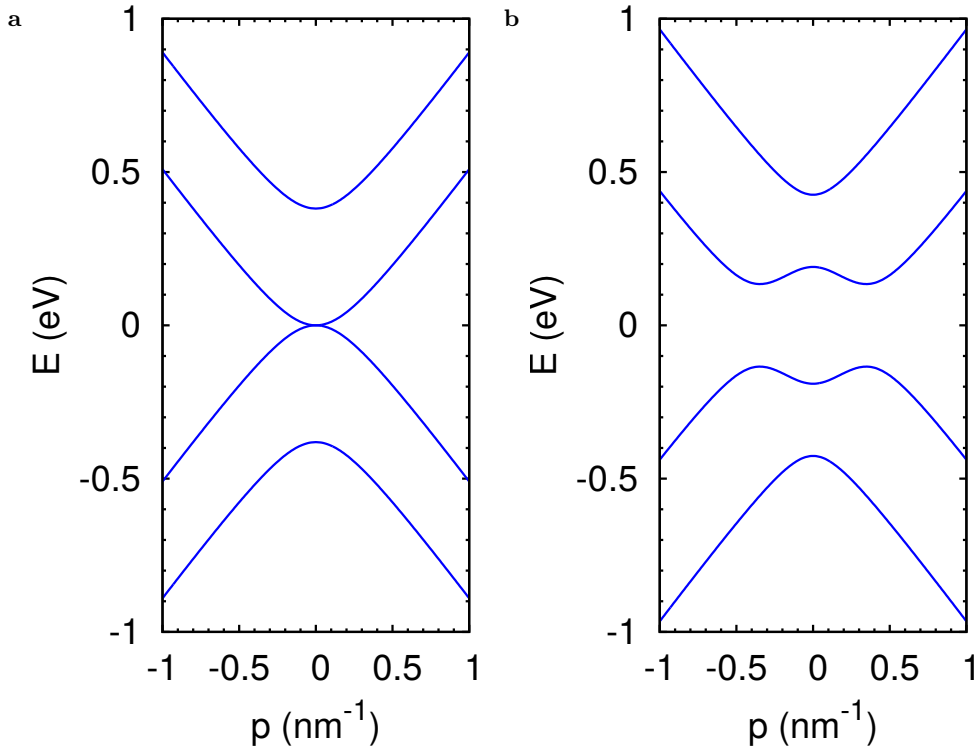


**Figure 1.5:** Band structures of bilayer graphene near a Brillouin zone corner for  $u = 0$  (a) and  $u \neq 0$  (b).  $u$  is chosen to be  $\gamma_1$  in (b).

It is found that the band structure of bilayer graphene is linear at high energies. However, the interlayer hopping parameter  $\gamma_1$  and asymmetry parameter  $u$  strongly affect the band structure at low energies. Considering the simplified Hamiltonian of Equation (1.10), the energies  $E = \pm\varepsilon_\alpha(\mathbf{p})$  ( $\alpha = 1, 2$ ) obey the following relation

$$\varepsilon_\alpha^2 = \frac{\gamma_1^2}{2} + \frac{u^2}{4} + v^2 p^2 + (-1)^\alpha \sqrt{(vp)^2(\gamma_1^2 + u^2) + \frac{\gamma_1^4}{4}}. \quad (1.11)$$

$E = \pm\varepsilon_1$  describes the low-energy bands, which are associated with the ‘non-dimer’ sites A1, B2. While  $E = \pm\varepsilon_2$  describes the higher energy bands that are split from zero energy by the interlayer coupling  $\gamma_1$ . The band structure for  $u = 0$  and  $u \neq 0$  are portrayed in Figure 1.5a and Figure 1.5b, respectively. In the case of  $u = 0$ , the role of  $\gamma_1$  is revealed by introducing the parabolic energy-momentum dispersion close to the  $K$  point. The other effect of  $\gamma_1$  is found in the formation of the two split bands, which are associated with the ‘dimer’ sites. When applying an electrical field perpendicular to the lattice

plane, a finite asymmetry parameter is induced to the system,  $u \neq 0$ . The low-energy bands exhibit a ‘Mexican hat’ shape with a band gap between the conduction and valence bands. The experiments are usually carried out at low energies, i.e.  $|E|, |u| \ll \gamma_0, \gamma_1$ . Hence, it is useful to describe the bilayer in the low energy range. By eliminating the components related to the dimer sites in Hamiltonian of Equation (1.10), one obtains an effective two-band Hamiltonian in the basis  $(\Psi_{A1}, \Psi_{B2}, \Psi_{A2}, \Psi_{B1})$ , that is

$$H_2 = \begin{pmatrix} -\frac{u}{2} \left(1 - \frac{\pi^\dagger \pi}{m\gamma_1}\right) & -\frac{(\pi^\dagger)^2}{2m} \\ -\frac{\pi^2}{2m} & \frac{u}{2} \left(1 + \frac{\pi\pi^\dagger}{m\gamma_1}\right) \end{pmatrix}, \quad (1.12)$$

where the effective mass  $m = \gamma_1/2v^2$ . The eigenvalues of  $H_2$  is

$$E = \pm \sqrt{\left(\frac{p^2}{2m}\right)^2 + \left(\frac{u}{2}\right)^2}. \quad (1.13)$$

One can notice that  $H_2$  resembles to the Dirac-like Hamiltonian of single-layer graphene but with off-diagonal terms that are quadratic in momentum [9]. Therefore, charge carriers in bilayer graphene are massive chiral fermions. The corresponding wave function in the case of  $u = 0$  is expressed as

$$\Psi = \frac{1}{\sqrt{2}} \begin{pmatrix} 1 \\ \mp e^{2i\phi} \end{pmatrix} e^{i\mathbf{p}\cdot\mathbf{r}/\hbar}. \quad (1.14)$$

As in monolayer graphene, the charge carriers in bilayer can be controlled by changing

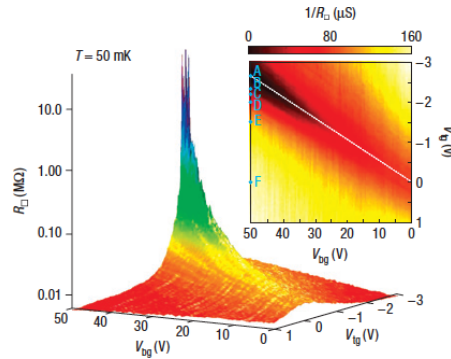


**Figure 1.6:** Opening of a band gap in bilayer graphene by applying a displacement field. Figure from Ref. [10].

the Fermi level. However, by applying a displacement field using top and back gates, it is possible to break the symmetry between the top and bottom layers in bilayer graphene, leading to the opening of a band gap [10, 22, 23]. Figure 1.6 shows an example of the band gap opening in bilayer graphene, which have been observed by Oostinga et. al. [10]. An insulating state has been reached. It is important to note that the symmetry of the system can also be broken by chemical doping [24].



## Chapter 2

# Experimental methods

The fabrication techniques, especially the transfer methods, for graphene samples have been greatly improved in the last decade. As a result, ballistic transport in large scale graphene can now be realized, e.g. a mean free path of 15  $\mu\text{m}$  has been obtained at low temperature, e.g.  $T=1.7$  K, by Wang et. al. [14]. In the following, we present a sample fabrication approach which is based on the assembly of two-dimensional materials linked by van der Waals (vdW) forces. The transport properties of graphene bilayers-hBN vdW heterostructures are probed at low temperatures (below 4 K). Details of the electrical set-up are then described.

### 2.1 Sample fabrication

One of the prominent properties of graphene is the high carrier mobility, which may exceed  $200,000 \text{ cm}^2\text{V}^{-1}\text{s}^{-1}$  on suspended devices [4]. However, this property cannot be preserved for graphene samples on  $\text{SiO}_2$  substrates because of the strong scattering from charged surface states and impurities, substrate surface roughness and optical phonons. It is also a challenge to realize various functions of graphene devices with suspended architectures. In addition, suspended graphene nanostructures are delicate to fabricate and extremely fragile. A proper dielectric, hexagonal boron nitride(hBN), is used as an alternative to  $\text{SiO}_2$ , which allows to fabricate substrates supported graphene devices without sacrificing the high mobilities. This is because the atomically smooth surface of hBN is relatively free of dangling bonds and surface charge traps, and the surface optical phonon modes of hBN have energies two times higher than similar modes of  $\text{SiO}_2$ , which indicates an improvement of the device performance at high-temperature and high-electric field [13].

Graphene-hBN devices are fabricated by manually transferring graphene from the supported substrate on the surface of hBN that is located on another substrate. Despite the advantages of hBN as dielectric, new problems are introduced during the graphene transfer process. One of the most severe problems is the chemical contamination from polymers, such as polymethyl methacrylate (PMMA), methyl methacrylate (MMA) and polydimethylsiloxan (PDMS), which are used as supporting mask during the transfer process. Those polymers cannot dissolve completely in a solvent such as acetone, chloroform, isopropanol, causing a layer of chemical residues on the surface of graphene. It is hard to remove the chemical residues although many attempts were performed in the past, such as thermal annealing in Ar/H<sub>2</sub> atmosphere, mechanical cleaning with atomic force microscope (AFM), or current annealing in vacuum. Another problem is that, because strain develops between graphene and hBN during depositing, wrinkles and bubbles appear on graphene after the transfer. These defects can degrade the mobility and prevent from the study of the fundamental physics of graphene.

To solve the above mentioned problems, we develop a new layer assembly method which was first proposed by Wang et. al. [14]. This method is based on the van der Waals adhesion between two-dimensional materials.

### 2.1.1 Two-dimensional materials preparation and characterization

The sample is fabricated on a p-doped Si substrate with 300-nm thermally grown SiO<sub>2</sub>. The Si substrate is first cleaned with acetone and isopropanol using ultrasonic bath in order to get rid of chemical contaminants. Then a soft O<sub>2</sub> plasma is applied to clean the rest of the surface contaminants with the following parameters: 10 sccm O<sub>2</sub>, RF power 30 W, pressure 100 mTorr, and duration 5 min. Since the substrate becomes hydrophilic after the O<sub>2</sub> plasma treatment, it is baked above 100 °C in air to evaporate water molecules accumulated on the surface right before mechanical exfoliation.

The graphene flakes are exfoliated from natural graphite crystals on the surface of Si/SiO<sub>2</sub> substrates by the scotch tape technique [16]. The clean graphite flakes are cleaved with a piece of scotch tape from the bulk graphite. The thickness of those flakes are then reduced by cleaving with another tape. When the graphite flakes become translucent, we place that part on top of a substrate and press for one minute. After removing the tape, a number of graphite flakes randomly spread on the substrate. Monolayer and bilayer graphene sheets are of a small minority (a five percent) amongst thicker flakes.

Despite the fact that monolayer graphene (MLG) is difficult to observe in an optical microscope on most substrates, it becomes visible on Si substrates with 300-nm SiO<sub>2</sub> owing

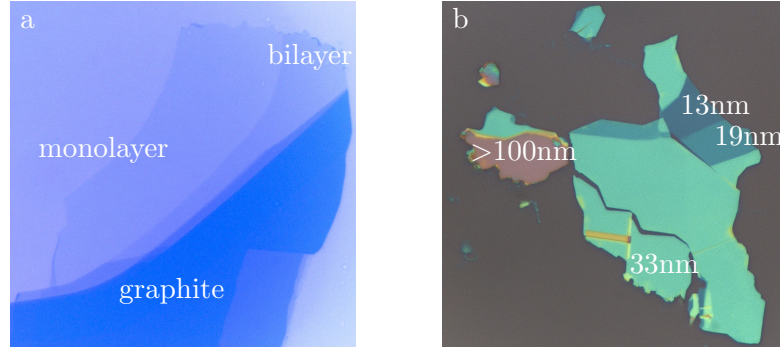


**Figure 2.1:** Two-dimensional materials obtained by mechanical exfoliation: (a) Optical image of monolayer graphene, bilayer graphene and graphite. (b) The color difference of hBN flakes with different thickness, which is measured with AFM.

to a change of interference color with respect to uncovered sections of the substrates [25]. Figure 2.1a shows monolayer and bilayer graphene (BLG) which are identified by the optical contrast. The position of the graphene flake is located by the markers patterned on the substrates. By means of mechanical exfoliation, about 100  $\mu\text{m}$  long graphene strips are achievable, which allows us to realize various devices for our investigations.

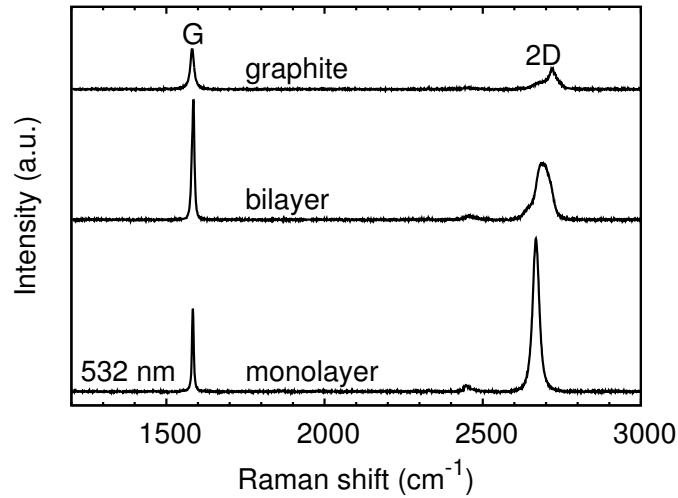


**Figure 2.2:** Comparison of Raman spectra for monolayer graphene, bilayer graphene and graphite. Laser wavelength 532 nm, power 2.5 mW, measurement duration 20 s.

Graphene has a remarkable signature in Raman microscopy, which makes this characterization technique a fast and non-destructive tool [26, 27]. Figure 2.2 shows the typical Raman spectra for exfoliated graphene samples on Si/SiO<sub>2</sub> substrates. The samples are characterized at room temperature in ambient condition using a RENISHAW inVia Raman spectrometer at a wave length of 532 nm. The laser is focused by a 100 $\times$  objective, allowing precise measurement with a spot size of  $\sim 1 \mu\text{m}^2$ . We use an incident power of 2.5 mW to avoid overheating or damaging the samples. The Rayleigh scattering is suppressed by using notch filters. Two prominent peaks are observed in Figure 2.2. One is

at  $\sim 1580 \text{ cm}^{-1}$ , called G peak, associated with the doubly degenerate  $E_{2g}$  phonon mode at zone center  $\Gamma$ . It is the first-order Raman scattering process governed by the fundamental Raman selection rule. On the contrary, another peak at  $\sim 2700 \text{ cm}^{-1}$ , named 2D peak, corresponds to an intervalley double-resonance Raman process at the zone boundary, which does not satisfy the fundamental Raman selection rule. The double-resonance process is directly linked to the details of the electronic band structure of graphene which changes with increasing the number of layers and the stacking order. As a result, there is only one possible intervalley double resonance process along the  $\Gamma - K - M - K' - \Gamma$  direction in MLG resulting in a single component of the 2D peak, whereas the observed four components of the 2D peaks in Bernal-stacked bilayer graphene come from the four possible double resonance processes due to the splitting of the electronic bands near the  $K$  ( $K'$ ) point [26]. The D peak at  $\sim 1350 \text{ cm}^{-1}$  caused by double resonance of electronic states with one phonon and one defect is missing, indicating the high quality of our flakes.

By comparison of the Raman spectra of MLG, BLG with graphite, MLG and BLG can be clearly distinguished from multi-layer graphite by the shape, width, position and intensity of the 2D peak. In case of MLG, we observe a sharp 2D peak with an intensity at least two times of the G peak. On the contrary, the 2D peak in BLG is a wide band, and less intensive than the G peak. By fitting the 2D peak with a Lorentzian function, we can prove that the 2D peak in the Raman spectrum of MLG only includes one component, but the 2D peak for BLG consists of four components. The position of the 2D peak upshifts with increasing number of layers,  $\sim 2668 \text{ cm}^{-1}$  for MLG,  $\sim 2685 \text{ cm}^{-1}$  for BLG,  $\sim 2722 \text{ cm}^{-1}$  for graphite.

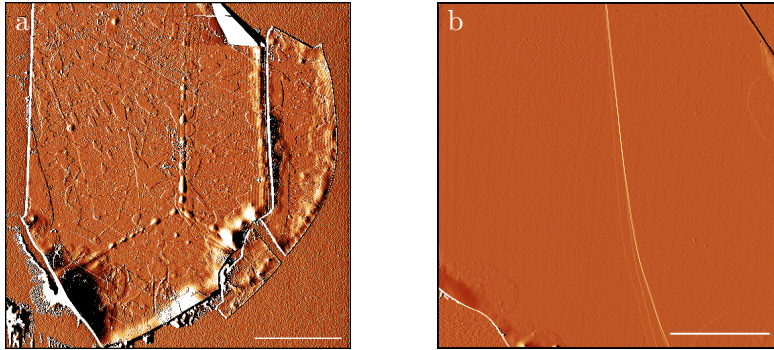


**Figure 2.3:** AFM images of a rough (a) and an atomically smooth (b) hBN surface. Scale bar is  $10 \mu\text{m}$ .

The hBN flakes are deposited on Si/SiO<sub>2</sub> substrates with the same technique as graphene. The flakes with  $10 \sim 40 \text{ nm}$  thickness are first selected in the optical microscope by their color appearance on the Si/SiO<sub>2</sub> substrate, as shown in Figure 2.1b. A precise characterization of hBN flakes is performed by using an AFM (BRUKER Dimension icon

system) operating in a tapping mode. It does not only measure the thickness of a hBN flake but also the surface morphology. In order to emphasize the surface morphology, Figure 2.3 shows the AFM images of two different hBN flakes in the amplitude error channel. It is obvious that the hBN flake in Figure 2.3b has an atomically smooth surface compared with the one in Figure 2.3a where the surface was destroyed during the mechanical cleavage process. Only the flakes with smooth and flat surfaces are used in the following fabrication steps.

### 2.1.2 Van der Waals assembly process

The hBN-graphene-hBN heterostructure can be assembled using the van der Waals adhesion of a graphene sheet to a hBN flake. Here we present our van der Waals assembly method which has been modified with respect to that proposed by Wang et al [14]. Figure 2.4 illustrates the procedure of the van der Waals material assembly. A transparent polymer, 7 wt% poly-propylene carbonate (PPC) (Sigma-Aldrich, CAS 25511-85-7) dissolved in ethyl acetate, is spun on the substrate with a thin hBN flake. The sample is then baked in a convectional oven at 80 °C for 10 min to evaporate the solvent. At the same time, a transparent PDMS (poly dimethyl siloxane) stamp is fixed on a clean microscope glass slide (Figure 2.4a). The substrate with the PPC film is inverted and then attached on the surface of the PDMS lying on the glass slide (Figure 2.4b). The substrate is removed manually from the stack, leaving the PPC film stucked on the PDMS stamp with the hBN flake faced up (Figure 2.4c). About 90% hBN flakes are transferred onto the surface of the PPC film. We mount the slide to our home-made transfer set-up shown in Figure 2.5, where it is possible to move the stack separately with respect to the target substrate. The hBN flake on the PPC film is aligned over a graphene flake on the target substrate by using a long working distance microscope and an x-y positioner (as shown in Figure 2.5). The hBN flake is then brought into contact with the graphene sheet (Figure 2.4d). We keep the sample at a temperature of 45 °C for 30 min to improve the van der Waals adhesion between hBN and graphene (Figure 2.4e). Once the temperature of the sample is cooled below 30 °C, the stack is lifted from the substrate (Figure 2.4f). Because graphene adheres more strongly to hBN than to SiO<sub>2</sub>, graphene is lifted together with hBN. The process is then repeated to place the hBN-graphene stack on top of a thick hBN flake (Figure 2.4g). Once the hBN-graphene-hBN heterostructure is completed, we heat the sample up to 60 °C in order to soften the PPC film. The glass slide together with the PDMS stamp is subsequently removed when keeping the PPC film melted (Figure 2.4h-i). The PPC is dissolved in acetone afterwards, leaving the hBN-graphene-hBN stack on the substrate.

This method provides an efficient way to build multi layer heterostructures just by repeating steps d-f.

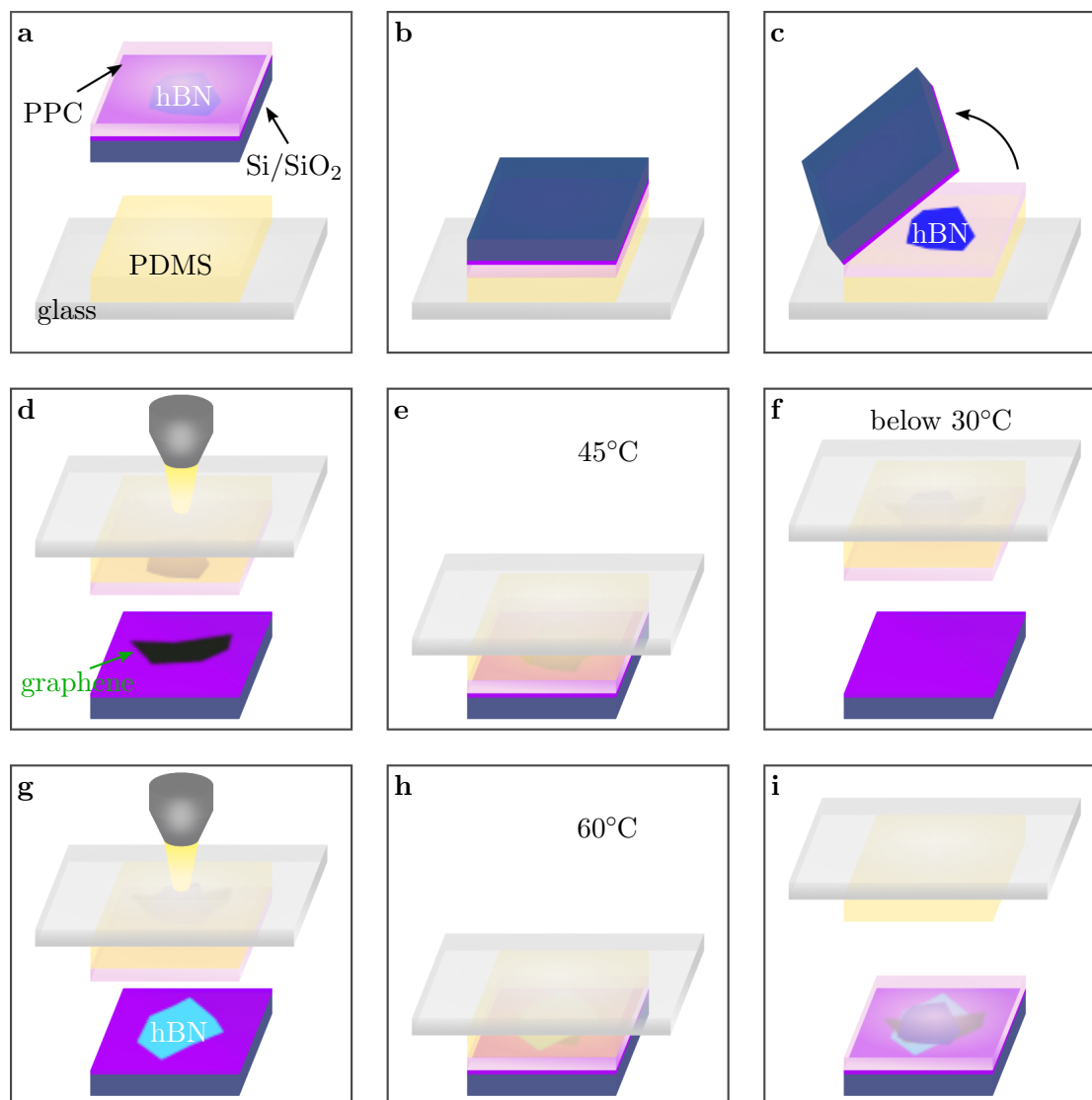


**Figure 2.4:** Van der Waals assembly process of a hBN-graphene-hBN heterostructure.

Although graphene is encapsulated between two hBN flakes, annealing at high temperatures is still necessary for the sake of cleaning the hydrocarbon adsorbates on the surface of graphene. The hydrocarbons are difficult to remove from an open graphene surface even by annealing in vacuum. However, in a hBN-graphene-hBN heterostructure, the hydrocarbon molecules can be removed from the interfaces during thermal annealing [28]. When the sample is heated, van der Waals bonds between hBN and graphene develop. As a consequence, the interfacial adsorbates are squeezed out or diffuse to form micrometer-sized bubbles visible as bright spots in Figure 2.6a, resulting in atomically sharp interfaces between hBN and graphene. In our case, the hBN-graphene-hBN sample is

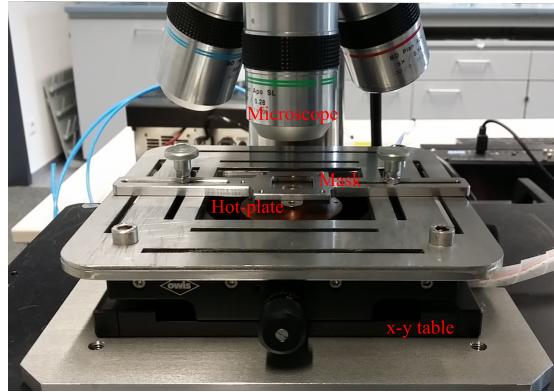


**Figure 2.5:** Transfer set-up. It consists of a long working distance microscope, a x-y table and a hot-plate. The target sample is mount on the hot-plate, which is right below object mirror of the microscope. The height of hot-plate can be tuned in micron scale. The glass stack is attached to the x-y table, which can move in the x-y directions with steps in a few micron. The transfer mask and the target sample are aligned via the microscope.

baked in air at 250 °C for 3 h to remove the hydrocarbons sandwiched at each interface as well as any PPC residues on the surface of top layer hBN.

After thermal annealing, AFM measurements are performed to check the flatness of the heterostructure and the exact location of graphene within the sandwich. As shown in Figure 2.6a, graphene (marked by the black dashed line) that is encapsulated between two hBN flakes is flat, but wrinkles and bubbles appear in the part without constraint from the top hBN layer (see Figure 2.6b). The area of the flat region depends on the size and smoothness of the hBN as well as the humidity of the atmosphere. In our work, we obtain flat areas of more than 10  $\mu\text{m}^2$ .

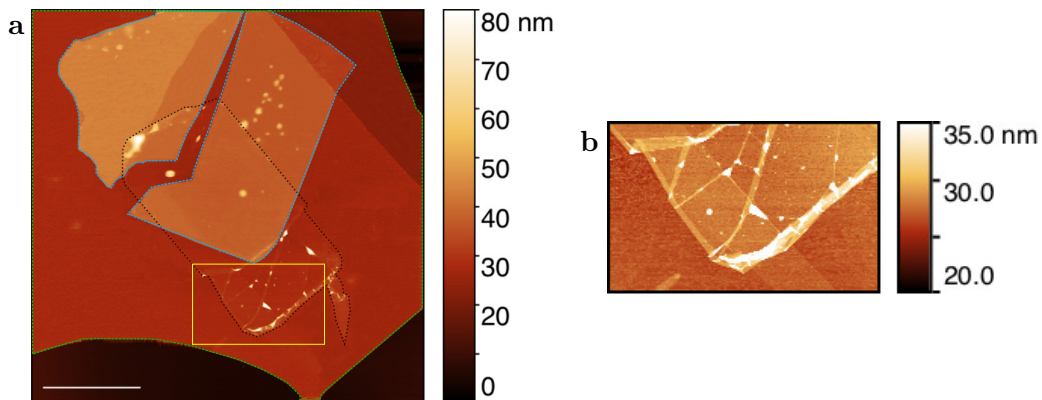


**Figure 2.6:** (a) A hBN-graphene-hBN heterostructure after thermal annealing. Scale bar is 10  $\mu\text{m}$ . The hBN flake on top of graphene is in orange, the bottom one is in red. The black dashed line shows the edges of graphene encapsulated between two hBN flakes. Graphene within the yellow rectangle is shown in (b). The edges and bubbles of graphene are more visible in (b).

### 2.1.3 Contacting the hBN-graphene-hBN heterostructure

The only way to connect encapsulated graphene is from the edges. Figure 2.7 illustrates the fabrication procedure for the edge contacts. At first, the edges of graphene devices are exposed by reactive ion etching (RIE). We use the e-beam lithography to define the etching mask with a two-layer resist, which consists of a 200 nm thick PMMA layer at the bottom and a 100 nm hydrogen silsesquioxane (HSQ) layer on the top, as depicted in Figure 2.7a. After the negative resist HSQ is developed in 25% TMAH for 4 min and rinsed with distilled water, the positive resist layer, PMMA, is etched in an oxygen plasma (Figure 2.7b). The etching rate for PMMA is about 45 nm/min setting the  $O_2$  flow rate of 15 sccm, the RF power of 30 W, the pressure of 60 mTorr in an Oxford ICP 80 system. Afterwards, the hBN-graphene-hBN stack is etched using plasma generated from a mixture of  $O_2$  and  $CHF_3$  gases with flow rate of 4 sccm and 40 sccm respectively (Figure 2.7c). The etch rate of the hBN is about 30 nm/min under 60 W RF power and

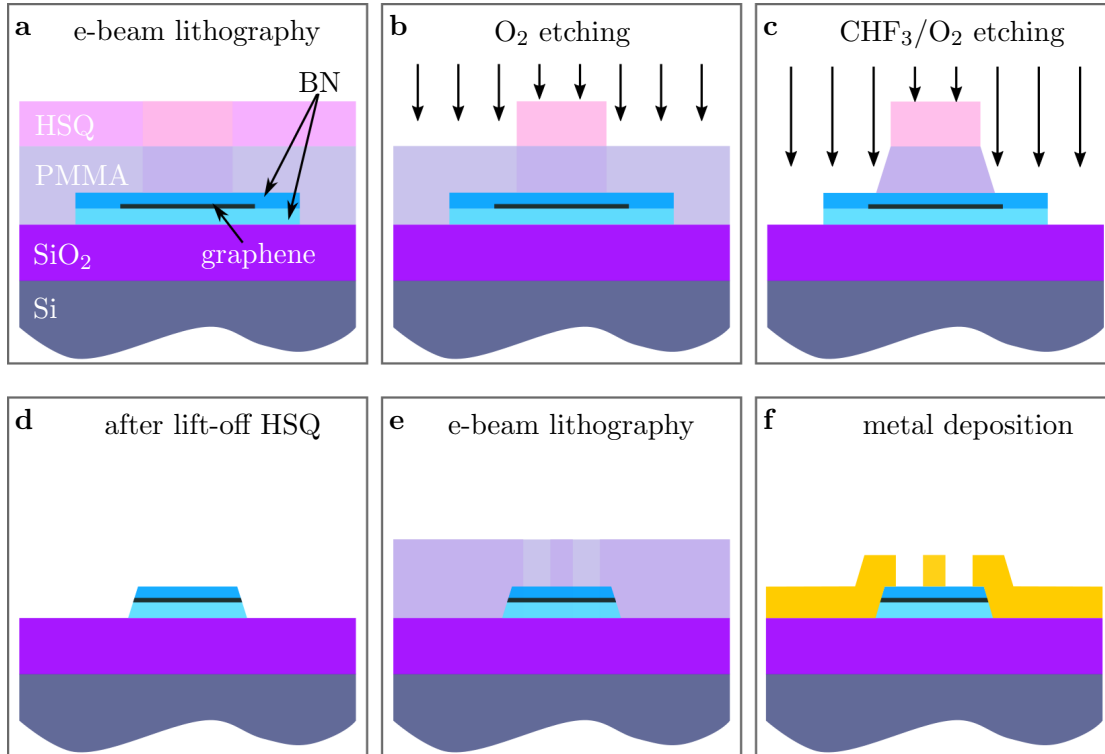


**Figure 2.7:** The process of one-dimensional edge-contact fabrication.

60 mTorr pressure. Since HSQ is a hard mask for reactive ion etching, the geometry of the device remains the same after etching. Then, the HSQ layer is lifted-off by dissolving the PMMA layer in acetone (see Figure 2.7d). Another e-beam lithography is performed to pattern the mask for edge contact leads and a local top gate (Figure 2.7e), and a thermal metal evaporation is conducted in the ultra high vacuum system (down to  $\sim 10^{-10}$  mbar) at a temperature below  $-120$  °C (Figure 2.7f). Finally, we fabricate

a lateral p-n-p junction with the Ti/Al (5 nm/85 nm) edge contacts and the Ti/Au (5 nm/75 nm) local top gate in the middle of the device. An AFM image of the final device (sample BL9) is shown in Figure 2.8(a).

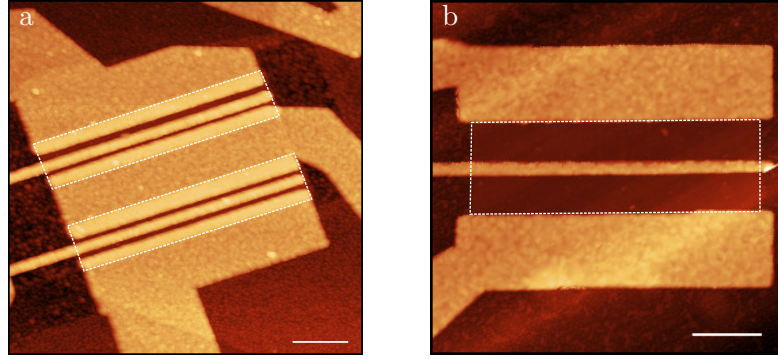


**Figure 2.8:** AFM images of two p-n-p junctions made of hBN-BLG-hBN heterostructures. The edge contacts fabrication method in Figure 2.7 is used for devices in (a) and the improved method in Figure 2.9 is used for the device in (b). The white dashed lines indicate the contour of bilayer graphene. The white dashed lines show the edges of graphene. Scale bar is 1  $\mu\text{m}$ .

The disadvantage of the above method is that the edge contacts have to be fabricated in two steps: (i) patterning the channel of the device; (ii) connecting the edges of graphene. Hence an overlap of the edge contact on top of the heterostructure is required in order to avoid misalignment in the second lithography step. We will see in the next chapter that the overlap part induces doping to graphene underneath it. On the other hand, it is difficult to reduce the length of the channel because of the limited space (see Figure 2.8a).

This method is improved by using just a layer of PMMA (without HSQ) as a mask both for etching and edge-contact deposition, as shown in Figure 2.9. We use a heterostructure including a graphite back-gate below the hBN-graphene-hBN stack and a local top gate deposited in advance. The PMMA mask for edge contacts is defined by utilizing an e-beam lithography at the beginning, as illustrated in Figure 2.9a. The exposed PMMA is developed in a solution of MIBK:ISO 1:3 for 15 s and rinsed with ISO for 10 s. Then, RIE is performed to etch the hBN-graphene-hBN stack with  $\text{CHF}_3/\text{O}_2$  gas, as sketched in Figure 2.9b. The etching duration is precisely controlled to make sure that the etch depth is sufficient to expose the graphene edges but keep the bottom hBN as thick as possible. Thereafter, a metal deposition is employed using the same PMMA mask for etching, as presented in Figure 2.9c. The edge contacts are formed after lift-off the metal in acetone, which is pictured in Figure 2.9d. Usually, an additional etching step is essential to define the geometry of the device and to remove the unwanted graphene around the edge contacts if necessary. Figure 2.8b displays the AFM image of a p-n-p junction fabricated with the refined method. In general, this amended method requires more efforts since the gates and edge contacts have to be deposited separately and a second RIE etching is normally desired to shape the device.

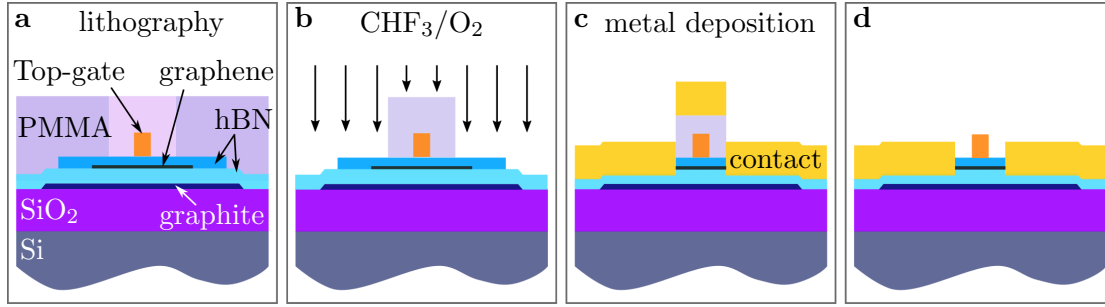


**Figure 2.9:** The improved method for making edge contacts.

## 2.2 Measurement techniques

The measurements are performed in a LD250 dilution refrigerator manufactured by BlueFors (Helsinki, Finland), which allows quantum transport measurements at a temperature down to 7 mK in high vacuum environment ( $\sim 10^{-6}$  mbar). The samples are mounted on a PCB (printed circuit board) sample holder using GE vanish and connected to the electric circuit by wire bonding. The sample holder is then fixed on the cold finger of the cryostat which is attached to the mixing chamber plate ( $\sim 7$  mK). The cold finger is inserted in a NbTi superconducting magnet, which can provide a magnetic field at the sample level up to 12 T. Figure 2.10 shows a diagram of the measurement circuit. The sample is measured in two-terminal methods but with false four-lead configuration in order to eliminate the resistance introduced from cables and RC filters. An AC voltage is supplied by a SR830 lock-in amplifier at a low frequency of 9.776 Hz, combined with a DC voltage provided by a BE2101 ultra low noise source (iTest Bilt System). A voltage divider is used to apply a small excitation on the sample. On the other hand, the output current is amplified by a DL1211 current preamplifier (DL instruments) and measured with another SR830 lock-in amplifier for the AC component and multimeter (Agilent 34410A) for the DC component. The voltage drop across the sample is measured by two additional lines. The AC and DC components are amplified by a low noise differential preamplifier (Celians EPC1-B) and a LI-75A low noise preamplifier (NF), respectively. Similarly, the AC and DC components of the voltage are recorded by a SR830 lock-in amplifier and a multimeter (Agilent 34410A) separately.

In order to avoid high-frequency noise introduced by the room-temperature instruments and the environment, a series of filters are added to each line at low temperatures. The high-frequency noise ( $f > 1$  GHz) is filtered by copper powder filters (CPF) on a PCB [29], which consists of 24 lines encapsulated in a mixture of copper particles and Stycast. Each line has a length of 3 m and a resistance of  $R = 43 \pm 1 \Omega$ . For lower-frequency noise ( $f > 1$  kHz), three-stage RC filters (RCF) are utilized. Twisted-pair

wires are used to cancel electromagnetic interference (EMI) from external sources and crosstalk between neighboring pairs.

The instruments are connected to GPIB cables, which are linked to a computer by an optical fiber. The computer is isolated electrically from the measurement system. All measurements are operated automatically with programs written in Python in the QTLab environment.

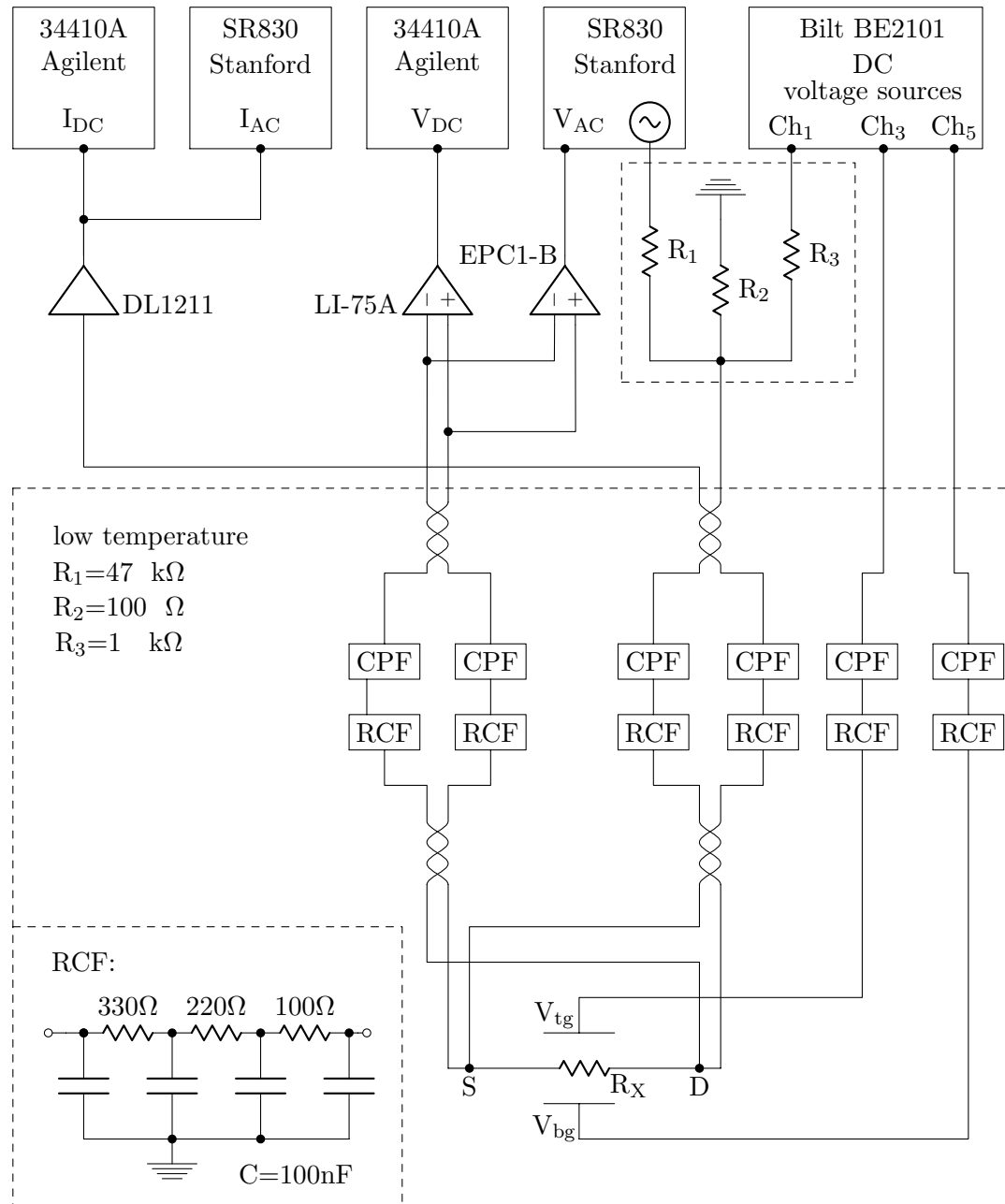


**Figure 2.10:** Diagram of measurement circuit. CPF and RCF are the abbreviations of copper powder filters and RC filters, respectively.



## Chapter 3

# Fabry-Pérot interference in bilayer graphene p-n-p heterojunctions

### 3.1 Introduction

In optics, the wave nature of photons is readily observed in the ubiquitous phenomenon of interference. A commonly used interferometer called the Fabry-Pérot consists of a glass with two semitransparent surfaces. The glass provides a cavity for photons bouncing back and forth within it. At each bouncing, waves are partially transmitted. The interference between the transmitted waves results in an intensity modulation, which is viewed as the sign of phase coherence. In solid state physics, the phase-coherent transport of electrons can be observed with an “electronic” Fabry-Pérot interferometer. In graphene, an electronic cavity can be created between p-n junctions using electrostatic fields.

The observation of Fabry-Pérot interferences requires ballistic transport. However, the mean free path of the charge carriers is usually small, less than 500 nm [30], for graphene on SiO<sub>2</sub> substrates due to the existence of disorder. Ballistic transport for long distances has been realized recently in the hBN-graphene-hBN heterostructures, where the mean free path exceeds 15  $\mu\text{m}$  [14]. In this chapter, we investigate the Fabry-Pérot interference for a bilayer graphene p-n-p junction. From the amplitudes of the interference fringes, we can analyze the quality of our devices.

The Fabry-Pérot interferometer is a useful tool to detect the phase shift of the electron waves. Young et al. have found a sudden phase shift of  $\pi$  in the interference pattern

at low magnetic fields, indicating the occurrence of the Klein tunneling in a single layer graphene p-n-p junction, where the top gate is about  $\sim 20$  nm wide. [8]. For bilayers, Varlet et al. have reported that, in the presence of the interlayer asymmetry, the non-trivial Berry phase shows a breaking of anti-Klein tunneling [12]. However, in their case, the quality of the device limited their study in the high-energy range, where the Fermi level is far from the band edge. In the present work, we benefit from high-quality devices, which enable the investigation of the Fabry-Pérot interference at both low energies and high energies. The phase shifts of the interference fringes are studied while tuning the Fermi level from the band edge to high energies.

### 3.1.1 Klein tunneling in single-layer graphene

The physics of a particle scattered from a finite potential step is a canonical problem in quantum mechanics, which has been studied for a long time. For a classical particle, it is forbidden to pass through a potential barrier with an energy higher than the energy of the particle. In the non-relativistic quantum mechanics regime, a quantum particle with energy  $E$  incident on a barrier of height  $V_0 > E$  and width  $L$ , has a finite probability to propagate through the potential barrier as an evanescent wave. The transmission probability decays exponentially with distance,  $T \sim \exp(-\beta L)$ , where  $\beta = \frac{\sqrt{2m(V_0-E)}}{\hbar}$ . In the case of a wide or high potential, the transmission probability decays rapidly. One year after the discovery of the Dirac equation [15], Oskar Klein has found that relativistic particles can tunnel through a potential barrier with a transmission probability that is independent of  $L$  [31]. For  $V_0 \gg E$ , the transmission probability is given by  $T = (E^2 - m^2c^4)/(E^2 - \frac{1}{2}m^2c^4)$ . In the case of  $E \gg mc^2$ ,  $T \approx 1$  so that the potential barrier becomes transparent. The difference between the non-relativistic and relativistic cases is that non-relativistic particles propagate through the barrier as evanescent waves, while relativistic particles tunnel through the barrier as their anti-particles because of the charge-conjugation symmetry.

However, the experimental demonstration of Klein tunneling is difficult since it is hard to achieve an atomically sharp potential. If the width  $d$  of the potential step over which the potential varies is comparable to or smaller than the Compton wavelength  $\lambda_C = h/(mc)$ , the tunneling is possible. Otherwise, the transmission probability will decay exponentially as demonstrated by Sauter [32]. In particle physics, the sharp interface can be attained in high-energy collisions, but the emergence of new particles becomes a dominant phenomenon. However, graphene provides a condensed-matter realization of Klein tunneling [8, 33], since the charge carriers in graphene are massless Dirac fermions.

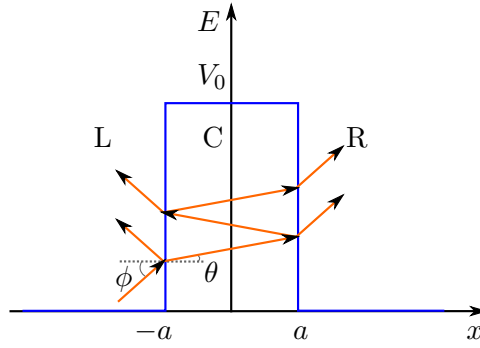


**Figure 3.1:** A sketch of a sharp potential barrier created by dual-gates in the npn regime. The height of the potential is  $V_0$  and the width is  $2a$ . The electron waves are incident from the left side of the potential. The transmitted waves are measured in the lead on the right side.

Klein tunneling in single-layer graphene and anti-Klein tunneling in bilayer graphene have been calculated by Katsnelson et al. [7]. In this section, we follow the same methods to give a simple introduction of Klein physics in graphene. More details and a full description of this theory is available in either the book of Katsnelson [34] or the review paper of Tudorovskiy et al. [35].

Figure 3.1 shows a sketch of an electron incident on a sharp potential barrier in a n-p-n junction. The potential consists of two sharp p-n interfaces separated by a distance of  $2a$ . We assume that the potential steps are extremely sharp, i.e., smaller than the Fermi wavelength, but larger than the lattice constant, so that Umklapp scattering between different valleys of graphene is prohibited. The spatial distribution of the potential profile along the  $x$  axis is given by

$$V(x) = \begin{cases} V_0, & |x| < a, \\ 0, & |x| > a. \end{cases} \quad (3.1)$$

The incident electrons reach the left side of the potential, where  $x < -a$ . In the local potential barrier ( $-a < x < a$ ), the holes act as positrons. The transmitted electron waves propagate on the right side of the potential ( $x > a$ ). In the low-energy limit, the Hamiltonian of the system reads [36].

$$H = -i\hbar v_F \boldsymbol{\sigma} \cdot \boldsymbol{\nabla} + V(x, y), \quad (3.2)$$

where  $V(x, y)$  is the potential energy. The wave vector outside the potential is denoted as  $k$ , and the one within the potential is written as  $q$ . At zero magnetic field, the  $y$ -component of the momentum is conserved. Thus, at the interface, we obtain the relation

between the incident angle  $\phi$  and the refraction angle  $\theta$  as

$$k \sin \phi = k_y = q_y = q \sin \theta. \quad (3.3)$$

The refractive angle is then defined as  $\theta = \arcsin(k_y/q)$ . The wave functions in the three regions are expressed as follows:

$$\Psi_L(x, y) = \begin{pmatrix} 1 \\ se^{i\phi} \end{pmatrix} e^{i(k_x x + k_y y)} + r \begin{pmatrix} 1 \\ -se^{-i\phi} \end{pmatrix} e^{i(-k_x x + k_y y)}, \quad x < -a, \quad (3.4)$$

$$\Psi_C(x, y) = a \begin{pmatrix} 1 \\ s'e^{i\theta} \end{pmatrix} e^{i(q_x x + k_y y)} + b \begin{pmatrix} 1 \\ -s'e^{-i\theta} \end{pmatrix} e^{i(-q_x x + k_y y)}, \quad |x| < a, \quad (3.5)$$

$$\Psi_R(x, y) = t \begin{pmatrix} 1 \\ se^{i\phi} \end{pmatrix} e^{i(k_x x + k_y y)}, \quad x > a. \quad (3.6)$$

Here,  $s = \text{sgn}(E)$  and  $s' = \text{sgn}(E - V_0)$ ,  $k = E/\hbar v_F$  and  $q = (E - V_0)/\hbar v_F$  are the wave vectors outside and inside the potential barrier, respectively. The  $x$ -components of the wave vectors are  $k_x = k \cos \phi$  and  $q_x = q \cos \theta$ .  $r$  represents the reflection amplitude on the left side of the potential barrier, while  $t$  is the transmission amplitude on the right side of the potential barrier.  $a$  and  $b$  are the amplitudes for the transmitted and reflected waves, respectively, inside the potential barrier. Since the wave function is continuous at the interfaces  $x = \pm a$ , we obtain the reflection amplitude from the boundary conditions

$$r = 2e^{i\phi - 2ik_x a} \sin(2q_x a) \frac{\sin \phi - ss' \sin \theta}{ss' [e^{-2iq_x a} \cos(\phi + \theta) + e^{2iq_x a} \cos(\phi - \theta)] - 2i \sin(2q_x a)}. \quad (3.7)$$

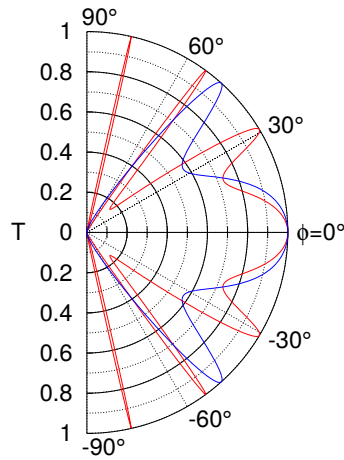


**Figure 3.2:** The angular transmission probabilities in single-layer graphene for a sharp potential barrier. The potential barrier with a length of 100 nm is considered. The Fermi energy of the incident electron is  $E = 100$  meV. Two potential barriers with different heights are considered. The red curve is related to  $V_0 = 215$  meV, while the blue curve corresponds to  $V_0 = 300$  meV.

The transmission probability  $T = |t|^2 = 1 - |r|^2$  is calculated from Equation (3.7). For normal incidence ( $\phi = 0$ ), the transmission probability is unity regardless of the height

of the potential barrier. The perfect tunneling is unique for massless Dirac fermions, for which the pseudospin flip is forbidden. Hence, a right moving electron can only be scattered by the potential barrier as a left moving hole state. This is the Klein tunneling in single-layer graphene. The angular dependent transmission probabilities are shown in Figure 3.2. The Fermi energy of the incident electron is chosen as  $E = 100$  meV. The right moving electrons face a potential field with a length of  $L = 2a = 100$  nm. The red and blue curves are calculated for potential heights of  $V_0 = 215$  meV and  $V_0 = 300$  meV, respectively. It is evident that Klein tunneling for  $\phi = 0$  is independent of the potential heights. In addition,  $T = 1$  is also reachable at certain angles which satisfy the condition  $q_x a = N \frac{\pi}{2}$ , where  $N$  is an integer.

The transmission probabilities in Figure 3.2 are based on sharp potentials. However, the potential steps are usually smooth in realistic experiments, regarding the finite thickness of the dielectric layer which determines the sharpness of the potential step. The transmission probability for a smooth potential is given by [37]

$$T = |t|^2 = e^{-\pi k_F d \sin^2 \phi}, \quad (3.8)$$

where  $d$  is the length on which the potential varies from 0 to  $V_0$ . Equation (3.8) is valid for  $\phi \ll \pi/2$ . The corresponding transmission probabilities are shown in Figure 3.3. The Klein tunneling occurs at normal incidence even though the potential step is smooth, whereas the transmission probabilities vanish exponentially at finite incident angles. This is known as ‘‘Klein collimation’’.

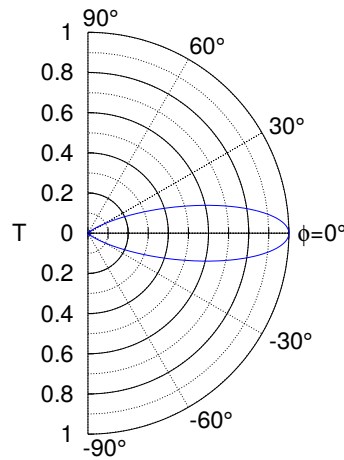


**Figure 3.3:** The angular transmission probabilities in single-layer graphene for a smooth potential barrier. The width of the potential step is  $d = 20$  nm. The incident energy of the electrons is 100 meV. The height of the smooth potential  $V_0$  is chosen as 300 meV.

### 3.1.2 Anti-Klein tunneling in bilayer graphene

In bilayer graphene, anti-Klein tunneling is expected instead of Klein tunneling when the electrons are scattered by a sharp potential barrier in the absence of a band gap. For A-B stacked bilayer graphene, the effective Hamiltonian at the low-energy excitations is written as [35]

$$H = -\frac{\hbar^2}{2m} \begin{pmatrix} 0 & (k_x - ik_y)^2 \\ (k_x + ik_y)^2 & 0 \end{pmatrix} + V(x), \quad (3.9)$$

where  $m = \gamma_1/2v^2 = 0.0355m_0$ ,  $m_0$  is the free electron mass.  $\gamma_0$  and  $\gamma_1$  are the in-plane and interplane hopping parameters. We consider that an electron faces a sharp potential barrier with an angle  $\phi$ . This is similar to the case described in Figure 3.1. The wave vectors outside and inside the potential barrier are defined as

$$k = \frac{\sqrt{2mE}}{\hbar}, \quad (3.10)$$

$$q = \frac{\sqrt{2m(V_0 - E)}}{\hbar}. \quad (3.11)$$

As the  $y$ -components of the wave vectors are constant, the wave function is expressed as  $\Psi(x, y) = \Psi(x)e^{ik_y y}$ . We thus obtain the one-dimensional solution  $\Psi(x)$  of the equation  $H\Psi(x, y) = E\Psi(x, y)$ , which is given by

$$\left(\frac{d^2}{dx^2} - k_y^2\right)^2 \Psi_i(x) = \left(\frac{2m(E-V(x))}{\hbar^2}\right)^2 \Psi_i(x), \quad i = 1, 2. \quad (3.12)$$

In the limit of  $V_0 > E + \frac{\hbar^2 k_y^2}{2m}$ , the solutions of Equation (3.12) in the three different regions are found [35]:

$$\Psi_L(x) = \begin{pmatrix} 1 \\ se^{2i\phi} \end{pmatrix} e^{ik_x x} + b_1 \begin{pmatrix} 1 \\ se^{-2i\phi} \end{pmatrix} e^{-ik_x x} + c_1 \begin{pmatrix} 1 \\ -sh_1 \end{pmatrix} e^{\kappa_x x}, \quad (3.13)$$

$$\Psi_C(x) = a_2 \begin{pmatrix} 1 \\ s'e^{2i\theta} \end{pmatrix} e^{iq_x x} + b_2 \begin{pmatrix} 1 \\ s'e^{-2i\theta} \end{pmatrix} e^{-iq_x x} + c_2 \begin{pmatrix} 1 \\ -s'h_2 \end{pmatrix} e^{\lambda_x x} + d_2 \begin{pmatrix} 1 \\ -s'/h_2 \end{pmatrix} e^{-\lambda_x x}, \quad (3.14)$$

$$\Psi_R(x) = a_3 \begin{pmatrix} 1 \\ se^{2i\phi} \end{pmatrix} e^{ik_x x} + d_3 \begin{pmatrix} 1 \\ -s/h_1 \end{pmatrix} e^{-\kappa_x x}. \quad (3.15)$$

Here,  $k_x = k \cos \phi$ ,  $k_y = k \sin \phi$ ,  $q_x = q \cos \theta$ ,  $q_y = q \sin \theta = k_y$ ,  $\kappa_x = k\sqrt{1 + \sin^2 \phi}$ ,  $\lambda_x = q\sqrt{1 + \sin^2 \theta}$ ,  $s = \text{sgn}(E)$ ,  $s' = \text{sgn}(E - V_0)$ ,  $h_1 = (\sqrt{1 + \sin^2 \phi} - \sin \phi)^2$ ,  $h_2 = (\sqrt{1 + \sin^2 \theta} - \sin \theta)^2$ .

The amplitudes  $a_i$ ,  $b_i$ ,  $c_i$  and  $d_i$  are calculated by the continuity of the wave function  $\Psi_i$  and its derivative  $d\Psi_i/dx$  at the interfaces  $x = \pm a$ . By numerically solving the

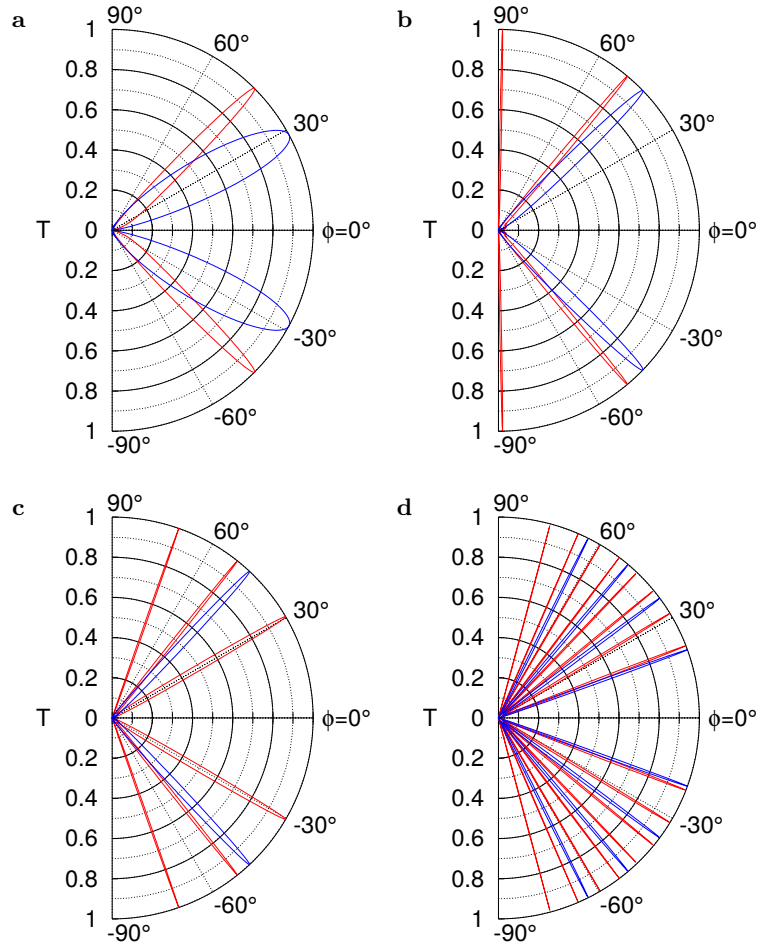


**Figure 3.4:** The transmission probabilities as a function of the electron incident angle in bilayer graphene for a potential barrier with a length of 50 nm (a), 100 nm (b), 150 nm (c), and 400 nm (d). The Fermi energy of incident electron is  $E = 20$  meV. Two potential barriers with different heights are considered. The red curve is related to  $V_0 = 50$  meV, while the blue curve corresponds to  $V_0 = 100$  meV.

boundary conditions, we obtain the transmission probabilities for various incident angles (see Appendix A). Figure 3.4 shows the transmission probabilities as a function of the incident angles. The angular transmission depends on the length of the potential barrier. Four examples are presented in Figure 3.4a, Figure 3.4b, Figure 3.4c and Figure 3.4d for potential barrier lengths of  $L = 50, 100, 150, 400$  nm, respectively. The transmission probabilities of electrons with an energy of 20 meV tunneling through a barrier with a height of  $V_0 = 50$  or 100 meV are shown in red or blue in each plot. At certain incident angles, the potential barrier becomes transparent, which is similar to the situation of single-layer graphene. At the normal incidence, the transmission probability is expressed analytically, that is

$$T = |a_3|^2 = \left| \frac{4ikqe^{2ika}}{(q+ik)^2 e^{-2qa} - (q-ik)^2 e^{2qa}} \right|^2. \quad (3.16)$$

If  $a$  goes to infinity, the transmission probability approaches zero, which is the contrary in the case of single-layer graphene. This is the anti-Klein tunneling in bilayer graphene.

### 3.1.3 Berry phase in single-layer and bilayer graphene

The Berry phase of electron wave function affects the electronic transport properties in many aspects, such as electric polarization [38], quantum Hall effect [39], orbital magnetism [40], and quantum charge pumping [41]. Berry has demonstrated that a quantum system acquires a geometrical phase factor  $e^{i\gamma_n}$  when the eigenstate undergoes a cyclic adiabatic evolution [42, 43]. In this process, the external parameter  $\mathbf{R}$  changes slowly in the Hamiltonian  $H(\mathbf{R})$ . The Berry phase is a gauge invariant quantity, which is expressed as a closed path integral in the parameter space, which reads

$$\gamma_n = \oint_C d\mathbf{R} \cdot A_n(\mathbf{R}) \quad (3.17)$$

Here  $A_n(\mathbf{R})$  is the Berry connection or Berry vector potential, which is given by

$$A_n(\mathbf{R}) = i\langle n(\mathbf{R}) | \nabla_{\mathbf{R}} | n(\mathbf{R}) \rangle, \quad (3.18)$$

where  $|n(\mathbf{R})\rangle$  is the basis function for the Hamiltonian  $H(\mathbf{R})$  in the parameter space. From Equation (3.17) and Equation (3.18), it is noted that the Berry phase only depends on the geometrical aspect of the closed path integral. In analogy to electrodynamics, we define the Berry curvature as [43]

$$\boldsymbol{\Omega}_n(\mathbf{R}) = \nabla_{\mathbf{R}} \times A_n(\mathbf{R}). \quad (3.19)$$

According to Stokes's theorem, the Berry phase is expressed as a surface integral

$$\gamma_n = \int_S d\mathbf{S} \cdot \boldsymbol{\Omega}_n(\mathbf{R}). \quad (3.20)$$

Here, the Berry curvature  $\boldsymbol{\Omega}_n(\mathbf{R})$  is analogous to the magnetic field.

#### 3.1.3.1 Berry phase in single-layer graphene and gapless bilayer graphene

In graphene, the direction of motion is coupled to the orientation of the pseudospin. The chiral nature of charge carriers has profound effects on transports, for example, the Berry phase. In the low-energy limit, the Hamiltonians for single-layer and bilayer

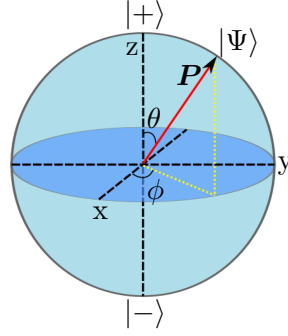


**Figure 3.5:** Sketch of a polarization vector  $\mathbf{P}$  on a Bloch sphere. A quantum state  $|\Psi\rangle$  is described by  $\mathbf{P}$ .

graphene are written as [9]

$$\begin{aligned} H_{SLG} &= v_F \begin{pmatrix} 0 & \pi^+ \\ \pi & 0 \end{pmatrix}, \\ H_{BLG} &= -\frac{1}{2m} \begin{pmatrix} 0 & (\pi^+)^2 \\ \pi^2 & 0 \end{pmatrix}, \end{aligned} \quad (3.21)$$

respectively.  $\pi = p_x + ip_y$  is the momentum operator. In the case of bilayer graphene,  $H_{BLG}$  is the effective low-energy Hamiltonian that describes the effective hopping between the non-dimer sites, A1-B2. The two-component spinors are  $(\Psi_A, \Psi_B)^T$  for single-layer graphene and  $(\Psi_{A1}, \Psi_{B2})^T$  for bilayer graphene. The eigenstates are described as follows:

$$\begin{aligned} |\Psi_{SLG}^\pm\rangle &= \frac{1}{\sqrt{2}} \begin{pmatrix} \pm e^{-i\phi} \\ 1 \end{pmatrix}, \\ |\Psi_{BLG}^\pm\rangle &= \frac{1}{\sqrt{2}} \begin{pmatrix} \pm e^{-2i\phi} \\ 1 \end{pmatrix}. \end{aligned} \quad (3.22)$$

In general, to understand the adiabatic evolution of the eigenstates, we first define a polarization vector  $\mathbf{P}$  for a spin- $\frac{1}{2}$  quantum state  $|\Psi\rangle = (e^{-i\phi} \cos \frac{\theta}{2}, \sin \frac{\theta}{2})^T$ , as sketched in Figure 3.5, that is [44]

$$\mathbf{P} = \begin{pmatrix} \langle \Psi | \sigma_x | \Psi \rangle \\ \langle \Psi | \sigma_y | \Psi \rangle \\ \langle \Psi | \sigma_z | \Psi \rangle \end{pmatrix} = \begin{pmatrix} \sin \theta \cos \phi \\ \sin \theta \sin \phi \\ \cos \theta \end{pmatrix}, \quad (3.23)$$

with  $\theta \in [0, \pi]$  being the polar angle and  $\phi \in [0, 2\pi]$  being the azimuthal angle. The vector  $\mathbf{P}$  with the length of 1 generates a Bloch sphere. A quantum state  $|\Psi\rangle$  is represented by a superposition of the two basis states  $|+\rangle = (1, 0)^T$  and  $|-\rangle = (0, 1)^T$  as  $|\Psi\rangle = e^{-i\phi} \cos \frac{\theta}{2} |+\rangle + \sin \frac{\theta}{2} |-\rangle$ . Then, the pseudospin orientation of  $|\Psi\rangle$  is pointing in the

direction of  $\mathbf{P}$  on the Bloch sphere. We obtain the polarization vector  $\mathbf{P}$  for single-layer and bilayer graphene by substituting the eigenstates of Equation (3.22) into Equation (3.23), resulting in [9, 44, 45]

$$\mathbf{P}_{SLG} = \begin{pmatrix} \cos \phi \\ \sin \phi \\ 0 \end{pmatrix}, \quad \mathbf{P}_{BLG} = \begin{pmatrix} \cos 2\phi \\ \sin 2\phi \\ 0 \end{pmatrix}. \quad (3.24)$$

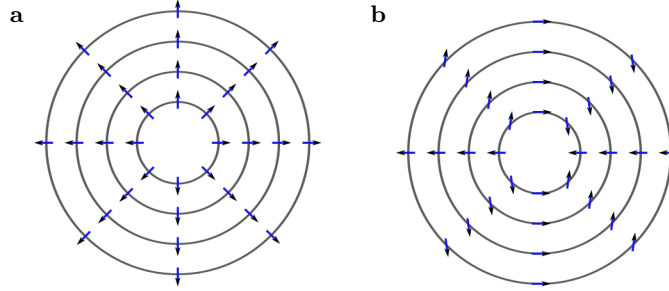


**Figure 3.6:** Pseudospin projections of electrons along the constant energy contours in single-layer (a) and bilayer graphene (b). The center of each plot is the  $K$  point. The pseudospin projections are independent of energy.

There are no  $z$ -components in  $\mathbf{P}$  for both single-layer and bilayer graphene, which illustrates that  $\mathbf{P}$  varies in the equatorial plane of the Bloch sphere. As a consequence, the pseudospin rotates in the same plane, where  $\theta = \pi/2$ . In graphene, when the electronic wave vector experiences one full rotation around the Dirac point, the number of rotations that the pseudospin rotates is defined as winding number. From Equation (3.24), we notice that the winding number is 1 for single-layer graphene but 2 for bilayer graphene. Therefore, in the case of single-layer graphene, the pseudospin rotates with the same speed of the wave vector so that it is normal to the constant energy contours, as shown in Figure 3.6a. In gapless bilayer graphene, the pseudospin winds twice for a  $2\pi$  rotation of the wave vector, as shown in Figure 3.6b. The processes are independent of energies in both cases.

We utilize Equation (3.17) and Equation (3.18), and calculate the Berry phase for single-layer and bilayer graphene in the spherical coordinate system. For the eigenstate  $|\Psi_{SLG}^+\rangle$ , the Berry connection is  $A(\phi) = \langle \Psi_{SLG}^+ | i \frac{\partial}{\partial \phi} | \Psi_{SLG}^+ \rangle = 1/2$ , and the associated Berry phase  $\gamma = \int_0^{2\pi} A(\phi) d\phi = \pi$ . Similarly, in the case of bilayer graphene, we have  $A(\phi) = 1$  and  $\gamma = 2\pi$ .

### 3.1.3.2 Berry Phase in gapped bilayer graphene

In bilayer graphene, the inversion symmetry of the lattice can be broken by applying external gate voltages, which gives rise to non-trivial diagonal components in  $H_{BLG}$ , that is

$$H_{BLG} = \begin{pmatrix} -\frac{u}{2} & -\frac{(\pi^+)^2}{2m} \\ -\frac{\pi^2}{2m} & \frac{u}{2} \end{pmatrix}. \quad (3.25)$$

The presence of the diagonal terms results in the  $z$ -component of the polarization vector, which induces an energy-dependent pseudospin rotation out of the equatorial plane, as described in Figure 3.7. Near the band edge, the pseudospin is highly polarized along  $z$ -axis, as shown in Figure 3.7a. Hence, the chirality is broken. The Berry phase is zero since the pseudospin does not round a circuit. At high energies, the in-plane motion of the pseudospins is asymptotically recovered, so that the chirality is restored. When the pseudospin returns to the equatorial plane, the Berry phase is  $2\pi$  again. Thus, the Berry phase takes values from 0 to  $2\pi$  in the presence of a interlayer asymmetry.

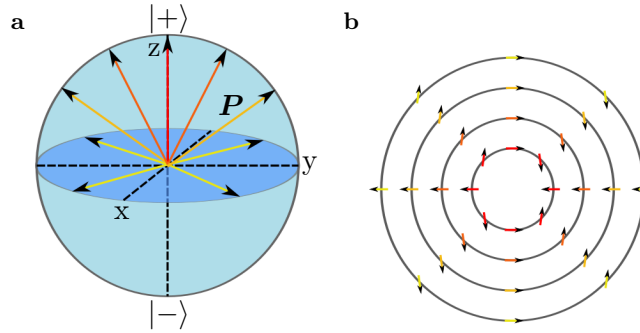


**Figure 3.7:** Pseudospin in gapped bilayer graphene. (a) Sketch of the polarization vectors in gapped bilayer graphene.  $\mathbf{P}$  represents the pseudospin polarization. The  $z$ -component of pseudospin is recovered in the presence of a interlayer asymmetry. Close to the band edges, the pseudospin is completely polarized. (b) The pseudospin projections along the constant energy contours. The color of the arrows corresponds to the pseudospin polarization in (a). The pseudospin is energy-dependent in gapped bilayer graphene.

## 3.2 Sample description

The samples are fabricated using the procedures described in Chapter 2. Figure 3.8 shows the schematic and AFM image of bilayer graphene p-n-p junctions. In Figure 3.8a, the layout of a device is presented. The Si substrate is used as a global back-gate. The  $\text{SiO}_2$  layer is  $317 \pm 1$  nm thick, measured with the FILMETRICS spectrometer. Bilayer graphene is encapsulated with two atomically flat hBN flakes. The top one has a thickness of 14 nm and the bottom one is 35.5 nm. The thin top dielectric

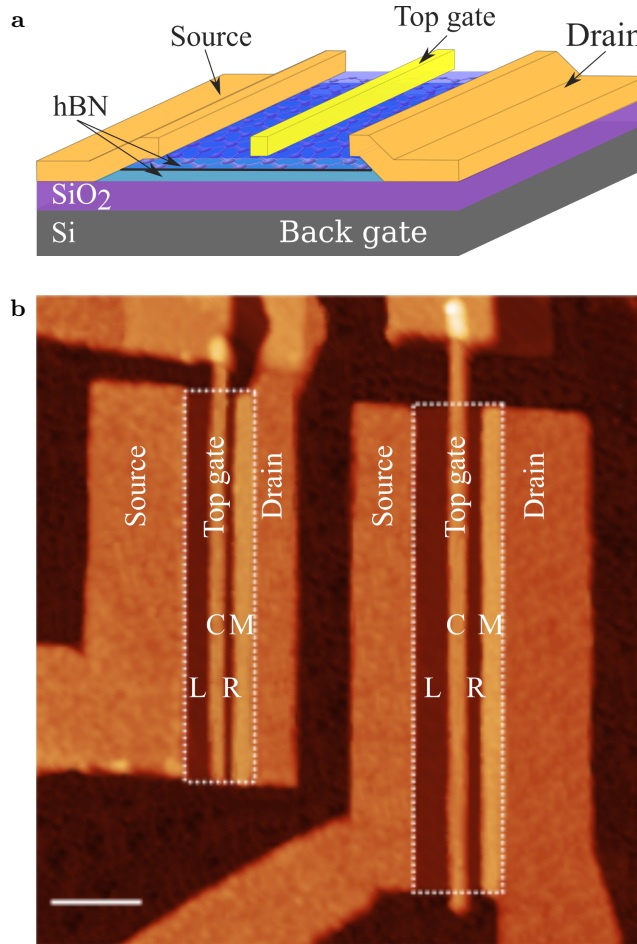


**Figure 3.8:** Sample description of bilayer graphene p-n-p junctions. (a) Schematic of a bilayer graphene p-n-p junction. Bilayer graphene is encapsulated between two hBN flakes and connected with Ti/Al contacts from the edges. (b) The AFM image of the two devices measured in this thesis. The white dashed lines show the edges of bilayer graphene. Scale bar is  $1 \mu\text{m}$ . The sample BL12C (right one) is  $1 \mu\text{m} \times 5 \mu\text{m}$  and the sample BL12D (left one) is  $0.8 \mu\text{m} \times 4 \mu\text{m}$ . The channel of each device is divided into four regions, i.e. L, C, R, M. Bilayer graphene under the top gate is denoted as C, the areas on the left and right side of the top-gated region are marked as L and R, and the area below the metal contact is labeled as M.

enables us to create a relatively sharp potential barrier by placing a local top gate. Two devices are connected with Ti/Al ( $5 \text{ nm}/84 \text{ nm}$ ) leads from the same hBN-BLG-hBN heterostructure. Figure 3.8b shows the AFM image of the two devices. The white dashed lines mark the edges of bilayer graphene. The right one (sample BL12C) has a channel length of  $1 \mu\text{m}$  and width of  $5 \mu\text{m}$ . The one at the left (sample BL12D) possesses the same  $W/L$  ratio of 5 as the sample BL12C, but with a shorter channel length of  $0.8 \mu\text{m}$ . In the middle of the two devices, the top gates are deposited with Ti/Au ( $5 \text{ nm}/73 \text{ nm}$ ). Both gates have a width of  $\sim 150 \text{ nm}$ . According to the configuration of the device, the channel can be divided into four regions, bilayer graphene under the top gate (denoted

as C), the areas on the left and right side of the top-gated region (marked as L and R, respectively), and the area below the metal contact (denoted as M).

### 3.3 Electrical transport in bilayer graphene p-n junctions

The devices are characterized at 4.2 K with the methods described in Section 2.2. Figure 3.9a presents the colormap of the conductance of the sample BL12C measured as a function of both  $V_{bg}$  and  $V_{tg}$  at zero magnetic field. The two horizontal blurred lines at  $V_{bg} = -7.51$  V and  $V_{bg} = -25.9$  V, indicate the conductance minima. These positions of the conductance minima are independent of the top-gate voltages, and only determined by the back-gate voltages. They correspond to the charge neutrality points of bilayer graphene that are only tuned by the back-gate, for example, bilayer graphene in areas L, R, and M (see Figure 3.8). Along the white arrow, we observe the third line of the conductance minimum, which is tuned using both the top-gate and back-gate voltages simultaneously. Thus, it indicates the charge neutrality point of bilayer graphene under the top gate, i.e. area C. The low conductance line determines the displacement field  $D$  axis, denoted as the white arrow. When increasing the  $D$  field, the conductance along the  $D$  axis decreases. Although an insulating state has not been reached, the increasing width and distance of the diagonal line indicates the opening of a band gap.

The map can be divided into six regions by the three charge neutrality lines. Each region has a unique charge polarity combination. The combinations are labeled on the conductance map as nnnn, npnn, pnnp, pnpp, pppn and pppp, corresponding to the charge types in the sequential regions L, C, R, M. In the unipolar regime, the charges in the top-gated region C have the same polarity as their counterparts in the neighboring regions L and R, i.e. nnnn, pppn, pppp, in contrast to the bipolar regime, such as npnn, pnnp, pnpp.

Figure 3.9b shows the resistance along the yellow dashed line in Figure 3.9a, where  $V_{tg} = 0$  V. Three resistive peaks appear at the voltages of  $V_{bg} = 6.69$  V,  $-7.51$  V,  $-25.9$  V, indicating the charge neutrality points in different regions. From the shift of the charge neutrality points, we note that the intrinsic doping in each region is different. Bilayer graphene in the areas L and R is equally doped. The peak at  $V_{bg} = -7.51$  V indicates that bilayer graphene is n-doped in the areas L and R. The n-doping may come from the residue of hydrocarbons which enter the sample during the fabrication process done in ambient conditions. Although we have annealed the sample to get rid of the hydrocarbons, a small amount of hydrocarbons may remain in the sample [28]. In the area M, the contact is overlapping on top of bilayer graphene with a spacer, i.e. the top hBN layer. The presence of the overlapped contact induces an additional n-doping

in bilayer graphene, which gives rise to the peak at the  $V_{bg} = -25.9$  V. The peak at  $V_{bg} = 6.69$  V is linked to the area C, in which bilayer graphene is p-doped. If we tune the back-gate voltage, the Fermi level in the four regions is changed simultaneously. In Figure 3.9d, the band diagrams are shown for each region. The yellow and blue filled areas indicate the occupied states in the conduction and valence bands, respectively. The red solid line shows the intrinsic potential profile along the channel. The dotted line shows the Fermi level. As the back-gate voltage decreases, the Fermi level reduces and passes through the charge neutrality point in the regions C, L and R, M in sequence, as sketched in the top, middle, bottom panels in Figure 3.9d.

In Figure 3.9c, the resistance is presented as a function of the  $V_{tg}$  with  $V_{bg} = 0$  V, which corresponds to the green dashed line in Figure 3.9a. The charge neutrality point is observed at  $V_{tg} = 0.41$  V. The resistances are asymmetrical between the electron and hole sides. The reason is that a n-p-n junction is formed on the hole side since bilayer graphene outside the top-gated region is intrinsically n-doped.

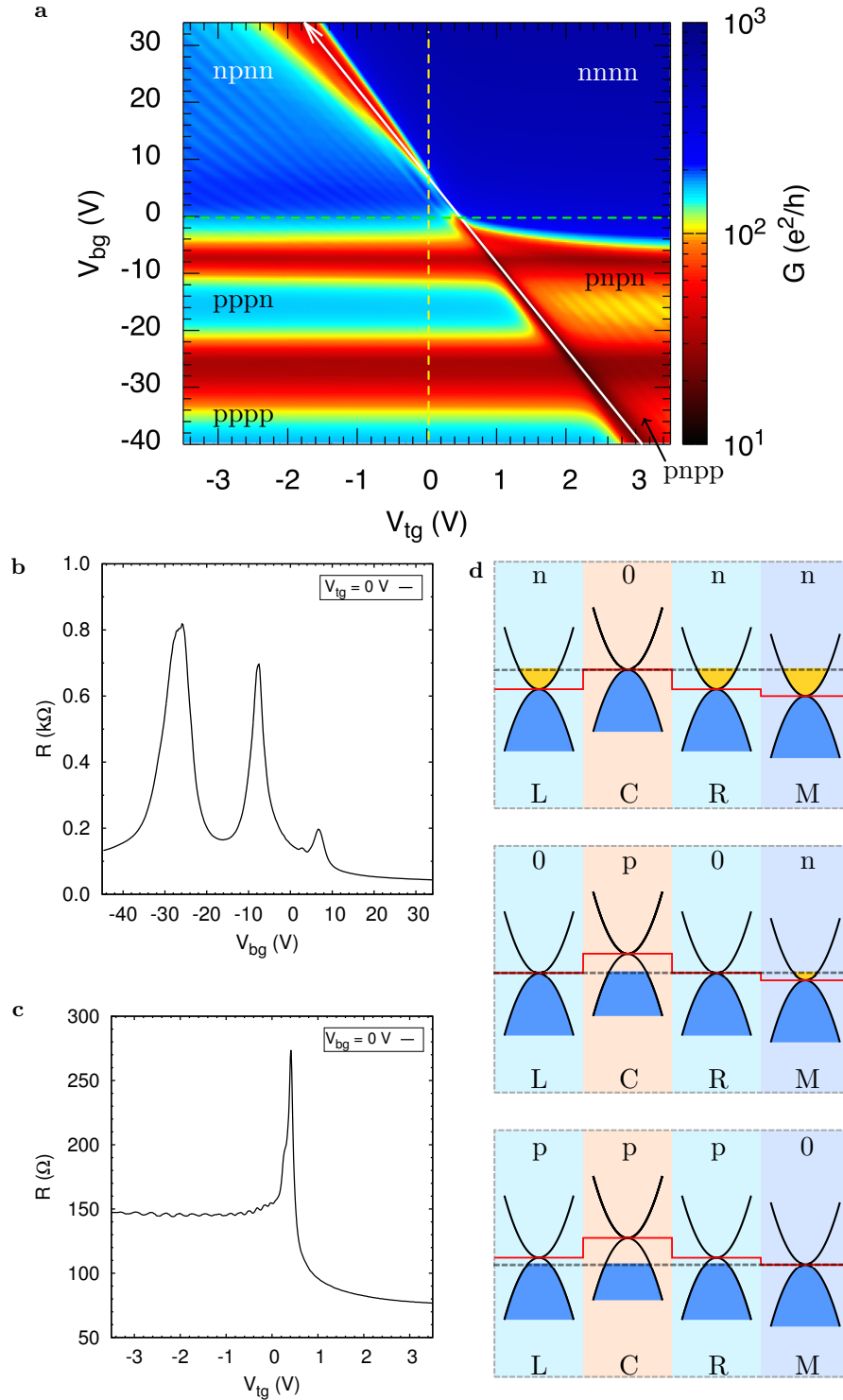


**Figure 3.9:** Characteristic of a bilayer graphene p-n-p junction (sample BL12C). (a) Conductance as a function of the top-gate voltage  $V_{tg}$  and back-gate voltage  $V_{bg}$ . The white arrow indicates the displacement field  $D$  axis. (b) The resistance versus  $V_{bg}$  along the yellow dashed line in (a), where  $V_{tg} = 0$  V. (c) The resistance varies with respect to the  $V_{tg}$  at zero back-gate voltage, which is along the green dashed line in (a). The measurements have been done at 4.2 K and zero magnetic field. (d) The low energy spectrum for quasiparticles in four different regions (L, C, R, M). The dotted line shows the Fermi level. The yellow and blue filled areas indicate the occupied states in the conduction and valence bands, respectively. The red solid line shows the profile of the potential barrier. The top, middle, and bottom panels depict the positions of the Fermi energy, corresponding to the charge neutrality points in the region C, L & R, and M, respectively.

### 3.3.1 Electrostatic model

We utilize the parallel-plate capacitor model to calculate the electrostatic field for dual-gated bilayer graphene devices. The device is viewed as three plate capacitors in series, i.e. the one between the top gate and the top layer of bilayer graphene, the one between the top and bottom layers of bilayer graphene, and the one between the bottom layer of bilayer graphene and the bottom-gate. Thus, the top-gate and back-gate capacitances are given by  $C_{tg} = \frac{\epsilon_0 \epsilon_r^{hBN}}{d_{hBN}^{(top)}}$ ,  $C_{bg} = \left( \frac{d_{hBN}^{(bot)}}{\epsilon_0 \epsilon_r^{hBN}} + \frac{d_{SiO_2}}{\epsilon_0 \epsilon_r^{SiO_2}} \right)^{-1}$ , respectively, where  $\epsilon_0$  is the vacuum permittivity,  $\epsilon_r^{hBN}$  and  $\epsilon_r^{SiO_2} = 3.9$  is the dielectric constants of the hBN and SiO<sub>2</sub>, respectively.  $d_{hBN}^{(top)} = 14$  nm and  $d_{hBN}^{(bot)} = 35.5$  nm are the thickness of the top hBN and the bottom hBN, respectively.  $d_{SiO_2} = 317$  nm is the thickness of the SiO<sub>2</sub> layer.

By operating the dual-gates, the displacement field in the area C is tuned. We define the displacement field as

$$\tilde{D} = \frac{D}{\epsilon_0} = -\frac{C_{tg}}{\epsilon_0} (V_{tg} - V_{tg}^{(0)}) + \frac{C_{bg}}{\epsilon_0} (V_{bg} - V_{bg}^{(0)}), \quad (3.26)$$

where  $V_{tg}^{(0)}$  and  $V_{bg}^{(0)}$  are the top-gate and back-gate voltages applied to overcome the intrinsic doping in the dual-gated region (area C), respectively. They are chosen as  $V_{bg}^{(0)} = -7.51$  V and  $V_{tg}^{(0)} = 0.94$  V. The charge carrier density in the region C is given by

$$n_C = \frac{C_{tg}}{e} (V_{tg} - V_{tg}^{(0)}) + \frac{C_{bg}}{e} (V_{bg} - V_{bg}^{(0)}), \quad (3.27)$$

where  $e$  is the charge of an electron. In the case of  $n_C = 0$ , Equation (3.27) expresses the function of  $D$  axis. The ratio of the top-gate capacitance to the back-gate capacitance  $C_{tg}/C_{bg} = 15.3$  is obtained from the slope of the  $D$  axis in Figure 3.9a. Therefore, we obtain  $\epsilon_r^{hBN} = 2.2$  for our devices. Then,  $C_{tg} = 139.13$  nF/cm<sup>2</sup> and  $C_{bg} = 9.09$  nF/cm<sup>2</sup> are calculated. Finally, the charge carrier density in each region can be expressed as

$$n_X(V_{tg}, V_{bg}) = \begin{cases} \frac{C_{tg}}{e} V_{tg} + \frac{C_{bg}}{e} V_{bg} + n_X^0 & X = C \\ \frac{C_{bg}}{e} V_{bg} + n_X^0 & X = L, R, M \end{cases}, \quad (3.28)$$

where  $n_X^0$  denotes the intrinsic doping in each region.  $n_X^0$  is calculated from the position of the charge neutrality points in Figure 3.9b and Figure 3.9c. We obtain  $n_L^0 = n_R^0 = 4.26 \times 10^{11}$  cm<sup>-2</sup> and  $n_M^0 = 14.69 \times 10^{11}$  cm<sup>-2</sup> from the position of the charge neutrality points in Figure 3.9b. And  $n_C^0 = -3.56 \times 10^{11}$  cm<sup>-2</sup> is obtained from the position of the charge neutrality point in Figure 3.9c.

### 3.3.2 Interlayer asymmetry in bilayer graphene

The application of a voltage to the top- and back-gates introduces an asymmetry between the two layers of bilayer graphene. The asymmetry parameter  $u$  expresses the difference in the on-site energies of the orbitals on the two layers, which is defined as [9]

$$\frac{u}{\gamma_1} = \frac{\Lambda(n_b - n_t)}{n_\perp} \left[ 1 - \frac{\Lambda}{2} \ln \left( \frac{|n|}{2n_\perp} + \frac{1}{2} \sqrt{\left(\frac{n}{n_\perp}\right)^2 + \left(\frac{u}{2\gamma_1}\right)^2} \right) \right]^{-1}. \quad (3.29)$$

$n_t$  and  $n_b$  are the charge carrier densities generated by the top-gate and back-gate voltages, respectively.  $n$  is the total charge carrier density, i.e.  $n = n_t + n_b$ . The characteristic carrier density is  $n_\perp = \frac{\gamma_1^2}{\pi \hbar^2 v_F^2}$ , and the screening parameter is  $\Lambda = \frac{c_0 e^2 n_\perp}{2\gamma_1 \epsilon_r \epsilon_0}$ .  $\gamma_1$  stands for the nearest-neighbor hopping between the two layers, i.e., the interlayer coupling.  $c_0$  is the interlayer spacing.  $\epsilon_r$  is the effective dielectric constant between the two layers of bilayer graphene. The parameter  $u$  can be obtained by numerically solving Equation (3.29). The corresponding size of the band gap is given by

$$u_g = \frac{|u| \gamma_1}{\sqrt{\gamma_1^2 + u^2}}. \quad (3.30)$$

However, in our experiments, the applied displacement field does not fully open a gap between the conduction and valence bands. As shown in Figure 3.10, the resistance is tuned by the top gate for a number of constant back-gate voltages. The resistance along the displacement field axis, where  $n_C = 0$ , is shown by the black curve. Since an additional Dirac peak, originating from the contact overlapped region M, exists around  $V_{bg} = -26$  V in our measurements, resistances at the charge neutrality points do not increase with the displacement field for  $V_{bg} < -7.5$  V. However, it is obvious that the displacement field leads to an increase of resistances and widths of the Dirac peaks for  $V_{bg} > 0$  V, which is the sign of a band gap opening. Finally, an insulating state has not been reached, therefore, the band gap is not fully open in our measurements. We calculate that the displacement field is  $\tilde{D} = 0.84$  V/nm at  $V_{bg} = 34$  V and  $V_{tg} = -1.75$  V, and the corresponding resistivity is only 3 k $\Omega$ / $\square$ .

According to Equation (3.30), a band gap of 63.1 meV is expected for  $\tilde{D} = 0.84$  V/nm. The large gap predicted theoretically is hardly realized in transport experiments. Apart from this, some experimental groups have reported an insulating state with a gap size about a few meV [10, 23, 46], while the others have found that samples exhibit good metallic properties [12] as we have observed. The reasons that affect the gap opening are under debate. At high temperatures (2 K  $\sim$  100 K), the suppression of the gap size can be attributed to thermal activation [10, 23, 47]. In an ideal defect-free bilayer graphene, the maximum resistance in high displacement fields varies with the temperature as

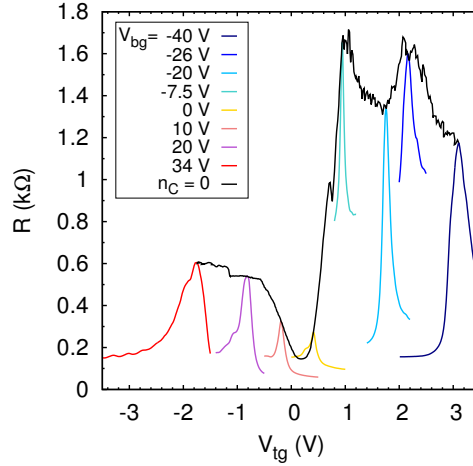


**Figure 3.10:** Resistance versus top-gate voltage for various back-gate voltages. The black curve shows resistances along the displacement field axis, i.e.  $n_C = 0$ .

$R_{max} \propto \exp(u_g/2k_B T)$  [10, 23, 48], where  $k_B$  is Boltzmann's constant. An energy of  $u_g/2$  is needed for the carrier to be activated from the Fermi level in the metal lead to the conduction band or valence band of graphene. At low temperatures, the mechanisms are different. In diffusive graphene, the presence of disorder may account for the suppression of the gap [23, 49, 50]. The charge carriers are localized in mid-gap states which are created by disorder and smear out the gap. Hopping processes between those localized states dominate the transport. Recently, a new explanation was put forward. In pristine bilayer graphene, there are stacking walls between AB and BA stacked domains [51]. Ju et. al. have reported that the chance to open a band gap is small in the presence of stacking walls but large when measuring within the same domain [52]. However, San-Joe et. al. have measured an insulating state in their suspended device with stacking walls [53]. Koshino et. al. have predicted theoretically that the stacking boundary is either insulating or highly transparent depending on the crystallographic direction of the boundary [54]. In the low-energy region, the boundary is almost insulating in armchair AA stacking and zigzag SP stacking (atoms in two layers do not overlap) while it is highly transparent in armchair SP stacking and zigzag AA stacking. Further investigations are needed to reveal the mechanisms of gap opening in bilayer graphene.

### 3.3.3 Contact resistance for one-dimensional edge contacts

Benefiting from the one-dimensional edge contacts, we observe a low contact resistance. In two-terminal measurements, the contact resistance can be estimated from the minimum resistance  $R_{min}$  at high charge carrier density. For example, we obtain  $41.1 \Omega$  as the minimum resistance for sample BL12C at a density of  $n = -2.9 \times 10^{12} \text{ cm}^{-2}$ . The corresponding contact resistance  $R_c$  is normalized by the width of the channel, i.e.

$R_{min}/2 \times W \approx 102 \Omega \mu\text{m}$ , in order to compare with the other devices. The contact resistances of the two devices are about  $93 \sim 103 \Omega \mu\text{m}$  at  $n \sim -3 \times 10^{12} \text{ cm}^{-2}$ , which is roughly half of the contact resistance measured on the surface connected graphene [55]. The reduction in the contact resistance comes from the shorter bonding distance in Ti-O-C edge contacts. The oxygen on the edge of graphene comes from the  $\text{O}_2$  etching, which is performed before the metal deposition for the edge contacts, as described in Chapter 2. The oxygen improves the binding as well as the transmission at the interfaces. Comparing to the first paper on edge contacts [14], we obtain a much lower  $R_c$ , which is attributed to the ultra high vacuum during metal deposition ( $\sim 10^{-9}$  mbar). The contact resistances we have extracted include the quantum resistance  $R_Q = \frac{h}{4e^2} \frac{1}{M}$ , where  $M = \text{int}(\frac{2W}{\lambda_F})$  is the number of the conduction modes. We exclude the  $R_Q$  from the  $R_c$  and obtain the extrinsic contact resistances  $(R_c - R_Q/2) \sim 60 - 70 \Omega \mu\text{m}$ , which depend on the transparency of the contact interfaces.

### 3.4 Fabry-Pérot interference in ballistic bilayer graphene p-n-p junctions

Fabry-Pérot interference is expected to occur in ballistic graphene p-n junctions, where the mean free path of charge carriers is larger than the length of the cavity. The mean free path of our devices, fabricated with encapsulated bilayer graphene, reaches  $8.8 \mu\text{m}$  at a density of  $-3.3 \times 10^{12} \text{ cm}^{-2}$ . Hence, our samples should be suitable to study phase-coherent transport in bilayer graphene.

We investigate the Fabry-Pérot interference by measuring the conductance. Figure 3.11a shows the color plot of the conductance versus  $V_{tg}$  and  $V_{bg}$  for the sample BL12D, which is shorter in length than sample BL12C. The conductance map is similar to that of sample BL12C shown in Figure 3.9a. The two horizontal lines at  $V_{bg} = -4.3 \text{ V}$ ,  $-27.3 \text{ V}$  indicate the charge neutrality points in only-back-gated regions L and R (bare bilayer graphene), and M (metal contact overlapped bilayer graphene), respectively. The additional line at  $V_{bg} = -27.3 \text{ V}$  originates from the overlapped contact in the region M and gives rise to n-doping. The diagonal line corresponds to the charge neutrality point in the dual-gated region C. It also determines the axis of the displacement field.

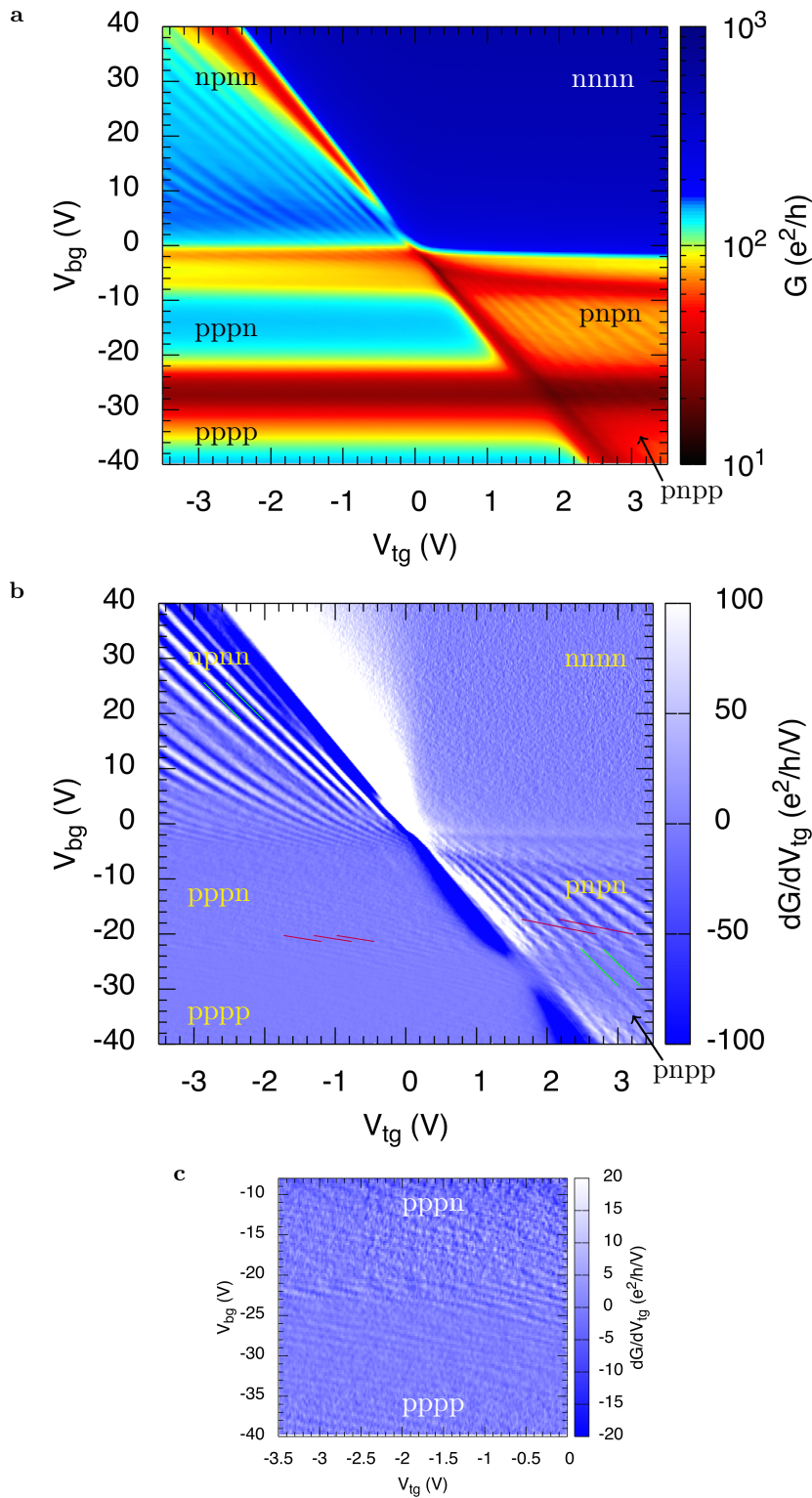


**Figure 3.11:** Fabry-Pérot interference observed in conductance measurements. (a) Colormap of the conductance as a function of the  $V_{tg}$  and  $V_{bg}$  for sample BL12D. The measurements have been performed at 4 K and zero magnetic field. (b) Transconductance of (a). The purple and green solid lines show the interference fringes induced by the back-gate only and dual-gate, respectively. The interference pattern in the  $pppn$  and  $pppp$  regimes are highlighted in (c).

In Figure 3.11a, we observe strong conductance oscillations in the bipolar regime, which are due to Fabry-Pérot interferences. The Fabry-Pérot fringes are nearly parallel to the diagonal charge neutrality line, indicating that the interference takes place in the dual-gated region C, where the Fermi level is affected by both the top- and back-gates. The intensity of the interference can be inferred from the visibility of the Fabry-Pérot fringes. In general, the amplitudes are large in ultra-clean devices, where the disorder-induced backscattering is weak. In our case, the high visibility of the interference patterns indicates the high quality of our device.

In order to analyze the fine interference patterns, especially for the unipolar regime, we remove the non-uniform conductance profile by using the transconductance  $dG/dV_{tg}$ . The corresponding  $dG/dV_{tg}$  for the conductance in Figure 3.11a is shown in Figure 3.11b. In the following, we explain the formation of Fabry-Pérot fringes in the six different cases.

### **Fabry-Pérot interference in the unipolar regime**

**Resonance in the nnnn regime.** In Figure 3.11b, no interference patterns are visible in the nnnn regime. The Fabry-Pérot interference vanishes. To understand this phenomenon, we sketch the potential profile together with the band diagrams in Figure 3.12. The four regions of the device, i.e. L, C, R, M, are portrayed within the grey dashed rectangle. The two outer regions, labeled as edge, describe the edges of bilayer graphene that contacted by the metal leads. These edges are heavily n-doped because of the metal leads. The Fermi level for each region is shown in the band spectrum. In the case of the nnnn regime, depicted in Figure 3.12b, the charge carriers have the same polarity n in all regions. Therefore, there is no p-n interface formed anywhere. Therefore Fabry-Pérot interference cannot appear due to the absence of cavity.

**Resonance in the pppp and pppn regimes.** In Figure 3.11b, we observe weak conductance resonances in the pppp and pppn regimes. The interference fringes are parallel to the purple solid lines. For a better visibility, we zoom into the pppp and pppn regions and show the patterns explicitly in Figure 3.11c. In the case of the pppp regime, the potential profile is shown in Figure 3.12e. As the Fermi level in the edges is approximately constant as in the metal leads, the edge regions are always heavily n-doped. On the other hand, the Fermi level of the entire device is tunable by modulating the back-gate voltages  $V_{bg}$ . When we tune the Fermi level to the valence band in the entire device, two p-n junctions are formed along the two edges of the device. A large cavity is formed between the two p-n interfaces. As indicated by the purple arrows in Figure 3.12e, the cavity covers the whole device, i.e. the regions L-C-R-M. Since this cavity is much larger than the one in the dual-gated region C, the interference patterns are less visible in the pppp regime, because the charge carriers are partially scattered when traveling within the cavity, leading to the low amplitudes of the conductance

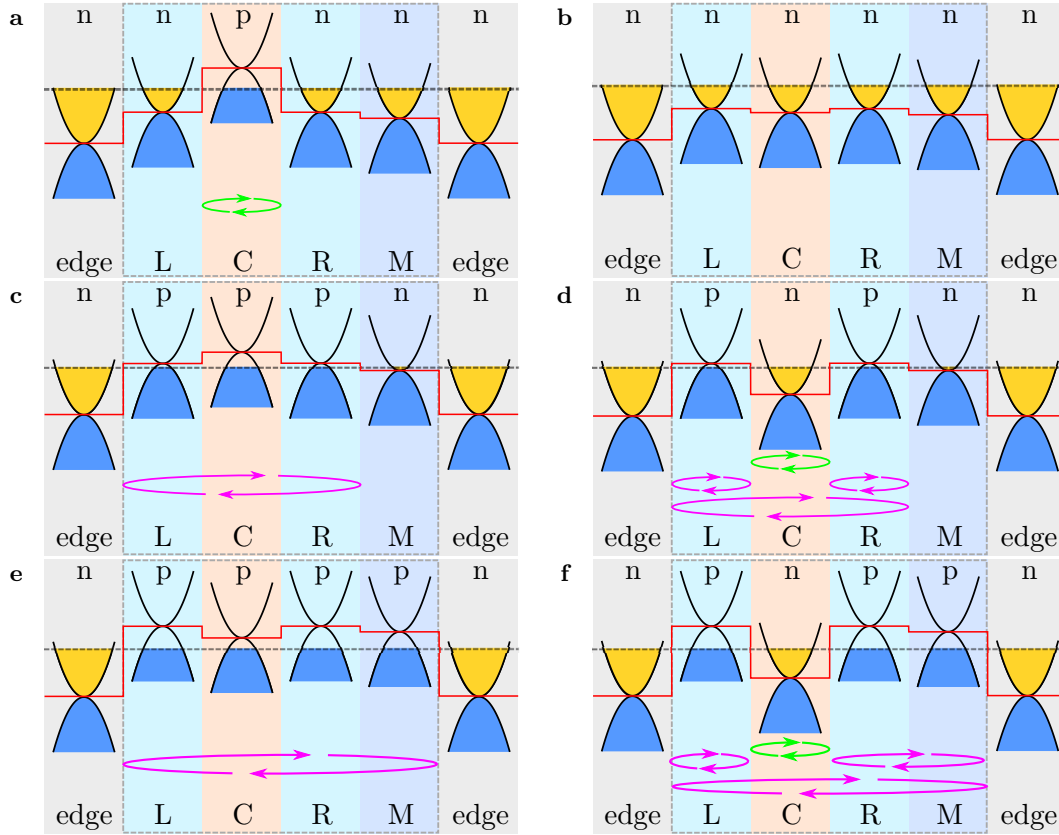


**Figure 3.12:** The potential profiles and the band diagrams in the cases of different charge polarity combinations. According to Figure 3.11a, 6 combinations are npnn (a), nnnn (b), pppn (c), npn (d), pppp (e) and pnpp (f). In each sketch, the different regions in the sample are labeled at the bottom, the corresponding charge polarities are denoted at the top. The device consists of four regions, i.e. L, C, R, M, which are arranged in the grey dashed rectangular. Outside the rectangular, two regions are labeled as edge, which describe the edges of bilayer graphene that contact the metal leads. The metal leads induce nearly constant n-doping in the edge regions. The grey dotted line marks the position of the Fermi level. The red solid line shows the potential profile. The green arrows denote the cavity created in the dual-gated region, while the purple arrows label the cavities that are tuned by the back-gate voltages.

resonances. In the case of the pppn regime, the formation of the interference fringes is similar to the situation in the pppp regime. In Figure 3.12c, the cavity is also marked with the purple arrows which go through three regions L-C-R. The interference patterns have the same orientation as the ones in the pppp regime because the Fermi levels are tuned by the back-gate in both cases. However, since the cavity L-C-R in the pppn regime is smaller than L-C-R-M in the pppp regime, the visibility of the interference fringes is better, as presented in Figure 3.11c.

### Fabry-Pérot interference in the bipolar regime

**Resonance in the npnn regime.** In the bipolar regime, the Fabry-Pérot fringes in

the npnn regime are simple in contrast to the ones in the pnpp or pnpn regimes. In the npnn regime, the resonance lines are nearly parallel to the displacement field axis, marked by the green lines in Figure 3.11b. Thus, the resonance patterns depends on both the back-gate and top-gate voltages. As shown in Figure 3.12a, a cavity is formed by tuning the Fermi level in the region C to the valence band, and the Fermi level in the other regions to the conduction band. The cavity is labeled by the green arrows.

**Resonance in the pnpp and pnpn regimes.** The Fabry-Pérot fringes in the pnpp or pnpn regimes are more complicated. As shown in Figure 3.11b, there are two sets of resonance lines existing in these two regimes. One set is denoted by the purple lines, which is similar to the resonance lines in the pppp and pppn regimes. Another set is parallel to the displacement field axis, labeled as the green lines. This set is most prominent and formed by the same cavity as in the npnn regime. The corresponding potential profiles are shown in Figure 3.12f and Figure 3.12d for the pnpp and pnpn regimes, respectively. In the region C, a cavity, marked by the green arrows, is created by applying top-gate voltages to tune the Fermi level within the conduction band, where the charge polarity is opposite to it in the neighboring regions. This cavity is responsible for the interference patterns parallel to the green lines in Figure 3.11b. In the pnpp regime, three cavities marked by the purple arrows, i.e. L, R-M, L-C-R-M, determine the resonance lines along the direction of the purple lines in Figure 3.11b. Although those three cavities have different lengths, they are tuned by the back-gate at the same time. Hence, the patterns induced by each cavity have the same orientation, but different period and amplitude. The shorter the cavity is, the larger are the period and amplitude. In the pnpn regime, the patterns along the purple lines arise from three cavities, L, R, L-C-R, as shown in Figure 3.12d. The difference between pnpp and pnpn regimes lies in two cavities, R-M in the pnpp regime and R in the pnpn regime. Both of them correspond to the resonance lines parallel to the purple lines. But the length of R is much shorter than the length of R-M, which resulting in the enhanced visibility for the resonances along the purple lines in the pnpn regime.

In this section, we have presented the results on the Fabry-Pérot interference. We directly observe the Fabry-Pérot interference on conductance measurements both in the unipolar and bipolar regimes. This implicates that the devices are clean and ballistic. Until now, ballistic Fabry-Pérot interference has only been realized on monolayer graphene p-n junctions by Young et. al. [8], Rickhaus et. al. [56], and on bilayer graphene p-n junctions by Varlet et. al. [12]. However, most of their results show weak conductance oscillations which are only visible in the transconductance. Only Rickhaus have observed the interference fringed directly in conductance measurements for a suspended graphene p-n junction. But the suspended devices are limited for applications. The devices, made with encapsulated bilayer graphene, have a good quality comparable

with the suspended devices, but provide more possibilities to design devices for various applications.

### Periods of Fabry-Pérot interference

The Fabry-Pérot interference is a phase-coherent effect. The amplitudes of the conductance are determined by the phase difference between the two transmitted waves, that is  $\Delta\theta = 2\Delta k L_{cavity}$ . The constructive peaks occur when  $\Delta\theta = 2j\pi$  with  $j$  being an integer. An example of Fabry-Pérot interference is shown as red curve in Figure 3.13. The curve is measured at  $V_{bg} = -14$  V in the pnpn regime on sample BL12D. The conductance  $G$  is a function of the charge carrier density  $n_C$  in the dual-gated region C.  $n_C$  is determined by  $n_C = \text{sgn}(E)k^2/\pi$ . We differentiate  $n_C$  with respect to  $k$  and obtain  $\Delta n_C = \text{sgn}(E)2k\Delta k/\pi$ . If we take the relations  $k = \sqrt{\pi|n_C|}$  and  $\Delta k = \pi/L_{cavity}$  into consideration, we deduce that the period of the constructive oscillations are tied to the length of the cavity by  $\Delta n_C = 2\sqrt{\pi|n_C|}/L_{cavity}$ .

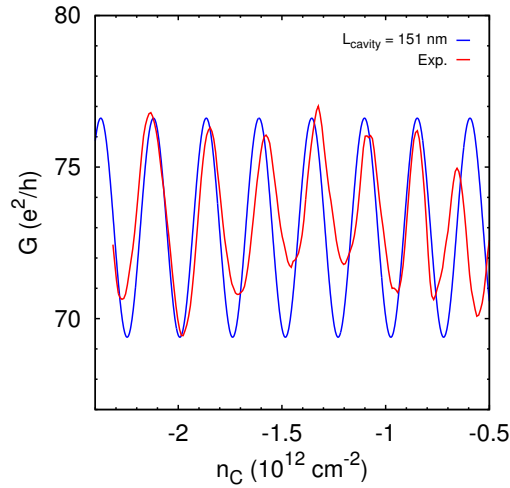


**Figure 3.13:** Conductance oscillations in the pnpn regime measured on sample BL12D. The conductance is presented with respect to the charge carrier density  $n_C$  in the dual-gated region C. The back-gate voltage is fixed at  $V_{bg} = -14$  V. The red curve shows the experimental data, while the blue curve is obtained from fitting of the experimental data using the discrete Fourier transformation. The blue curve corresponds to a cavity length of 151 nm.

We employ discrete Fourier transformation to determine the length of the cavity, which is related to the period in Figure 3.13. For convenience, we change the variable from  $n_C$  to  $k$ . The Fourier transformation is performed from  $k$  space to the  $L_{cavity}$  space. The dominant periodicity in Figure 3.13 is related to a cavity size of  $\sim 151$  nm, which is very close to the width of the top gate 150 nm. The fitting result is plotted as the blue curve in Figure 3.13.

In the bipolar regime, the periods of the oscillations are not constant, as noticed in Figure 3.14a. The conductance is taken at  $V_{bg} = 0$  V. The distance  $\Delta n_C$  between

two neighboring peaks is enhanced at high charge carrier density. In Figure 3.14b, we extract the periods  $\Delta n_C$  for a number of conductance curves taken at different back-gate voltages in Figure 3.11a. The resulting periods  $\Delta n_C$  are presented as a function of the displacement field. As the displacement field increases, the height of the potential profile rises. As a consequence, the cavity in the dual-gated region reduces its length, leading to a larger  $\Delta n_C \sim \frac{1}{L_{cavity}}$ .

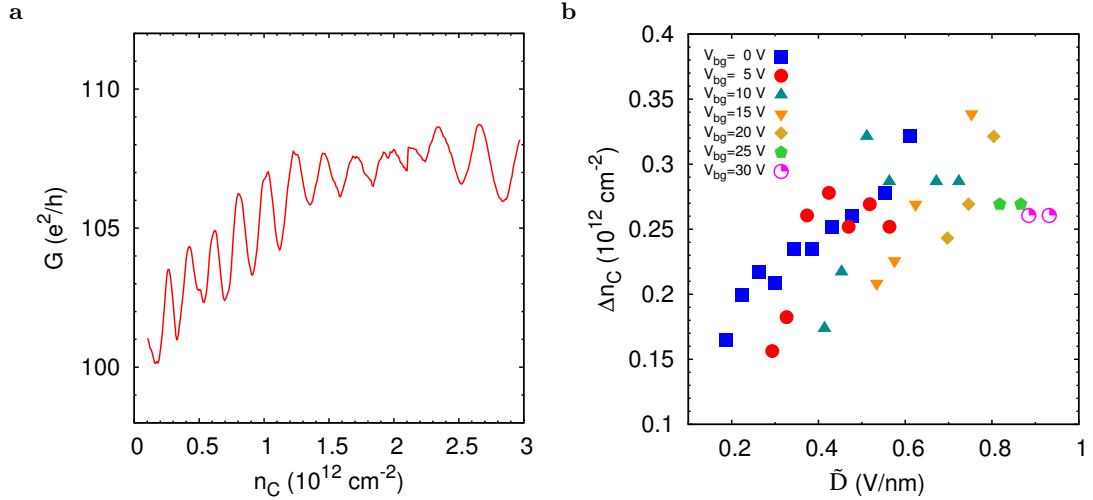


**Figure 3.14:** The periods of conductance oscillations in the bipolar regime (npnn). (a) An example of the conductance oscillation varies with  $n_C$ . The data is taken at  $V_{bg} = 0$  V. The oscillation periods are not constant. (b) The oscillation period  $\Delta n_C$  increases with the displacement field.

The discrete Fourier transformation has been used to analyze the cavity size in the unipolar regime, i.e. pppp and pppn. For sample BL12D, we obtain  $L_{cavity} = 721$  nm for the pppp regime and  $L_{cavity} = 536$  nm for the pppn regime, respectively. On the other hand, we have measured the lengths of the cavity according to the AFM measurements. In the pppp regime, the cavity L-C-R-M is about 800 nm long. And in the pppn regime, the length of the cavity L-C-R is about 603 nm. Therefore, the cavity length extracted with the Fourier transformation is consistent with the geometry of the sample.

The amplitudes of the conductance oscillations depend on the transmission probability of the cavity. The oscillations are visible as long as the reflection and transmission probabilities are comparable at the p-n interface. If the interface is very transparent for electrons, there will be no trapped electrons in the cavity. On the contrary, the electrons will not enter the cavity if the p-n interface is too reflective. For bilayer graphene with an atomically sharp potential barrier, the electron undergoes perfect reflection at the normal incident angle in the absence of a band gap. Hence, an oblique p-n interface assists the quasiparticle interference due to the selective transmission with respect to the incident angles. In the bipolar regime, the application of the top gate generates two oblique potential steps between the n- and p- type charge carriers. The non-zero

incident angles give rise to the high visibility of the Fabry-Pérot resonances. However, in the unipolar regime, the situation is different. The p-n junctions are only available in the cases of pppn or pppp regimes. The potential steps created by the heavily n-doped leads are relatively sharp because the potentials decay rapidly close to the leads. Thus, a large number of incident carriers with angles close to 0 are reflected. The resulting amplitudes of the Fabry-Pérot resonances are small.

### 3.5 Fabry-Pérot oscillations at low magnetic fields

Anti-Klein tunneling is expected to occur at normal incidence in bilayer graphene, as shown in Figure 3.4. However, the conductance at zero field is an integration of all possible incident angles. It is possible to study anti-Klein tunneling using a Fabry-Pérot interferometer at low magnetic fields [8, 33], where the quantum Hall regime has not yet emerged. When a low magnetic field is applied, the trajectories of electrons are bent because of the Lorentz force, and follow cyclotron orbits. The radius of the cyclotron motion is larger than the length of cavity in the low magnetic fields, therefore quantum interference can occur. The Fabry-Pérot resonances appear if the phase difference between the neighboring transmitted waves satisfies

$$\Delta\theta = \theta_{WKB} + \theta_{AB} + \theta_{Berry} = 2n\pi, n \in Z. \quad (3.31)$$

Here,  $\theta_{WKB} = \frac{1}{\hbar} \int_{-a}^a p_x(x') dx'$  is the Wentzel-Kramers-Brillouin (WKB) phase. The closed loop formed by different paths encloses an area  $\delta A$  and gives rise to an Aharonov-Bohm phase  $\theta_{AB} = eB\delta A/\hbar$ .  $\theta_{Berry}$  is the Berry phase that is illustrated in Section 3.1.3.

The Fabry-Pérot oscillations in a low magnetic field are shown in Figure 3.15. The measurements have been performed at  $V_{bg} = 20$  V. Figure 3.15 presents the variations of  $dG/dV_{tg}$  as a function of the top-gate voltage  $V_{tg}$  and the magnetic field  $B$ . It is evident that the fringes disperse with  $B$  and behave differently at  $V_{tg}$  far away from the charge neutrality point (CNP) ( $< -2.3$  V) and at  $V_{tg}$  close to CNP ( $-2.3 \sim -1$  V). In the region away from the CNP, the fringes disperse parabolically with respect to  $B$ , while the fringes change linearly with  $B$  in the region close to the CNP. When tuning the Fermi level away from the CNP, a shift in Fabry-Pérot fringes occurs at a certain  $B$  in the range of  $100 \text{ mT} \sim 300 \text{ mT}$ . We note that the shift in period increases with  $V_{tg}$ , and reaches a half-period at  $V_{tg} \approx -1.4$  V, which indicates that a Berry phase of  $\pi$  exists. This is similar to the case of single-layer graphene, as demonstrated by Young et al. [8]. Then, the shift in period decreases as we continuously tune the  $V_{tg}$  away from the CNP. The shift almost disappears at the left-most fringe, where the Berry phase is nearly  $2\pi$ . Therefore, by tuning the Fermi level with the top gate, the Berry phase changes

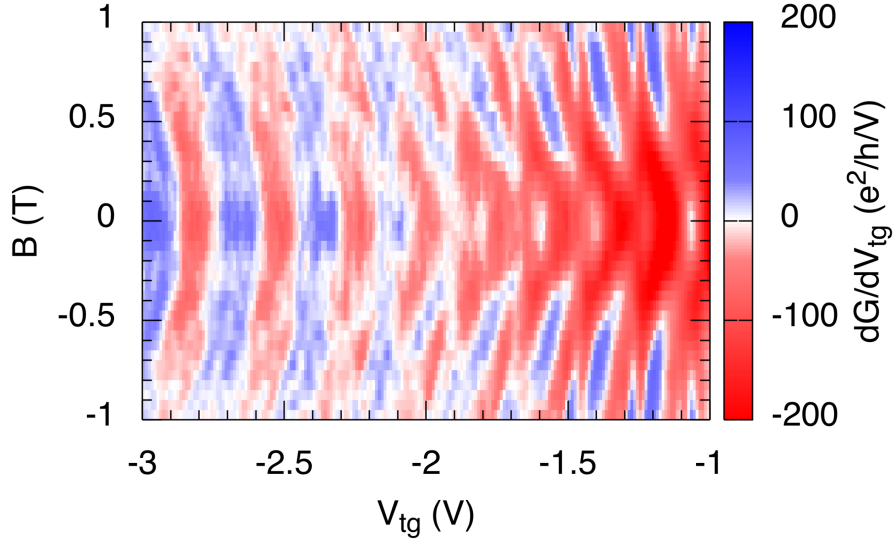


**Figure 3.15:** Effect of low magnetic fields on Fabry-Pérot oscillations (sample BL12C) at 4.2 K. The transconductance are shown as a function of  $V_{tg}$  and magnetic field  $B$ . The map is measured at  $V_{bg} = 20$  V in the npnn regime.

continuously from 0 to  $2\pi$ . This is inconsistent with the conventional Berry phase of  $2\pi$  in gapless bilayer graphene. However, in gapped bilayer graphene, the Berry phase can take values from 0 to  $2\pi$ , as we discussed in Section 3.1.3.2. Varlet et. al. [12] have observed the Berry phase of  $1.22 \sim 1.46\pi$  in gapped bilayer graphene.

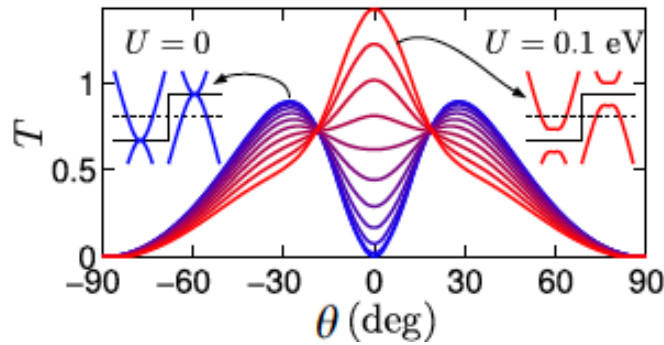


**Figure 3.16:** The angular transmission probability for a sharp potential. In the presence of a band gap, anti-Klein tunneling transits to Klein tunneling. Figure from Ref. [12].

The Berry phase in bilayer graphene differs from that in single-layer graphene. In single-layer graphene, the Berry phase of  $\pi$  requires that the trajectories of the reflected electrons form closed loops that enclose the origin in the momentum space. This is not the case as the electrons bounce back and forth between two parallel interfaces at zero or very small magnetic field, which is possible when the magnetic field is strong enough, but still weak in comparison with the quantum Hall regime [33]. At this magnetic field, the phase suddenly jumps by  $\pi$ . Thus the Berry phase in single-layer graphene depends

on the magnetic field. However, in bilayer graphene, a non-trivial Berry phase can be picked up even in zero magnetic field as long as the interlayer symmetry is broken by gating. The Berry phase is  $2\pi$  only in the absence of the interlayer asymmetry. It is predicted that the interlayer asymmetry disrupts the anti-Klein tunneling [12], as shown in Figure 3.16. Anti-Klein tunneling evolves into Klein tunneling at the normal incident angle as the asymmetry parameter varies. Since the transmission becomes finite, the paths of electrons can pass  $k = 0$  even at  $B = 0$ . The Berry phase is independent of the magnetic field, and ranges from 0 to  $2\pi$  depending on the asymmetry parameter  $u$ .

### 3.6 Conclusion

In conclusion, we have investigated a device consisting of a hBN-BLG-hBN heterostructure and two edge contacts. The device is characterized at 4.2 K. We observe strong conductance oscillations due to the Fabry-Pérot interference at zero magnetic field. At low magnetic fields, we perform conductance measurements in the npnn regime. The phase shifts appear when tuning the Fermi level close to the band edge. On the contrary, the phase shifts vanish at high charge carrier density. This illustrates a transition from anti-Klein tunneling to Klein tunneling in the presence of interlayer asymmetry. The corresponding Berry phase ranges from 0 to  $2\pi$ .

## Chapter 4

# Proximity-induced superconductivity in bilayer graphene p-n-p junctions

### 4.1 Introduction to proximity-induced superconductivity

In 1911, the Dutch physicist H. Kamerlingh Onnes observed an abrupt vanishing of the resistivity of solid mercury at  $T=4.15$  K, which is referred to as superconductivity [57]. J. Bardeen, L. Cooper, and J. R. Schrieffer showed that superconductivity is due to the formation of Cooper pairs, bound electron pairs of (in most cases) opposite momentum and spins. The Cooper pairs in a superconductor obey Bose-Einstein statistics and form a coherent superconducting condensate that can be characterized by a single macroscopic wave function  $\psi = |\psi| e^{i\varphi}$ , with a common phase  $\varphi$ . When placing a normal metal close to a superconductor, a finite amplitude of the pair function can be induced in the normal metal, which is referred to as the proximity effect. The mechanism of proximity effect in normal metals can be interpreted as Andreev reflections.

In the following, we specify the theoretical background of proximity-induced superconductivity in the conventional as well as the graphene-based Josephson junctions.

#### 4.1.1 Josephson effect

The Josephson effect was predicted by Brian D. Josephson in 1962 [58] in the basis of the BCS theory. When two superconductors are connected by a weak link [59], a Josephson junction is formed, as depicted in Figure 4.1. Such a weak link can be a geometric

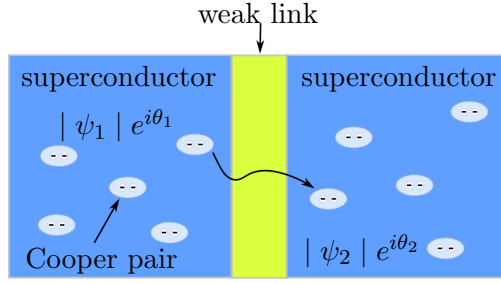


**Figure 4.1:** Sketch of a Josephson junction. The two superconductors are connected with a weak link, which can be a micro-constriction, an intermediate normal metal, or a semiconductor.

constriction point contact, an intermediate normal metal and even a semiconductor. In the original work of Josephson, a thin insulating barrier is used, but the Josephson effect has been generalized for different types of weak links. If two superconductors are placed close enough, the macroscopic wave functions of the two superconductors overlap, so that Cooper pairs can be transferred via the weak link which in turn induces a supercurrent flow between the superconductors with zero voltage drop. The supercurrent is related to the phase difference between the two coupled superconductors, which is obtained by the following current-phase relation

$$J_s = J_c \sin \varphi. \quad (4.1)$$

Equation (4.1) is known as the first Josephson equation. The supercurrent density  $J_s$  oscillates sinusoidally with the phase difference  $\varphi = \theta_2 - \theta_1$  across the junction in the absence of any scalar and vector potentials. The second Josephson equation defines the voltage-phase relation, reading

$$\frac{\partial \varphi}{\partial t} = \frac{2eV}{\hbar}. \quad (4.2)$$

The Josephson effect is governed by Equation (4.1) and Equation (4.2). For zero voltage, i.e.  $V = 0$ , the phase difference is a constant, leading to a current density up to a critical current density  $J_c$ . This is called the d.c. Josephson effect. For  $V \neq 0$ , the phase difference  $\varphi$  varies with time, according to the second Josephson equation, it has the analytical solution  $\varphi = \varphi_0 + (2e/\hbar)Vt$ . Thus, the supercurrent in the first Josephson equation is written as

$$J_s = J_c \sin(\varphi_0 + (2e/\hbar)Vt), \quad (4.3)$$

which is alternating with a frequency of  $\omega = 2eV/\hbar$ . This is known as the a.c. Josephson effect.

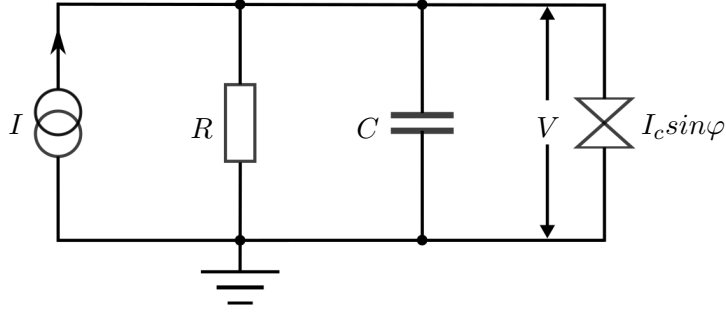


**Figure 4.2:** Equivalent circuit for the resistively and capacitively shunted junction (RCSJ) model.

#### 4.1.2 The resistively and capacitively shunted junction model

Under a current bias, a classic Josephson junction is equivalent to a resistively and capacitively shunted junction (RCSJ) [60], as sketched in Figure 4.2. The resistor  $R$  represents the normal state resistance, and the capacitor  $C$  is taken as the capacitance of the Josephson junction. At finite voltage, the total current in a Josephson junction consists of three major components: the Josephson current  $I_s$ , the normal current  $I_N$ , and the displacement current  $I_D$ . Here we neglect the fluctuation current  $I_F$  induced by noise since its contribution is small at low temperatures. In contrast to the Josephson current, the normal current originates from quasiparticles tunneling at the finite voltage-state. The displacement current is due to the finite capacitance of the Josephson junction. The total current is expressed as

$$I = I_c \sin \varphi + \frac{V}{R} + C \frac{dV}{dt}. \quad (4.4)$$

With the consideration of the voltage-phase relation Equation (4.2), the current is described by the following differential equation

$$I = I_c \sin \varphi + \frac{\hbar}{2eR} \frac{d\varphi}{dt} + \frac{\hbar C}{2e} \frac{d^2\varphi}{dt^2}. \quad (4.5)$$

The equation of motion defined by Equation (4.5) is analogous to that of a particle with mass  $(\frac{\hbar}{2e})^2 C$  and damping  $(\frac{\hbar}{2e})^2 \frac{1}{R}$  moving in a potential  $\frac{\hbar I_c}{2e} (1 - \cos \varphi - \frac{I}{I_c} \varphi)$ . This potential is called the tilted washboard potential. We define the Stewart-McCumber parameter  $\beta_C$  as the ratio of the time constant  $\tau_{RC} = RC$  to the characteristic time constant  $\tau_c = \frac{\hbar}{2eI_c R}$  that is associated with the phase evolution across the junction. The relation between  $\beta_C$  and the quality factor  $Q$  is expressed as  $\beta_C = Q^2$ . By using the Stewart-McCumber parameter  $\beta_C = \frac{2e}{\hbar} I_c R^2 C$  and the normalized time  $\tau = \frac{t}{2eI_c R/\hbar}$ , Equation (4.5) is rewritten as

$$\frac{I}{I_c} = \beta_C \frac{d^2\varphi}{dt^2} + \frac{d\varphi}{dt} + \sin \varphi. \quad (4.6)$$

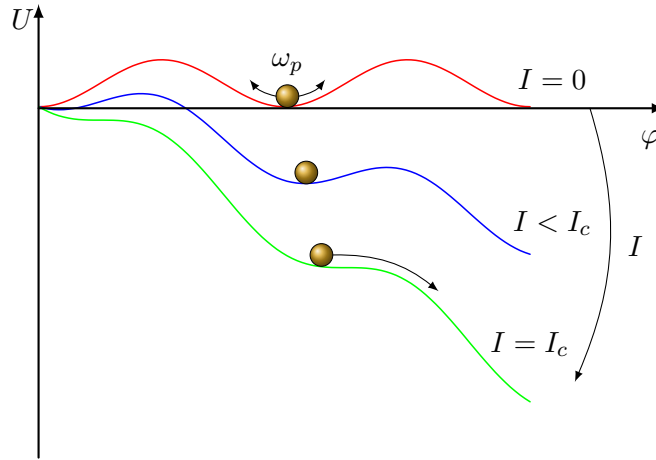


**Figure 4.3:** The damped motion of a quasiparticle in the tilted washboard potential, models the evolution of the phase difference between the 2 superconducting leads of a Josephson junction.

The motion of the quasiparticle in a tilted washboard potential is depicted in Figure 4.3. If the bias current is zero, i.e.  $I = 0$ , the particle oscillates with the plasma frequency  $\omega_p = \sqrt{\frac{2eI_c}{\hbar C}}$  around a minimum of the periodic horizontal potential. The washboard potential tilts with increasing bias current, as schematically shown in Figure 4.3. As long as  $I < I_c$ , the particle stays in the minimum of the potential, which corresponds to the zero-voltage state. When  $I$  reaches  $I_c$ , the particle starts to move out because there is no minima in the potential, which corresponds to a finite voltage state. It is noteworthy that, for  $I < I_c$ , the particle can escape from the potential by thermal excitation and by (macroscopic) tunneling.

The competition between the viscous damping and the inertia of the particle plays an important role in the hysteresis behaviour of the  $I - V$  curves in the case of  $I < I_c$ . The hysteresis is described by the Stewart-McCumber parameter  $\beta_C$ . Figure 4.4 illustrates the  $I - V$  curves for  $\beta_C$  in three different limits. For an overdamped Josephson junction ( $\beta_C \ll 1$ ), the capacitance and/or resistance of the junction are small. In the tilted washboard model, this regime is equivalent to the mass of the particle being small and the damping large, since the mass is proportional to the capacitance  $C$  and the damping is inversely proportional to the resistance  $R$ . The junction immediately switches to the zero-voltage state as  $I$  decreases below  $I_c$  due to the small inertia of the particle. In this situation, the time required for the charge on the capacitor to relax is almost instantaneous compared to the time scale  $\tau_c$ . There is no hysteresis on the  $I - V$  characteristics. However, for an underdamped Josephson junction ( $\beta_C \gg 1$ ), the capacitance and/or resistance of the junction are large and the damping is small. A bias current, which is much smaller than  $I_c$ , is required to stop the particle moving down the potential. In this case, the time scale  $\tau_c$  is much shorter than the time required for the charge on the capacitor to relax. A strong hysteresis of the  $I - V$  curves is observed.

For an intermediate regime, the amount of hysteresis is determined by the damping parameter  $\beta_C$ .

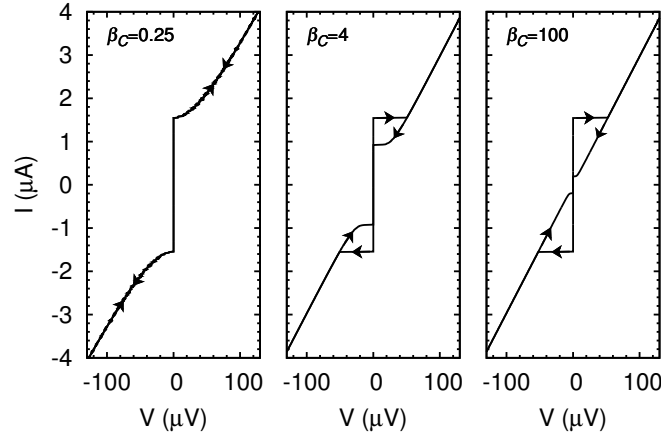


**Figure 4.4:** The hysteresis behaviour of the  $I - V$  curves for various  $\beta_C$ . As the  $\beta_C$  increases, the  $I - V$  curve realize a non-hysteresis to hysteresis transition.

It is important to note that the critical current depends on the temperature. As the temperature increases, the current fluctuation induced by the thermal background has to be taken into account. By adding a noise current  $I_F$  in parallel to the resistor  $R$  in the RCSJ model, the system is described by the stochastic differential equation

$$\frac{I}{I_c} + \frac{I_F}{I_c} = \beta_C \frac{d^2\varphi}{dt^2} + \frac{d\varphi}{dt} + \sin\varphi. \quad (4.7)$$

The random fluctuations of the current cause variations in the average slope of the tilted washboard potential. This makes it possible for a particle to escape from the minimum of the potential even before the critical current is reached. In the underdamped limit, the particle gains a velocity that is determined by the damping of the junction after it escapes from the potential well, so that it can roll down the tilted washboard potential. These fluctuations give rise to a premature critical tilt below which the particle is trapped, and a reduced critical current  $I_c$ . In the overdamped limit, the particle escapes from the potential maximum but does not obtain a velocity since the strong damping slows down the particle and traps it in a nearby potential. This process of escaping and retrapping leads to a diffusive behavior of particles with a finite average velocity. In the RCSJ model, this corresponds to a phase diffusion with a finite voltage supercurrent. In this process, the maximum supercurrent is reduced below the critical current.

### 4.1.3 Fraunhofer diffraction pattern

When placing a rectangular Josephson junction in a perpendicular magnetic field  $\vec{B} = (0, 0, B_z)$ , a magnetic flux  $\Phi$  penetrates an area, enclosed by the contour of the dashed blue

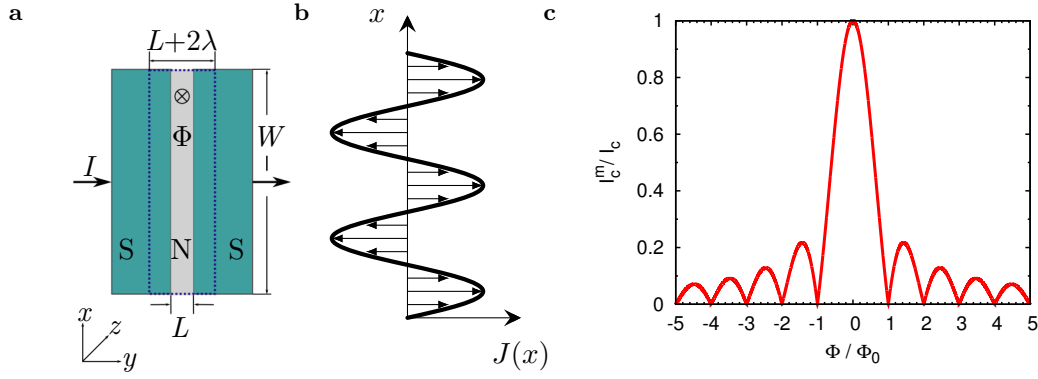


**Figure 4.5:** Sketch of Fraunhofer diffraction pattern in an extended Josephson junction. (a) Sketch of a Josephson junction in the magnetic field perpendicular to the plane of the junction. (b) Josephson current density along the superconducting leads. (c) Fraunhofer diffraction pattern for a homogeneous current density. Figures refers to Ref.[57].

line limited in  $y$  direction roughly by the thickness of the N and two times of the London penetration depth  $\lambda$ , as sketched in Figure 4.5a. The gauge invariant phase difference  $\varphi$  along the superconducting leads ( $x$ -axis) becomes non-uniform, but homogeneous in the direction parallel to the magnetic field ( $z$ -axis). In the junction plane, the total phase change along a closed contour equals  $2n\pi$ , resulting in a phase difference along the  $x$ -axis obeys the following function

$$\varphi(x) = \frac{2\pi}{\Phi_0} B_z (L + 2\lambda)x + \varphi_0 = \frac{2\pi\Phi}{\Phi_0} + \varphi_0. \quad (4.8)$$

Here,  $\Phi_0$  is the flux quantum,  $L$  is the length of the normal metal,  $\varphi_0$  is the phase difference at  $x = 0$ , and  $\Phi = B_z(L + 2\lambda)x$ .

The supercurrent density  $J_s(x) = J_c(x) \sin \varphi(x)$  oscillates sinusoidally along the  $x$ -axis with a period of  $\Delta x = \frac{\Phi_0}{B_z(L+2\lambda)}$ , which is dependent on the magnetic field, as depicted in Figure 4.5b. Thus, the magnetic flux within a single period is equivalent to one magnetic flux quantum,  $\Phi = B_z(L + 2\lambda)\Delta x = \Phi_0$ . As an example, Figure 4.5b shows the case of  $\Phi = \frac{5}{2}\Phi_0$ . The net supercurrent cancels to zero over a complete oscillation period, therefore, only one odd half-period contributes to the net supercurrent through the junction, which is given by

$$I_c(B_z) = \int_{-W/2}^{W/2} J_c(x) \sin(\varphi(x)) dx. \quad (4.9)$$

The integration in Equation (4.9) can be extended to the limit  $x \rightarrow \pm\infty$  because  $J_c(x)$  is zero outside the junction, i.e.  $J_c(x) = 0$  for  $|x| > W/2$ . The expression is then rewritten as

$$I_c(B_z) = e^{i\varphi_0} \int_{-\infty}^{\infty} J_c(x) e^{ikx} dx, \quad (4.10)$$

where  $k = \frac{2\pi}{\Phi_0} B_z (L + 2\lambda)$ . The phase factor  $e^{i\varphi_0}$  has no influence on the magnitude of the supercurrent so that the maximum Josephson current  $I_c^m(B_z)$  is given by

$$I_c^m(B_z) = \left| \int_{-\infty}^{\infty} J_c(x) e^{ikx} dx \right|, \quad (4.11)$$

which is the Fourier transform of the Josephson current density  $J_c(x)$ . For a homogeneous spatial distribution of the maximum Josephson current density, i.e.  $J_c(x) = J_c$ , the dependence of the maximum supercurrent on the magnetic field obeys the following relationship

$$I_c^m(\Phi) = I_c(0) \left| \frac{\sin \frac{\pi\Phi}{\Phi_0}}{\frac{\pi\Phi}{\Phi_0}} \right|. \quad (4.12)$$

Here,  $\Phi = B_z W (L + 2\lambda)$  is the magnetic flux through the junction and  $I_c(0) = J_c W$  is the maximum supercurrent at zero magnetic field. This function forms the well-known Fraunhofer diffraction pattern, as shown in Figure 4.5c, which is analogous to the diffraction pattern of light passing through a narrow slit. The minima of  $I_c^m$  refers to a number of full oscillation periods of the Josephson current density, which fits into the junction. Each period has a flux of  $\Phi_0$ .

#### 4.1.4 Andreev reflection

The proximity-induced superconductivity exists in a NS or SNS junction, where Cooper pairs in the superconductor can diffuse into the normal metal as phase correlated electron-hole states. This proximity effect is well understood by introducing the Andreev reflection. For electrons with an excitation energy of  $\varepsilon > \Delta$ , the incident electrons on the N/S interface reflect and transmit as normal quasiparticles. In the case of  $\varepsilon < \Delta$ , the incident electron from the normal metal cannot enter the superconductor unless it binds with another electron with opposite spin, forming a Cooper pair. This process gives rise to a hole retro-reflected back to the normal metal. The mechanism of Andreev reflection is schematically depicted in Figure 4.6. Since the incident electron and the reflected hole maintain the phase-coherent properties of Cooper pairs, the following conservation principles govern in the Andreev reflection processes:

- i) Charge is not conserved. A charge of  $2e$  is missing in the normal metal and transferred to the superconductor as a Cooper pair.
- ii) Energy is conserved. The incident electron has an excitation energy of  $\varepsilon$  above the Fermi energy, and the reflected hole has the same excitation energy below the Fermi energy.

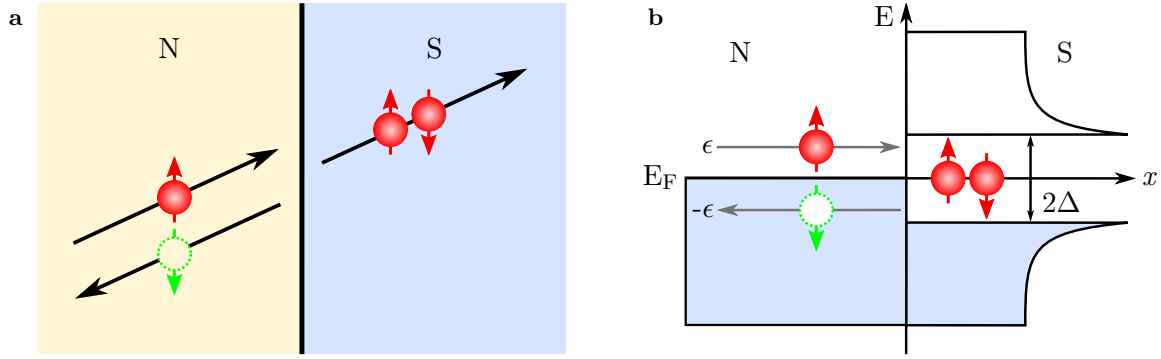


**Figure 4.6:** The schematics of an Andreev reflection process. (a) The Andreev reflection process at the N/S interface. An incident electron with spin-up (red filled circle) is reflected as a hole (green empty circle) with spin-down by the pairing potential. At the same time, a Cooper pair transfers into the superconductor. (b) The corresponding energy diagram.

iii) Spin is conserved. The spin of the reflected hole is opposite to that of the incident electron.

v) Momentum is approximately conserved at small excitation energy. The momentum of the reflected holes is defined as  $\vec{k}_h = \vec{k}_F - \vec{\delta k}$ , and the momentum of the incident electrons is denoted as  $\vec{k}_e = \vec{k}_F + \vec{\delta k}$ , where  $\delta k = \varepsilon/\hbar v_F$ . In the case of  $\varepsilon = 0$ , the momentum is conserved, so that the reflected hole exactly traces back the path of the incident electron.

The Andreev reflection is time-reversal symmetric, so that an incident hole can be reflected as an electron as well. Furthermore, the process of the Andreev reflection is phase coherent, thus the phases of the reflected hole  $\theta_h$  and the reflected electron  $\theta_e$  are defined as

$$\begin{aligned}\theta_h &= \theta_e + \varphi - \arccos(\varepsilon/\Delta), \\ \theta_e &= \theta_h - \varphi - \arccos(\varepsilon/\Delta),\end{aligned}\tag{4.13}$$

where  $\varphi$  is the phase difference of two superconductors. In the case of a NS junction,  $\varphi$  can be chosen to be zero by an appropriate gauge transformation. For charge carriers at the Fermi energy ( $\varepsilon = 0$ ), we have the relation:  $\arccos(\varepsilon/\Delta) = \pi/2$ .

#### 4.1.5 Blonder-Tinkham-Klapwijk (BTK) theory

The BTK theory is commonly used to describe the  $I - V$  characteristics in a NS junction [61]. We assume that the NS junction consists of an infinite normal metal and an infinite superconductor in the electrical contact at the N/S interface. The conduction

model in the NS junction is described by the Bogoliubov-de Gennes equations

$$\begin{pmatrix} -(H + \mu) & \Delta(x) \\ \Delta(x) & H + \mu \end{pmatrix} \begin{pmatrix} \Psi_e(x, t) \\ \Psi_h(x, t) \end{pmatrix} = \varepsilon \begin{pmatrix} \Psi_e(x, t) \\ \Psi_h(x, t) \end{pmatrix}, \quad (4.14)$$

where  $H = -\frac{\hbar^2}{2m}\nabla^2$  is the Hamiltonian of free electrons in a normal metal.  $\varepsilon > 0$  is the excitation energy, and  $\mu$  is the chemical potential or Fermi energy in the normal region.  $\Delta(x)$  is the spatially varying superconducting pairing potential, i.e.  $\Delta(x) = 0$  in the normal region but  $\Delta(x) = \Delta$  in the superconductor.  $\Psi_e(x, t)$  and  $\Psi_h(x, t)$  are the electron and the hole wave functions, respectively. The solution of Equation (4.14) bears the form

$$\Psi(x, t) = \begin{pmatrix} \Psi_e(x) \\ \Psi_h(x) \end{pmatrix} e^{-i\varepsilon t/\hbar}. \quad (4.15)$$

The four types of quasiparticle waves for a given energy are described as

$$\Psi_{\pm k^+} = \begin{pmatrix} u \\ v \end{pmatrix} e^{\pm ik^+ x}, \quad \Psi_{\pm k^-} = \begin{pmatrix} v \\ u \end{pmatrix} e^{\pm ik^- x}. \quad (4.16)$$

Here,  $k^\pm = \sqrt{2m}(\mu \pm \sqrt{(\varepsilon^2 - \Delta^2)})^{1/2}$ ,  $u(k > k_F)$  and  $v(k < k_F)$  are the electron-like and hole-like components of the two wave functions, respectively. According to the BCS theory, we have the following relationship

$$u^2 = \frac{1}{2} \left[ 1 + \frac{\sqrt{\varepsilon^2 - \Delta^2}}{\varepsilon} \right], \quad (4.17)$$

$$v^2 = \frac{1}{2} \left[ 1 - \frac{\sqrt{\varepsilon^2 - \Delta^2}}{\varepsilon} \right], \quad (4.18)$$

$$\varepsilon^2 = \left( \frac{\hbar^2 k^2}{2m} - \mu \right)^2 + \Delta^2. \quad (4.19)$$

We consider an incident electron at the N/S boundary, the incident electron wave  $\Psi_{inc}$ , the reflected electron wave  $\Psi_{ref}$  and the transmitted electron wave  $\Psi_{tran}$  are expressed as

$$\Psi_{inc}(x) = \begin{pmatrix} 1 \\ 0 \end{pmatrix} e^{iq^+ x}, \quad (4.20)$$

$$\Psi_{ref}(x) = a \begin{pmatrix} 0 \\ 1 \end{pmatrix} e^{iq^- x} + b \begin{pmatrix} 1 \\ 0 \end{pmatrix} e^{-iq^+ x}, \quad (4.21)$$

$$\Psi_{tran}(x) = c \begin{pmatrix} u \\ v \end{pmatrix} e^{ik^+ x} + d \begin{pmatrix} v \\ u \end{pmatrix} e^{-ik^- x}. \quad (4.22)$$

where  $k^\pm$  and  $q^\pm$  are the wave vectors in the superconducting and normal sides, respectively.  $\hbar q^\pm = \sqrt{2m}\sqrt{(\mu \pm \varepsilon)}$ .

The N/S interface is usually not transparent, and the interfacial scattering is taken into account by introducing a repulsive potential  $H\delta(x)$  at the interface. A dimensionless parameter is used to describe the barrier strength  $Z = H/\hbar v_F$ . The boundary conditions require the continuity of the wave functions at the interface  $x = 0$ :  $\Psi_N = \Psi_S$  and that the derivative of the wave functions satisfies  $(\hbar/2m)(\Psi'_S - \Psi'_N) = H\Psi(0)$  at the boundary. By applying the boundary conditions, we obtain the probability  $A(\varepsilon)$  of the Andreev reflection as a hole, the probability  $B(\varepsilon)$  of the normal reflection as an electron, the probability  $C(\varepsilon)$  of the transmission through the interface with a wave vector on the same side of the Fermi surface ( $q^+ \rightarrow k^+$ ), and the probability  $D(\varepsilon)$  of the transmission crossing through the Fermi surface ( $q^+ \rightarrow -k^-$ ). In the case of  $\varepsilon < \Delta$ , we have the following relationships

$$A(\varepsilon) = \frac{\Delta^2}{\varepsilon^2 + (\Delta^2 - \varepsilon^2)(1 + 2Z^2)^2}, \quad (4.23)$$

$$B(\varepsilon) = 1 - A, \quad (4.24)$$

$$C(\varepsilon) = D(\varepsilon) = 0. \quad (4.25)$$

For a transparent interface,  $Z = 0$ ,  $A(\varepsilon) = 1$ , the incident electrons are completely reflected as holes. At a finite  $Z$ , the incident electrons are partially Andreev reflected as holes ( $0 < A(\varepsilon) < 1$ ) and partially normal reflected as electrons ( $0 < B(\varepsilon) < 1$ ).

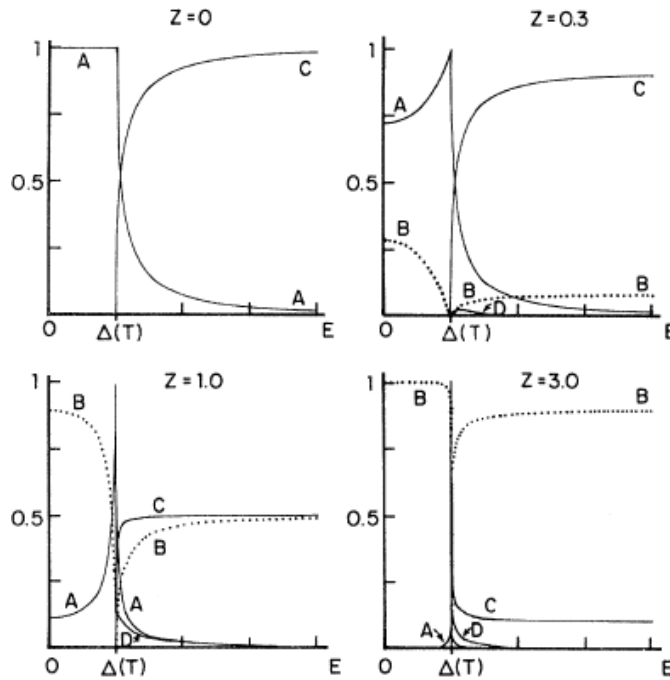


**Figure 4.7:** The reflection and transmission coefficient at the N/S interface for various barrier strength  $Z$ . Figure from Ref. [61].

In the case of  $\varepsilon > \Delta$ , the probability coefficients are expressed as

$$A(\varepsilon) = \frac{u^2 v^2}{\gamma^2}, \quad (4.26)$$

$$B(\varepsilon) = \frac{(u^2 - v^2)^2 Z^2 (1 + Z^2)}{\gamma^2}, \quad (4.27)$$

$$C(\varepsilon) = \frac{u^2 (u^2 - v^2) (1 + Z^2)}{\gamma^2}, \quad (4.28)$$

$$D(\varepsilon) = \frac{v^2 (u^2 - v^2) Z^2}{\gamma^2}, \quad (4.29)$$

where  $\gamma^2 = (u^2 + Z^2(u^2 - v^2))^2$ . The energy-dependent transmission and reflection coefficients are shown in Figure 4.7.

The current is conserved in the junction, thus it is simple to calculate the current in the N side, where all current is carried by the single particles. The total current flow through the junction reads

$$I_{NS} = 2N(0)e v_F S \int_{-\infty}^{\infty} (f(\varepsilon - eV) - f(\varepsilon))(1 + A(\varepsilon) - B(\varepsilon)) d\varepsilon, \quad (4.30)$$

where  $S$  is the cross section area,  $N(0)$  is the one-spin density of states at Fermi energy, and  $f(\varepsilon) = (e^{(\varepsilon - \mu)/kT} + 1)^{-1}$  is the Fermi-Dirac distribution. From Equation (4.30), the  $I - V$  curves for an arbitrary barrier strength are obtained, as shown in Figure 4.8. With an increase of the barrier strength  $Z$ , the  $I - V$  characteristic changes continuously from metallic to tunneling limit.

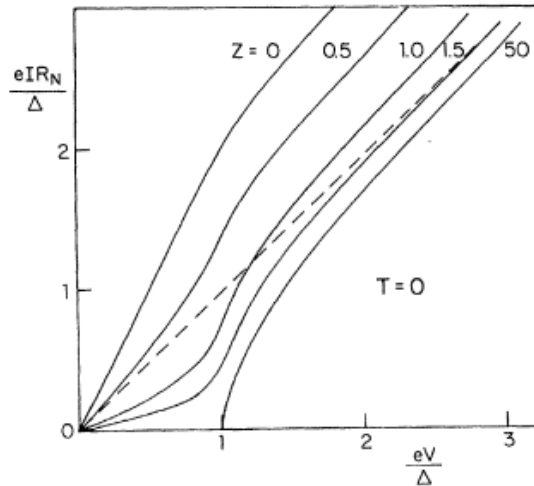


**Figure 4.8:** Current versus voltage for various barrier strength  $Z$  at zero temperature. Figure from Ref. [61].

In the normal state, where both sides of the interface are normal metals, the probability of the Andreev reflection is  $A = 0$ , and the probability of transmitted electrons is

$C = 1 - B = (1 + Z^2)^{-1}$ . The current of the normal state is obtained from Equation (4.30) as

$$I_{NN} = \frac{2N(0)e^2v_F S}{1 + Z^2} V = \frac{V}{R_N}. \quad (4.31)$$

At high voltages ( $eV \gg \Delta$ ),  $I_{NS}$  is linearly dependent on  $V$  with a slope of  $R_N$ . However, there is a constant displacement  $I_{NS} - I_{NN}$ , which is denoted as an excess current  $I_{exc}$ . On the  $I - V$  curve, the excess current is found by extrapolating back to the  $V = 0$  axis. The excess current is given by

$$\begin{aligned} I_{exc} &= (I_{NS} - I_{NN}) && (eV \gg \Delta) \\ &= \frac{1}{eR_N(1 - B(\infty))} \int_0^\infty (A(\varepsilon) - B(\varepsilon) + B(\infty)) d\varepsilon, \end{aligned} \quad (4.32)$$

where  $B(\infty) = Z^2/(1 + Z^2)$  is the reflection probability of electrons in the normal state. Equation (4.32) implies that the excess current is due to superconductivity. In Figure 4.8, the dashed line illustrates the dependence of  $I_{NN}$  on  $V$ . The excess current is larger for a relatively transparent N/S interface. For  $Z = 0$  and  $\Delta \ll kT$ , we have

$$I_{exc} = \frac{4\Delta}{3eR_N} \tanh \frac{eV}{2kT}. \quad (4.33)$$

#### 4.1.6 Multiple Andreev reflection

In a SNS junction, multiple Andreev reflection (MAR) is possible. Figure 4.9 schematically shows the multiple Andreev reflection process. When an electron is injected from the left superconductor  $S_L$  into the normal metal with an energy of  $\varepsilon$ , it gains an energy of  $eV$  when it arrives at the N/ $S_R$  interface because of the difference of the chemical potential  $\mu_L - \mu_R = eV$ . A hole is then reflected back and passes through the normal metal. In this process, the hole also obtains an energy of  $eV$ , since it has the opposite charge with respect to the electron. At the  $S_L/N$  interface, the hole is reflected as an electron owing to the time-reversal symmetry of the Andreev reflection. By repeating this process, the charge carrier gains an energy of  $neV$ , where  $n$  is the number of reflections. Once the energy of the charge carrier is larger than  $2\Delta$ , the charge carrier enters the quasiparticle continuum.

With an increase of the bias voltage, the particle reaches an energy of  $2\Delta$  with fewer reflections. The multiple Andreev reflection process induces an excess current similar to the Andreev reflection, which is described by Klapwijk et al. [62] with the BTK theory. For  $\Delta \ll kT$  and  $\Delta \ll eV$  with transparent interfaces, the excess current is given by

$$I_{exc} = \frac{8\Delta}{3eR_N} \tanh \frac{eV}{2kT}, \quad (4.34)$$

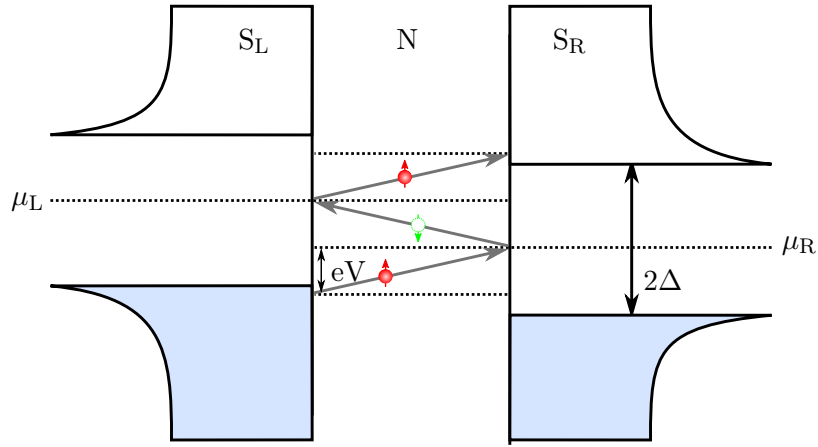


**Figure 4.9:** The process of multiple Andreev reflection in a SNS junction. The difference of the chemical potentials between the left and the right superconductor is  $eV$ . The quasiparticles pass through the SNS junction after accomplishing  $n = 2\Delta/eV$  Andreev reflections.

which is twice of the value calculated for the Andreev reflection in a NS junction [61]. The multiple Andreev reflection gives rise to the non-linearity of  $I - V$  characteristics, which is clearly visible in the differential conductance  $dI/dV$  (or differential resistance  $dV/dI$ ) versus bias voltage  $V$  curves. A series of peaks at voltages of  $2\Delta/ne$ , called subharmonic gap structure, are observed, as shown in Figure 4.10.

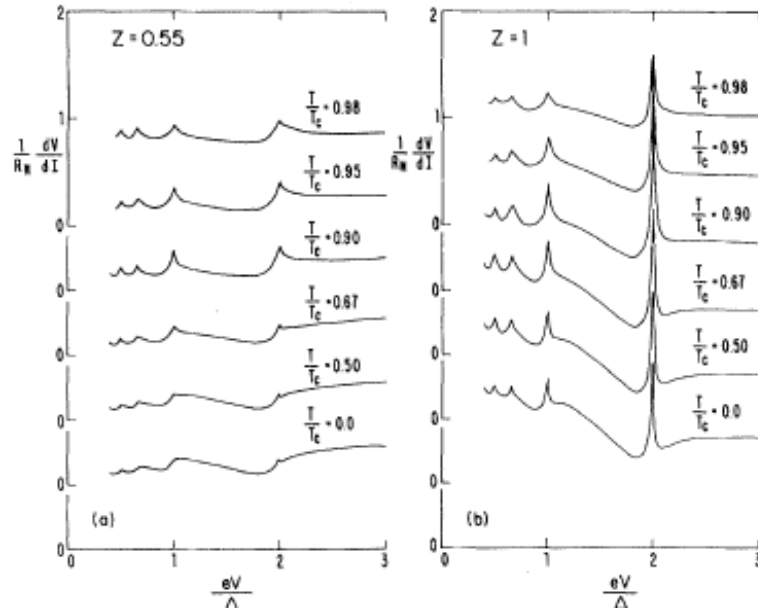


**Figure 4.10:** The differential resistance versus  $eV/\Delta$  simulated for various temperatures. Figure from Ref. [63].

### 4.1.7 Andreev reflection in magnetic field

In the presence of a magnetic field, the Andreev reflection is modified because of the cyclotron motion of the electrons or holes. In a low magnetic field, where the cyclotron radius is much greater than the channel length, i.e.  $r_c \gg L$ , the supercurrent is mediated by Andreev bound states as long as the phase shift between the electron and the reflected hole is small,  $\delta\theta < L/r_c \cos\theta$ , which is equivalent to a critical field  $B^* \sim \frac{\Delta}{eLv_f}$  [64]. This process is depicted in Figure 4.11b. The Andreev reflection for  $B < B^*$  are similar to the zero-field situation, in which a small phase shift  $\delta\theta < \Delta \tan\theta/\varepsilon_F$  is allowed by the Andreev reflection, as described in Figure 4.11a. For  $B < B^*$ , the interference between Andreev states from different paths causes a periodic suppression of the supercurrent when the flux  $\Phi$  is a multiple of a flux quantum  $\Phi_0$ . The maximum supercurrent exhibits a Fraunhofer pattern as the flux changes, which is described by the Josephson effect in Section 4.1.3.

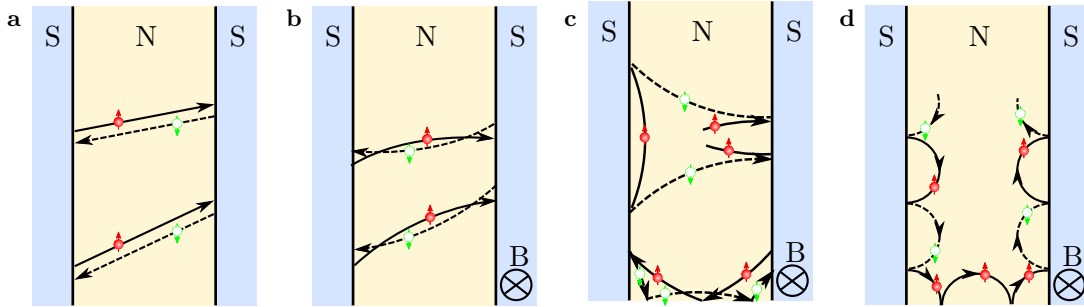


**Figure 4.11:** Andreev reflection in zero magnetic field  $B = 0$  (a), low magnetic field  $B < B^*$  (b), intermediate magnetic field  $B < B^*$  (c), high magnetic field  $B \gg B^*$  (d). Figures adapted from Ref. [64].

In a sufficiently high magnetic field ( $B \gg B^*$ ), the quantum Hall effect occurs and the cyclotron orbits are small ( $r_c < L/2$ ) so that the motion of the reflected hole bends in the same direction as that of the incident electron along the N/S interface, as shown in Figure 4.11d. In the clean limit, the electron-hole pairs can retain phase-coherence after several Andreev reflections. The conversion of electron and hole along the N/S interface forms the Andreev edge states, which destroy the backscattering of the standard Andreev reflection, resulting in the suppression of the supercurrent [65]. The conductance in a SNS junction is strongly affected by the Andreev edge states. A conductance step of  $2e^2/h$  is predicted for a transparent N/S interface [66, 67]. For a finite-scattering interface, the conductance exhibits an oscillatory behavior. The Andreev edge states can be detected by using a superconductor with a high critical field  $H_c$ , e.g. Niobium [64, 68].

In the intermediate field  $B > B^*$ , the trajectories of the electron-hole pair cannot develop closed loops, as sketched in Figure 4.11c. The electron returns to the incident interface after a few Andreev reflections, therefore the supercurrent is not able to pass the bulk

metal. There is an exceptional case that the supercurrent can pass through the junction when the Andreev reflections at the edge of the normal region transfer Cooper pairs.

#### 4.1.8 Proximity-induced superconductivity in graphene

Proximity-induced superconductivity in graphene — in our case induced by superconducting Al leads — draws special attention because the electrons in graphene are interpreted as massless relativistic particles described by the Dirac equation. The process of the Andreev reflection explains the proximity effect in an SNS (or NS) junction and is quantum mechanically described by the Bogoliubov-de Gennes equation. The two unrelated fields, the relativistic physics and the physics of many-body ground states, are linked together in a superconductor-graphene-superconductor (SGS) junction, which are expressed in the Dirac-Bogoliubov-de Gennes (DBdG) equation [69],

$$\begin{pmatrix} H - E_F & \Delta \\ \Delta^* & E_F - \mathcal{T}H\mathcal{T}^{-1} \end{pmatrix} \begin{pmatrix} \Psi_e \\ \Psi_h \end{pmatrix} = \varepsilon \begin{pmatrix} \Psi_e \\ \Psi_h \end{pmatrix}. \quad (4.35)$$

$H$  is the single-particle Hamiltonian in graphene that is

$$H = \begin{pmatrix} H_+ & 0 \\ 0 & H_- \end{pmatrix} \quad (4.36)$$

with  $H_{\pm} = -i\hbar v(\sigma_x \partial_x \pm \sigma_y \partial_y) + U$ .  $U$  is the electrostatic potential and  $\mathcal{T}$  is the time-reversal operator, which interchanges the valleys. The Hamiltonian is time-reversal invariant for zero magnetic field,  $\mathcal{T}H\mathcal{T}^{-1} = H$ . The pair potential  $\Delta(x)$  is zero in the normal metal but bears the form of  $\Delta_0 e^{i\varphi}$  in the superconductor. For a uniform system, an eigenstate of the DBdG equation is chosen as a plane wave  $(u, v) \exp(ik_x x + ik_y y)$ . The dispersion relation for an impurity-free graphene-superconductor junction is

$$\varepsilon = \sqrt{|\Delta|^2 + (E_F - U \pm \hbar v(k_x^2 + k_y^2)^{1/2})^2}, \quad (4.37)$$

in which the two branches of the excitation spectrum correspond to the conduction band and the valence band. The projection of the momentum parallel or normal to the interface are  $k_y$  and  $k_x$ , respectively.

The Andreev reflection is special in graphene as the two valleys are needed for a single Andreev reflection process [69]. Because of the time-reversal symmetry  $(\Psi_{A-}^*, -\Psi_{B-}^*) = \mathcal{T}(\Psi_{A+}, \Psi_{B+})$  (A, B denote the two sublattices, and  $\pm$  label the two valleys of the band structure), an electron in one valley is reflected as a hole in the other valley. In Figure 4.12a, a schematic of the Andreev reflection in graphene is depicted. The incident

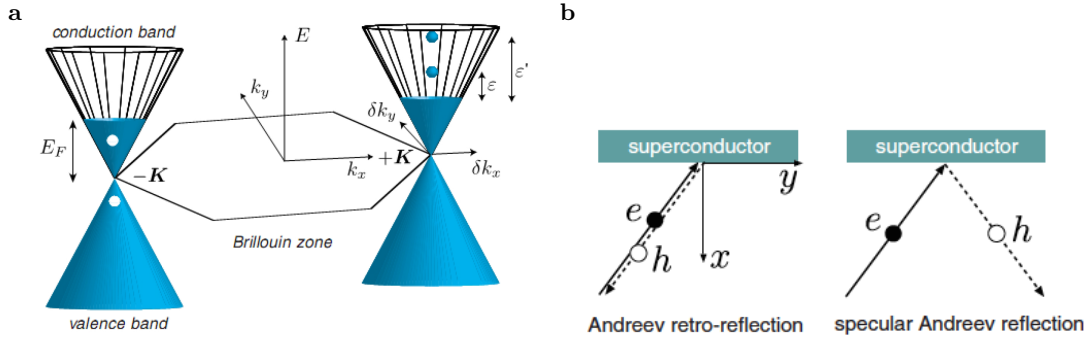


**Figure 4.12:** Andreev reflection in graphene. (a) The intraband reflection and interband reflection for the excitation energy  $\varepsilon < E_F$  and  $\varepsilon > E_F$ , respectively. (b) The intraband reflection is the Andreev retro-reflection, and the interband reflection is the specular Andreev reflection. Figure from Ref. [70].

electrons are in the conduction band (filled state) from one valley. Given the fact that the Fermi level of graphene can be continuously tuned by applying a gate voltage, two different Andreev reflection processes may occur. For  $\varepsilon < E_F$ , the reflected hole is in the conduction band since the energy has to be conserved during the Andreev reflection. This intraband reflection is similar to the situation of the traditional NS junctions. For  $\varepsilon > E_F$ , however, the reflected hole is an empty state in the valence band. The Andreev reflection is an interband process, which most likely takes place in the vicinity of the Dirac point.

In the Andreev reflection process, the momentum  $k_y$  and the excitation energy  $\varepsilon$  are conserved at the interface. Thus, Equation (4.37) is solved at given  $k_y$  and  $\varepsilon$ . In the graphene side,  $U = \Delta = 0$ , the  $x$  component of the velocity is defined by the derivative  $v_x = \hbar^{-1} d\varepsilon/dk_x$ , which is positive for the reflected states. There are two possible  $k_x$  values corresponding to the positive slope  $v_x$  in the dispersion relation. One is for the reflected electron state (normal reflection) and the other is for the reflected hole state (Andreev reflection). Since a hole in the conduction band moves in a direction opposite to its wave vector, both  $v_x$  and  $v_y$  change sign if  $\varepsilon < E_F$ . Therefore, the intraband Andreev reflection is a retro-reflection. If  $\varepsilon > E_F$ , a hole in the valence band moves in the direction of its wave vector. The reflection changes the sign only of  $v_x$ , while  $v_y$  remains unchanged. This Andreev reflection is specular which is related to interband reflections, as shown in Figure 4.12b.

By applying the Dirac-Bogoliubov-de Gennes equation, Titov and Beenakker [71] predict the existence of a supercurrent at the Dirac point and give a formula for the critical supercurrent in the ballistic limit at zero temperature

$$I_c = 1.22 \frac{e\Delta_0}{\hbar} \frac{\mu W}{\pi \hbar v}. \quad (4.38)$$

At finite temperatures, the supercurrent in SGS junction has been independently simulated by Hagymási et al. [72] and Sarvestani et al. [73].

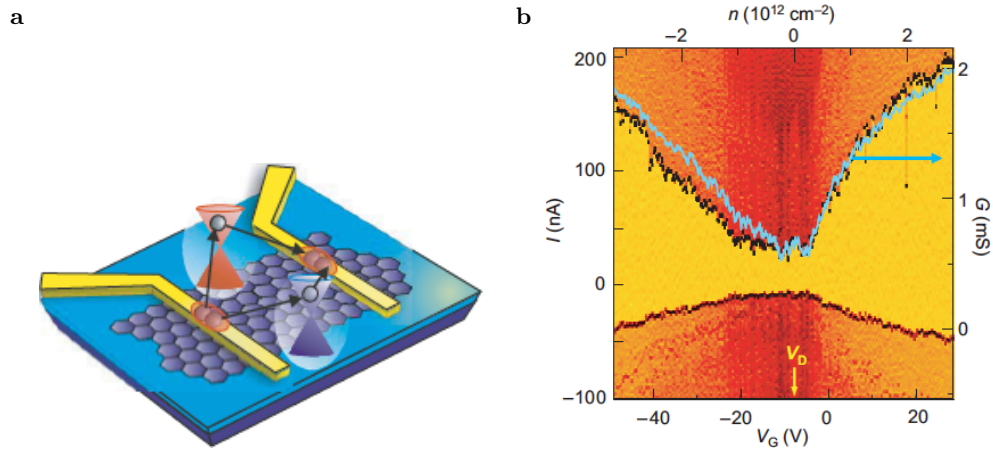


**Figure 4.13:** Bipolar supercurrent. (a) A schematic of a SGS junction. The two electrons in a Cooper pair pass graphene through two different K-valleys, denoted by the red and blue cones. (b) An example of the bipolar supercurrent. The supercurrent is carried by electrons or holes in graphene. Figures from Ref. [74].

The proximity-induced superconductivity in graphene has firstly been experimentally investigated by Heersche et al. [74]. The supercurrent was measured in a Ti/Al-graphene-Ti/Al Josephson junction. The authors found that the supercurrent can be carried by either electrons in the conduction band or holes in the valence band. By changing the charge carrier density with a back-gate, the supercurrent is tunable and reaches a value of 140 nA at high density. Furthermore, the supercurrent still exists at the Dirac point, where the charge carrier density is zero. Choi et al. [75] claim that the supercurrent can be switched off by creating a p-n potential barrier in graphene. The multiple Andreev reflection is also expected in the SGS junction. The corresponding subharmonic gap structure up to  $n = 6$  in diffusive graphene has been observed by Du et al. [76], which indicates the highly transparent SG interfaces. Apart from using Al as electrodes, high temperature superconductors, i.e. Ta ( $T_c = 2.5$  K) [77], Pb ( $T_c = 2$  K) [78], PbIn ( $T_c = 4.8$  K) [79], TiNb ( $T_c = 8.5$  K) [80], have been used as electrodes to investigate the superconductivity in SGS junction. The critical field  $H_c$  is much higher in the high- $T_c$  superconductor, which allows to examine the quantum Hall effect of graphene in the superconducting state [80]. In the presence of Andreev edge states, the quantum Hall plateau conductance has been enhanced compared to the normal state. The previous results mentioned above are mainly limited to the diffusive regime, preventing to probe the intrinsic properties of graphene. Although in ballistic graphene, the supercurrent has been studied theoretically for a long time, it has been observed in recent experiments only [64, 68] benefiting from the great improvement of the sample quality.

So far, most investigations on the proximity effect of graphene Josephson junctions focus on monolayer graphene and only a few works take bilayer graphene into consideration. Muñoz et al. [81] utilize the tight-binding Bogoliubov-de-Gennes model to simulate the Josephson current in a bilayer-graphene-based Josephson junction. The proximity effect for bilayer graphene is similar to that for monolayer graphene in many cases, especially for a undoped short junction [82]. However, a few differences have been predicted. For an undoped junction, the supercurrent is not homogeneously distributed within each layer although the average current is constant in the normal region [81]. Therefore, a weak interlayer current is expected. By applying a displacement field to bilayer graphene, the supercurrent can be switched off due to the gap opening if the length of the junction is larger than the Fermi wavelength. Takane et al. [82] derive an analytic solution for the supercurrent in bilayer graphene SGS junction, which has a simple form at the zero temperature

$$I_c = e \frac{2\mu W}{\pi\gamma_0} \sqrt{\frac{\gamma_1}{\mu}} \frac{\frac{\Gamma}{2}\Delta_0}{\Delta_0 + \frac{\Gamma}{2}}, \quad (4.39)$$

where  $\mu$  is the chemical potential,  $\gamma_0$  is the nearest-neighbor in-plane transfer integral,  $\gamma_1$  is the nearest-neighbor vertical coupling, and  $\Gamma$  is the strength of the tunnel coupling.

In sharp contrast to monolayer graphene, bilayer graphene is peculiar because of the possibility to open a band gap and the anti-Klein tunneling of charge carriers in the presence of a potential barrier. In the following, we present the measurement results on proximity-induced superconductivity in a bilayer graphene Josephson junction with a potential barrier.

## 4.2 Normal state resistance

In this section, we characterize the normal-state resistances for two devices at low temperature of 4.2 K where conductance maps were already shown in Figure 3.9a and Figure 3.11a. The transport properties have been discussed in Chapter 3. Here, Figure 4.14 presents the resistance measurement of two devices as a function of the top-gate voltage  $V_{tg}$  and the back-gate voltage  $V_{bg}$ . The two devices are both fabricated from the hBN-BLG-hBN heterostructure. The ratios of  $W/L$  for both devices are set to be 5, but the lengths of the devices  $L$  are 1  $\mu\text{m}$  and 0.8  $\mu\text{m}$  for the sample BL12C and BL12D, respectively. The two resistance maps are measured separately for two different cool-downs. Because of the thermal cycling between the two measurements, the intrinsic doping has been slightly changed for the sample BL12D at the second cool-down, thus we observe a small shift of the charge neutrality point on the resistance map, as observed in Figure 4.14b.

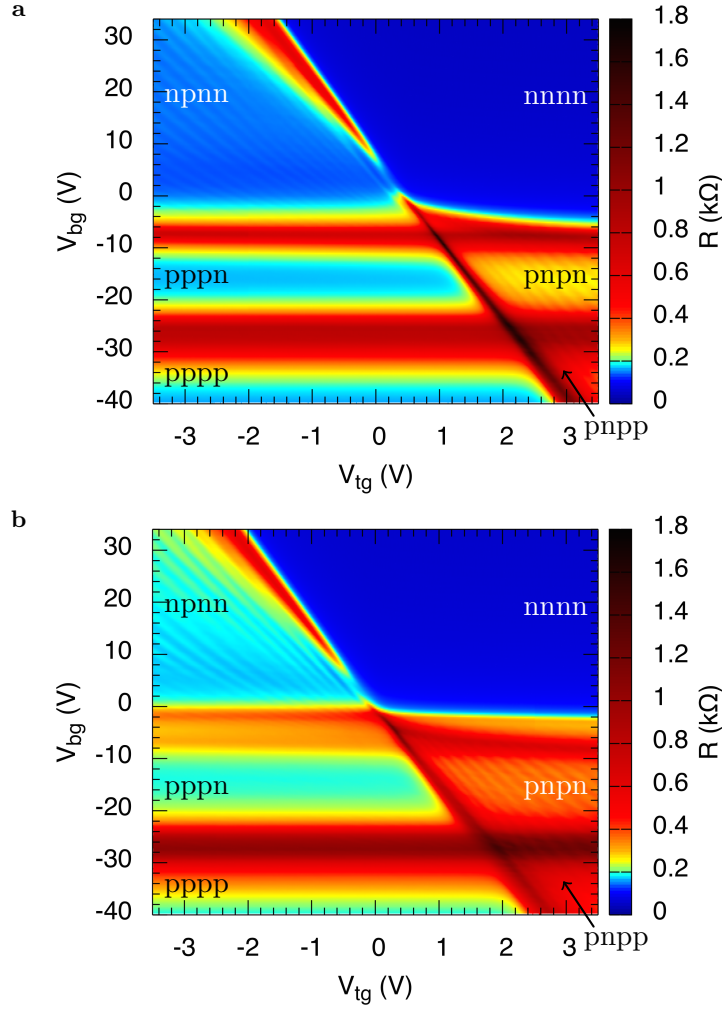


**Figure 4.14:** Resistance as a function of  $V_{tg}$  and  $V_{bg}$  at the normal state for the sample BL12C (a) and BL12D (b), respectively. The two samples are both measured at a temperature of 4.2 K but for two different cool-downs.

A comparison of the resistance for the two devices at the same density shows that the resistance of the sample BL12C is higher than of BL12D in the npnn, pnpp, pppn, pppp and pppn regions while it reaches similar values in the nnnn region. Since the two samples have the same  $W/L$  ratio, the resistances in the nnnn region are  $42 \Omega$  and  $48 \Omega$  at a charge carrier density of  $-2.55 \times 10^{12} \text{ cm}^{-2}$  for sample BL12C and BL12D, respectively. The reason is as follows: the transmission for the two devices is similar in the absence of the p-n interfaces in the nnnn region. However, it is much lower for the shorter device in the npnn, pnpp, pppn, pppp and pppn regions where p-n interfaces exist. The p-n interfaces for the pppp region come from the edges of graphene which are n-doped by the source/drain contacts.

In the following, we use the resistance map shown in Figure 4.14a as the normal state resistance for the sample BL12C, since the normal state and superconducting state (25 mK) are measured during the same cool-down. For the sample BL12D, the normal state

resistance is extracted from the linear part of the  $I - V$  curves which are measured independently at a temperature of 15 mK.

### 4.3 Ballistic Josephson current in S-BLG-S junctions

In this section, we investigate the Josephson effect of two junctions with a length  $L$  of 1  $\mu\text{m}$  and 0.8  $\mu\text{m}$ , respectively. All leads are used as superconductors. For bulk aluminum, the energy gap is  $2\Delta \sim 340$   $\mu\text{eV}$  at  $T = 0$  K and the transition temperature  $T_c$  is  $\sim 1.18$  K [83]. For the junction of  $L = 1$   $\mu\text{m}$ , we estimate the mean free path  $l_m$  from the normal state conductivity as

$$l_m = \frac{\pi}{2} v_F \frac{\sigma m_0}{ne^2} \sim 8.78 \text{ } \mu\text{m}. \quad (4.40)$$

Here,  $v_F \approx \hbar k_F / 0.035 m_0$  is the Fermi velocity of bilayer graphene,  $m_0$  is the rest mass of electrons,  $n$  is the charge carrier density,  $\sigma$  is the conductivity. In the clean limit, the phase coherence length  $\xi = \frac{\hbar v_F}{2\pi k_B T}$  is approximately 51  $\mu\text{m}$ , where  $v_F$  is the Fermi velocity of bilayer graphene. Thus, the length of the junction is much smaller than the mean free path and the phase coherence length,  $L < l_m < \xi$ . The similar relation holds for the shorter junction as well. Hence, the transport properties in the junctions are within the ballistic short-junction regime.

As illustrated in Figure 4.15, we observe the Josephson current in a ballistic bilayer graphene p-n-p junction at a temperature of 25 mK. The supercurrent can be tuned by operating the top and bottom gates. The two quadrants in Figure 4.15a for  $V_{bg} > -7.5$  V correspond to the nnnn and npnn regions. As shown in Figure 4.15b, the  $I - V$  characteristics shows a sharp jump from the normal current to the Josephson current in the nnnn regime. The supercurrent increases monotonically with the back-gate voltage at a constant top-gate voltage  $V_{tg} = 2$  V, and a maximum  $I_c$  of 1.72  $\mu\text{A}$  has been reached for a channel length of 1  $\mu\text{m}$  in the first cool-down. We note that  $I_c$  slightly changed after thermal cycles to room temperatures. On the contrary, in the npnn regime for  $V_{tg} = -2$  V, the maximum of  $I_c$  appears at a back-gate voltage of 5 V, as pictured in Figure 4.15d. As long as the electron density in the n region or the hole density in the p region is low, the value of  $I_c$  is small. The maximum value in the npnn side is reached only when the hole or electron densities are both large.

We further observe that  $I_c$  in the npnn region is one order of magnitude smaller than in the nnnn region. The reason is that in the presence of p-n interfaces, the transmission probabilities of charge carriers in the npnn region are dramatically reduced. Moreover, it is found that  $I_c$  in both nnnn and npnn regimes can also be tuned by the top-gate

voltage, as shown in Figure 4.15c. The supercurrent increases with the top-gate voltage, which is due to the increase of the charge carrier density in the local gated region. When the charge carrier density in the local gated region is larger than the parts outside the potential,  $I_c$  becomes saturated.

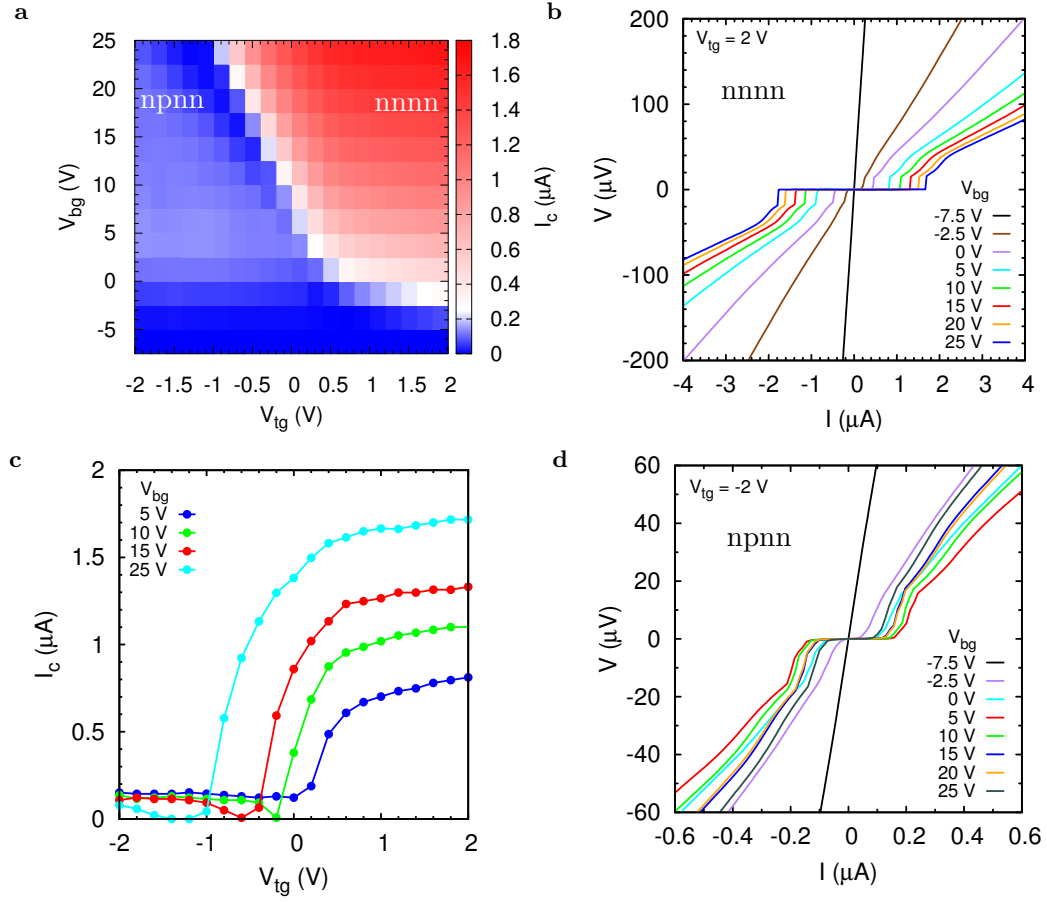


**Figure 4.15:** Supercurrent tuned by dual-gates for the sample BL12C. (a) The supercurrent  $I_c$  as a function of  $V_{tg}$  and  $V_{bg}$  at 25 mK. The  $I_c$  is extracted from the  $I - V$  curves which is measured by varying  $V_{tg}$  and  $V_{bg}$  with steps of 0.2 V and 2.5 V, respectively. (b) The dependence of  $I_c$  on  $V_{bg}$  in the nnnn region with a fix of  $V_{tg}$  at 2 V. (c)  $V_{tg}$  dependence of  $I_c$  for  $V_{bg} = 5, 10, 15, 25$  V. (d)  $V_{bg}$  dependence of  $I_c$  in the npnn region for  $V_{tg} = -2$  V.

Figure 4.16 shows an  $I - V$  curve measured on the device BL12D at  $V_{bg} = 40$  V and  $V_{tg} = 3.5$  V for a constant current bias. As expected for an underdamped Josephson junction, a small hysteresis is observed. The transition from a zero-voltage state to a finite-voltage state always occurs for high currents. The difference between the critical current and the retrapping current is small even at high density. We employ the RCSJ model to fit the  $I - V$  curve with the following parameters:  $I_c = 1.55$   $\mu\text{A}$  and  $R = 33.7$   $\Omega$ . We obtain a junction capacitance of  $C = 2.35 \times 10^{-13}$  F, the corresponding plasma frequency of  $\omega_p = 1.42 \times 10^{11}$  Hz, and the Stewart-McCumber parameter of  $\beta_C = 1.26$ . Therefore, the junction is slightly underdamped. At the finite voltage, the critical current

obtained from the experiment is lower than the calculated value because the multiple Andreev reflection is not considered in the RCSJ model.

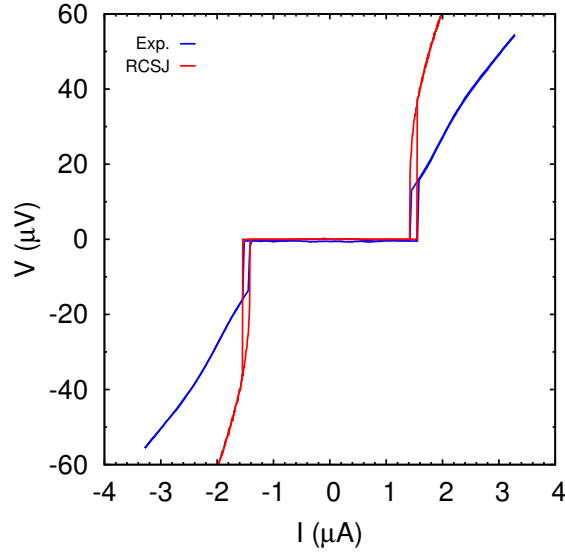


**Figure 4.16:** The voltage-current relation measured at  $V_{bg} = 40$  V and  $V_{tg} = 3.5$  V for the device BL12D at a temperature of 15 mK (blue), and the corresponding simulation using the RCSJ model (red). A small hysteresis illustrates that the junction is slightly underdamped.

#### 4.4 Multiple Andreev reflections

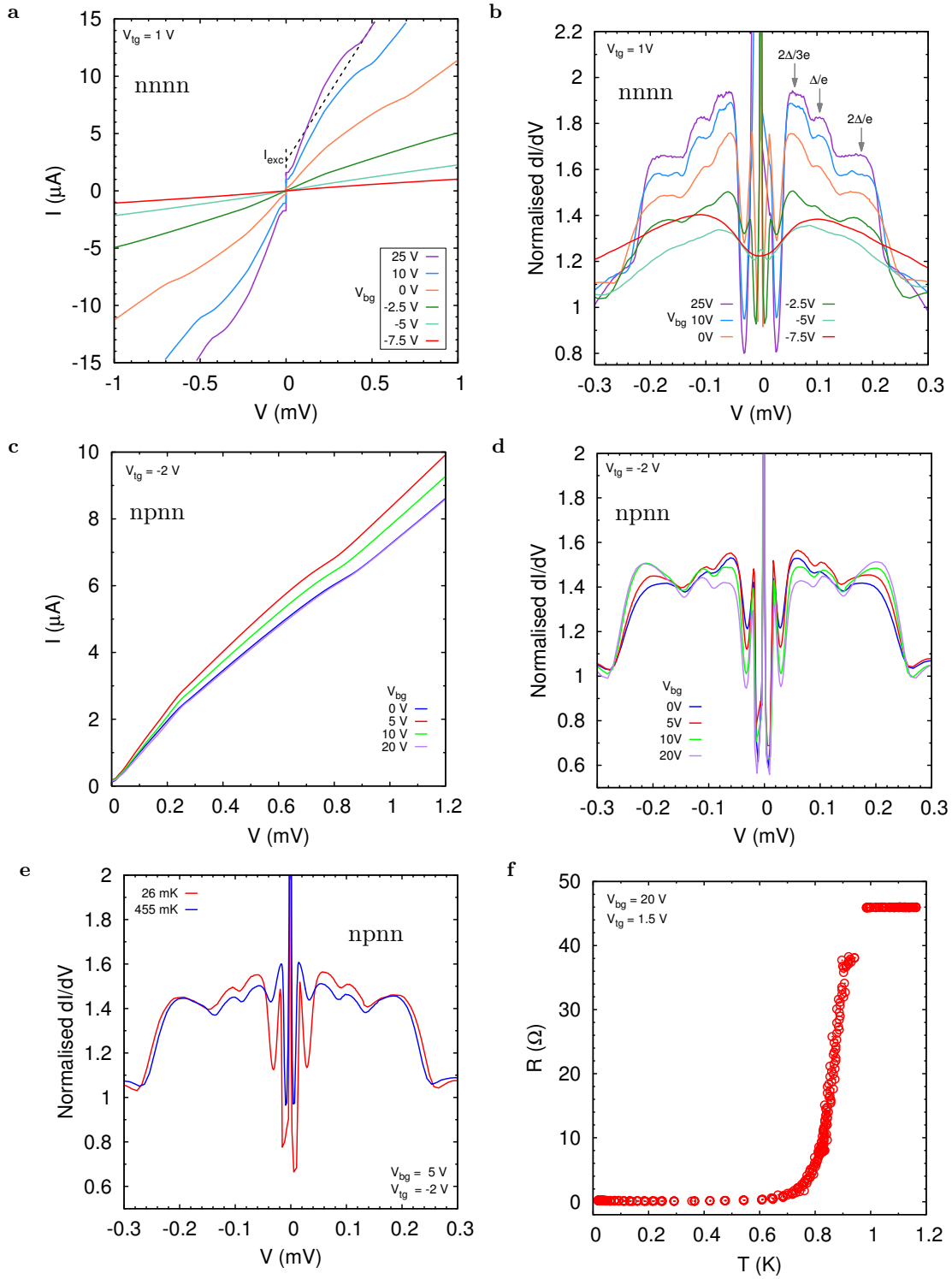
In a SNS junction where multiple Andreev reflection occurs, the subharmonic gap structure and excess current will be discussed in the following.

Figure 4.17a shows the  $I - V$  characteristics at  $V_{tg} = 1$  V in the nnnn region. The  $I - V$  curves switch from a linear behavior to a non-linear style as the back-gate voltage  $V_{bg}$  increases. For  $V_{bg} > -2.5$  V, the current remains linear in the high-voltage limit, but does not extrapolate back to zero at zero voltage, as sketched in Figure 4.17a. The interception on the  $V = 0$  axis is referred to as the excess current  $I_{exc}$ . Since the current is conserved along the junction, we can calculate the current in the normal region, which has three contributions: incident electrons to the N/S interface, electrons resulting from Andreev reflection of holes, and electrons injected into the normal metal from incident quasiparticles in the superconductor. The excess current originates from the multiple Andreev reflection process in the SNS junction. When an incident electron reaches to the N/S interface and is reflected as a hole, a current flows through the junction. The excess current is approximately  $2.59 \mu\text{A}$  at  $V_{bg} = 25$  V, which is larger than  $I_c = 1.67 \mu\text{A}$ .

Features induced by MAR are more visible in differential conductance  $dI/dV$  (see Figure 4.17a and Figure 4.17d) than in  $I - V$  curves (see Figure 4.17a and Figure 4.17c). Figure 4.17b displays the differential conductance  $dI/dV$  as a function of the voltage  $V$  for different back-gate voltages  $V_{bg}$ . In the nnnn region, a series of maxima in  $dI/dV$  is observed. This is due to the multiple Andreev reflection at the N/S interfaces. Theoretically, the subharmonic gap structure are expected to locate at voltages of  $V = 2\Delta/ne$ . However, heating effects may distort the shape as well as shift the position of MAR features [84]. As shown in Figure 4.17e, the positions of peaks shift slightly towards lower voltage when the temperature increases to 455 mK. At the same time, the amplitudes of the peaks increase. Therefore, the subharmonic gap structures are more visible as the temperature is close to  $T_c$ , which is also true for a high barrier strength [63].

In a ballistic junction, the amplitudes of MAR features can be tuned by the applied gate voltages [85]. A comparison between Figure 4.17d and Figure 4.17b shows that the peaks are more pronounced in the npnn region than in the nnnn region. This is because, in the npnn region, the transmission probabilities of charge carriers are much lower in the presence of p-n interfaces [63, 85]. By comparing the  $dI/dV$  curves at different back-gate voltages within the npnn region, we see that the amplitudes of the peaks at  $2\Delta/e$  and  $\Delta/e$  increase when the charge carrier density becomes lower. In addition, the amplitudes of the peaks decrease if the number of reflections increases [62].

From the  $dI/dV$  versus  $V$  curves, we extract the superconducting gap of the electrodes  $2\Delta$  according to the positions of subharmonic gap structure induced by MAR. The obtained superconducting gap of the electrodes is  $2\Delta \approx 210 \mu\text{eV}$  for both nnnn and npnn regions, which is in good agreement with the data reported in Ref. [75]. Given  $\Delta = 1.76k_B T_c$  in the BCS theory, a critical temperature  $T_c$  of 692 mK is expected. The experimentally measured  $T_c$ , at which the transition from the superconducting to normal state occurs, is in the range of 692 to 934 mK, as shown in Figure 4.17f. Thus the experimentally obtained value  $\Delta \approx 105 \mu\text{eV}$  is consistent with the BCS theory.



**Figure 4.17:** Excess current and subharmonic gap structure (sample BL12C).  $I - V$  characteristics in the nnnn region at  $V_{tg} = 1\text{ V}$  (a) and in the npnn region at  $V_{tg} = -2\text{ V}$  (c). The black dotted line in (a) indicates the excess current  $I_{exc}$  for  $I - V$  curve taken at  $V_{bg} = 25\text{ V}$ . Differential conductance  $dI/dV$  versus bias voltage  $V$  curves changes with the  $V_{bg}$  in the nnnn (b) and npnn (d) regions. The  $dI/dV$  value is normalized by the normal state resistance  $R_n$  of each  $V_{bg}$ .  $\Delta = 105\text{ }\mu\text{m}$ . (e) Temperature dependence of  $dI/dV$  versus  $V$  curve measured at  $V_{bg} = 5\text{ V}$  and  $V_{tg} = -2\text{ V}$  in the npnn region. (f) Resistances as a function of the temperature.

## 4.5 $I_c R_n$ product

The supercurrent in a Josephson junction is correlated to the normal-state resistance. The  $I_c R_n$  product is usually used to characterize the quality of Josephson junctions. Figure 4.18 shows the  $I_c R_n$  product that is normalized by  $\Delta/e$ . The  $I_c R_n$  product depends on both back-gate and top-gate voltages. Figure 4.18a shows that  $eI_c R_n/\Delta$  increases with the back-gate voltage for both nnnn and npnn regions, which are described by the red-filled and blue-empty diamonds, respectively. In the unipolar regime,  $eI_c R_n/\Delta$  ( $\Delta = 105 \mu\text{eV}$ ) increases monotonically and reaches a maximum of 0.72 at  $V_{bg} = 25 \text{ V}$ . In the bipolar regime  $eI_c R_n/\Delta$  saturates after reaching its maximum of 0.19 at 5 V. The oscillations above 5 V can be attributed to Fabry-Pérot interferences (see Section 4.7). Figure 4.18b presents the dependence of  $eI_c R_n/\Delta$  on  $V_{tg}$  for a constant back-gate voltage  $V_{bg} = 5 \text{ V}$ . The value of  $eI_c R_n/\Delta$  in the npnn region is less than 50% of that in the nnnn region, which indicates that the diffusion of the Andreev bound state is partially suppressed by the presence of the p-n interfaces. When tuning the Fermi energy away from the Dirac point in the middle of the device, a saturation of  $eI_c R_n/\Delta$  is observed in the npnn region.

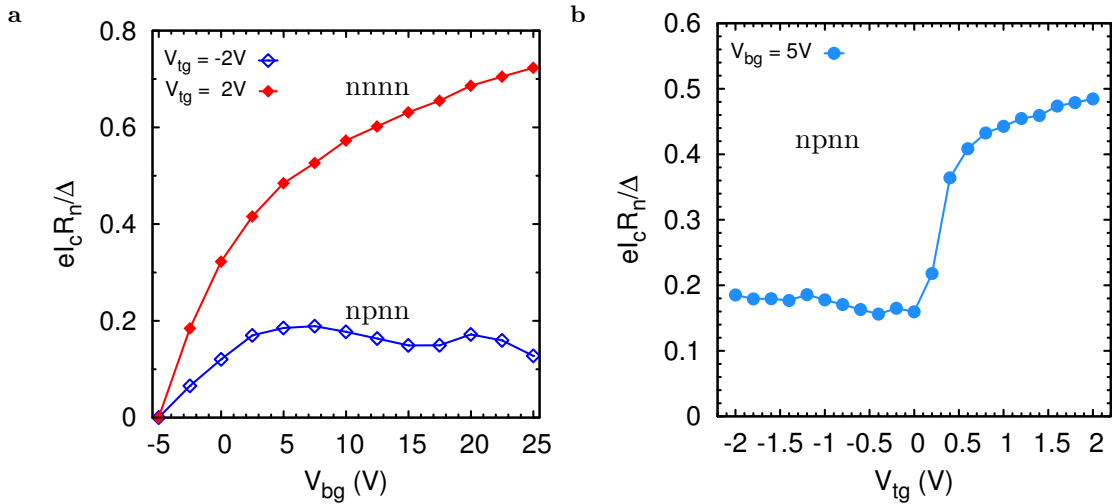


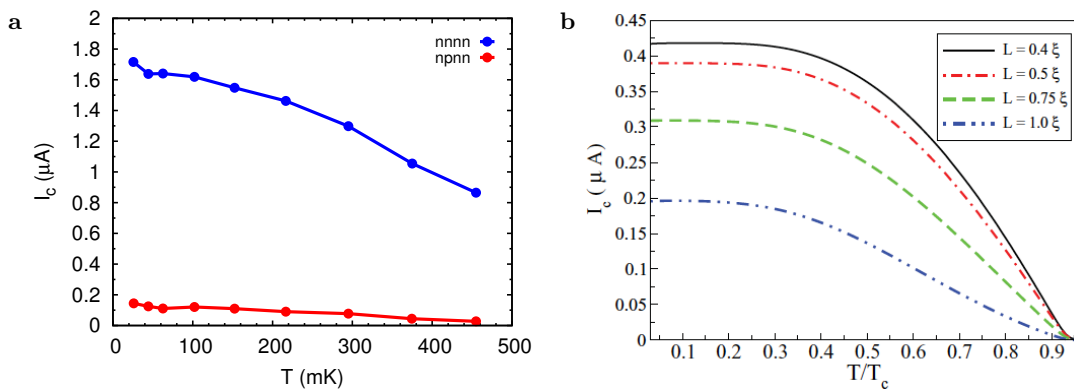
**Figure 4.18:** The normalized  $I_c R_n$  product  $eI_c R_n/\Delta$  for sample BL12C tuned by the back-gate voltage  $V_{bg}$  (a) and the top-gate voltage  $V_{tg}$  (b). In (a), the red-filled and blue-empty diamonds represent the data in the nnnn and npnn regimes, respectively.

The  $I_c R_n$  product is related to the length of the channel. Ben Shalom et al. [64] measured the supercurrent in devices with different lengths and showed that the relation between the  $eI_c R_n/\Delta$  and the channel length exhibits a  $1/L$  dependence in the ballistic regime. A maximum value of 0.43 is obtained for a device of 150 nm, while the value of  $eI_c R_n/\Delta$  is below 0.1 for a device longer than 1  $\mu\text{m}$ . In the present work, we obtain a maximum  $I_c R_n$  of 0.72 for a 1- $\mu\text{m}$  long device, which is by far the highest value reported so far. The

theoretical  $I_c R_n$  products are usually estimated for a fully transparent N/S interface. For example,  $I_c R_n = 2.44\Delta/e$  has been calculated for ballistic short junctions (sample length  $L \ll \xi$ ) [69]. If we take the  $1/L$  dependence into consideration, our result is close to the ballistic limit, which indicates that the N/S interfaces are highly transparent in the unipolar regime. In the npn region, the reduction of the  $I_c R_n$  product is due to the finite transmission probability of the p-n interfaces.

## 4.6 Temperature dependence of the supercurrent

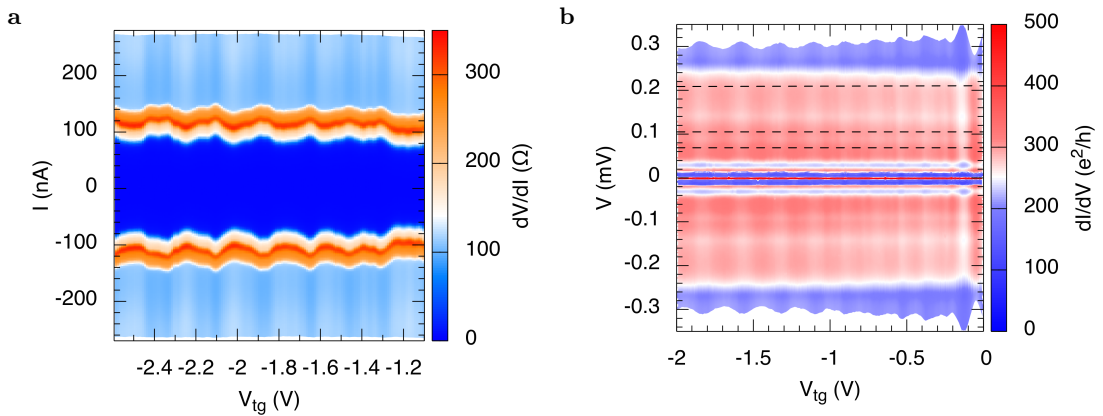
If the temperature increases, the supercurrent decreases. Figure 4.19a shows the temperature dependence of supercurrent. The blue and red dots denote the supercurrent in nnnn and npnn regions, respectively. The measurements have been performed up to  $T = 455$  mK because it is more complicated to run the cryostat above 500 mK.  $I_c$  in the npnn region decreases to 27 nA at  $T \approx 455$  mK, while it remains at  $\sim 0.8$   $\mu$ A in the nnnn region. Additionally, in the unipolar regime, the  $I_c$  changes slowly for  $T < 200$  mK. This is consistent with the theoretical predictions for SGS short junctions based on single-layer graphene [73], as shown in Figure 4.19b. The theoretical results also present a temperature dependence for various ratios of sample lengths  $L$  to the phase coherence length  $\xi$ . In our case, we have tried to fit our data with Eilenberger theory for ballistic junctions according to Galaktionov and Zaikin [86]. Although the model was developed for ballistic junctions and has explained some experiment results [87], the predicted  $I_c$  is one order of magnitude smaller than observed in the unipolar regime. A suitable model is required to explain this discrepancy.



**Figure 4.19:** Temperature dependence of the supercurrent (sample BL12C). (a) The supercurrent versus Temperature curves for nnnn and npnn regions, denoted in blue and red, respectively. (b) The theoretical simulations of  $I_c(T)$  curves for SGS junctions in the short junction limit. The simulations are carried for different  $L/\xi$  ratios. Figure from Ref. [73].

## 4.7 Critical current oscillations due to the Fabry-Pérot interference

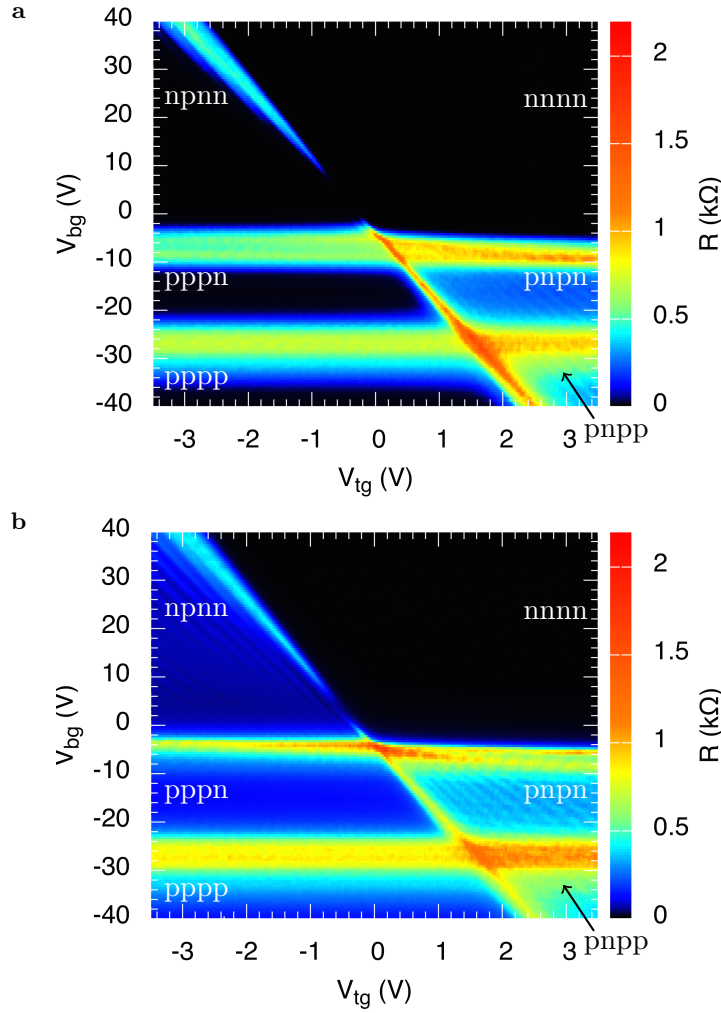
The critical current oscillates at a constant value of  $V_{bg}$  when tuning the top-gate voltage in the npn region, as shown in Figure 4.20a. The value of  $dV/dI$  is measured with respect to the top-gate voltage  $V_{tg}$  and the current  $I$  at a constant value of the back-gate voltage  $V_{bg} = 10$  V. The oscillations of  $I_c$  correspond to the resistance oscillations in the normal state due to the Fabry-Pérot interference. When the resistance passes through a minimum,  $I_c$  has a maximum. Figure 4.20b shows the evolution of  $dI/dV$  as a function of the top-gate voltage  $V_{tg}$  and the voltage  $V$  at  $V_{bg} = 5$  V. The amplitude of the subharmonic gap structures at voltages  $2\Delta/ne$ , follows the conductance oscillations in the normal state as well. However, the positions of these features do not fluctuate with quantum interference, indicating that  $\Delta$  does not oscillate. Thus, the oscillations of  $I_c$  are solely attributed to the transmission resonances of Fabry-Pérot interference.



**Figure 4.20:** Critical current oscillations originating from Fabry-Pérot interferences (sample BL12C). (a) The differential resistance as a function of the top-gate voltage  $V_{tg}$  and the current. The deep blue represents the Josephson current. (b) The differential conductance versus the top-gate voltage  $V_{tg}$  and the voltage. The subharmonic gap structures, marked with the white dashed lines, are located at voltages of  $2\Delta/ne$ .

## 4.8 Switching off the supercurrent

In this section, we describe three ways to switch off the supercurrent in a dual-gated graphene Josephson junction. Figure 4.21 shows that the resistance varies with  $V_{tg}$  and  $V_{bg}$  for two devices, i.e. BL12C and BL12D. The two samples are very similar. Both have a  $W/L$  ratio of 5 and a top-gate length of  $\approx 150$  nm. But there is one difference, which is the length of the channel, i.e.  $1 \mu\text{m}$  for sample BL12C and  $0.8 \mu\text{m}$  for sample BL12D. The resistance maps of these samples as a function of  $V_{tg}$  and  $V_{bg}$  are shown in



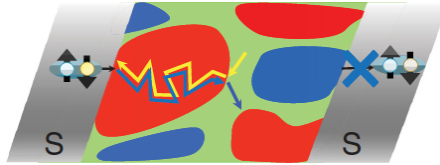
**Figure 4.21:** The color scaled plots of Resistances as a function of  $V_{tg}$  and  $V_{bg}$  for the sample BL12C (a) and the sample BL12D. The measurements have been done at superconducting state ( $T = 15$  mK).

Figure 4.21. The two devices are measured at a temperature of 15 mK and within the same cool-down. It is important to note that both were cooled down the same number of times, and that they have been fabricated from the same bilayer graphene flake. In Figure 4.21a, we observe that the sample BL12C is superconducting in the nnnn, npnn, pppn, pppp regimes, but resistive in the pnpn, pnpn regimes as well as at the charge neutrality lines while the sample BL12D only becomes superconducting in the nnnn regime as shown in Figure 4.21b. Hence we can control the on- and off-states of the supercurrent by manipulating the two gates. In both devices, the supercurrent can be switched off by tuning the gates to the horizontal charge neutrality lines, diagonal charge neutrality line (gap region), and pnpn or pnpn regions.

In the normal state, the resistances in the nnnn region are smaller than in the npnn and pppp regions, i.e.  $R^{nnnn} < R^{npnn}$  and  $R^{nnnn} < R^{pppp}$ . This is due to the angular transmission probabilities of p-n junctions in the npnn and pppp regions. Note that there

are two p-n junctions formed at the edges of the sample because the contacts induce n-doping at the edges. These p-n junctions at the edges are sharper than the ones created by the top gate in the npnn region, leading to lower transmission probabilities. In the superconducting state, the selective transmission of p-n junctions also affects the supercurrent for sample BL12C, yielding to  $I_c^{nnnn} > I_c^{nppn} > I_c^{pppp}$ .

**Switch off the supercurrent in the presence of a potential barrier.** The critical current in the nnnn region decreases with increasing the length of the channel, which is consistent with the BCS theory. The maximum critical current is 1.63  $\mu\text{A}$  for sample BL12D and 1.49  $\mu\text{A}$  for sample BL12C. The  $I_c R_n$  product is  $0.65\Delta/e$  in sample BL12D, which is larger than  $0.48\Delta/e$  in sample BL12C. Note that the  $I_c R_n$  products measured for sample BL12C in this cool-down are lower than the values displayed in Section 4.5 because the Al contacts have degraded after five months. On the contrary, in the npnn region, the supercurrent is off in sample BL12D, but on in sample BL12C. This is unexpected according to the BCS theory. The difference between the nnnn and npnn regions is that a potential barrier exists in the npnn region and affects the transmission. However, the selective transmission of p-n junctions (see Section 3.1.2) cannot account for the off state of the supercurrent in device BL12D because MAR, a consequence of phase-coherent propagation of electron and hole pairs, remains visible in the npnn region for both samples. This means that the electron and hole pairs can undergo phase-coherent transport at finite DC bias voltages even in the presence of p-n junctions. The difference may lie in the zero-voltage state (DC bias voltage  $V = 0$ ), where the electron and hole pairs break up in sample BL12D, but survive in sample BL12C. This problem needs better understanding and further discussions.



**Figure 4.22:** Sketch for the specular-like Andreev reflection near Dirac point. Figure from Ref. [88].

**Switch off the supercurrent at Dirac points.** The two horizontal lines at the resistance maxima indicate the Dirac points of graphene that we tuned only by the back-gate. The off-state of the supercurrent may arise from the specular-like reflection of the electron-hole pairs along the contour of the charge puddles, as claimed in Ref. [88] and illustrated in Figure 4.22. It is known that graphene conducts as a random network of electron and hole puddles around the charge neutrality point. The electron and hole puddles are separated by insulating regions. At the boundary of the puddles,

the electron-hole pairs break due to a specular-like reflection, which impedes superconductivity. Further experiments with better samples should clarify the possible role of inhomogeneities on the supercurrent at the Dirac point.

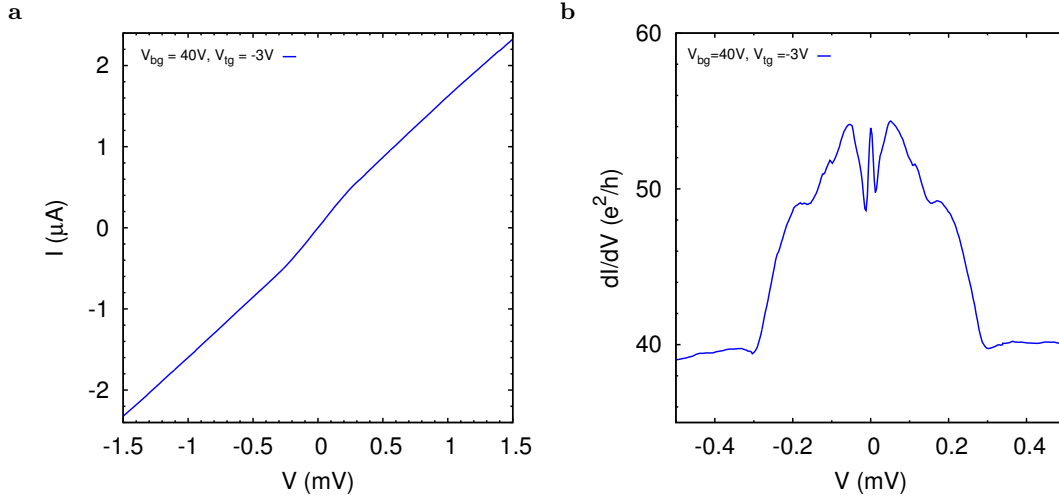


**Figure 4.23:** Suppression of the supercurrent in the band gap (sample BL12C). (a)  $I - V$  curve measured at the Dirac point of the bipolar region with  $V_{bg} = 40$  V and  $V_{tg} = -3$  V. (b) The corresponding differential conductance  $dI/dV$  versus voltage  $V$ .

**Switch off the supercurrent within the band gap.** By applying a displacement field, it is possible to open a band gap in the bilayer graphene band structure. When the Fermi level of the charge carriers is tuned within the band gap, the supercurrent can be switched off. In our measurements, we observe that the supercurrent can be turned off even before the gap is opened completely. Figure 4.23a shows the  $I - V$  characteristic measured with  $V_{bg} = 40$  V and  $V_{tg} = -3$  V. The supercurrent is suppressed in the top-gated region, whereas a missing Coulomb blockade close to zero voltage indicates that the gap is not open. In this situation, the multiple Andreev reflection is smeared, as shown in Figure 4.23b.

## 4.9 Fraunhofer diffraction pattern

In this section, we investigate the dependence of the critical current  $I_c^m$  on the magnetic field in a bilayer graphene Josephson junction. The measurements have been performed at  $V_{bg} = 20$  V and  $V_{tg} = 1.5$  V. As depicted in Figure 4.24a, for  $B < 1$  mT, the oscillation of the current  $I_c^m$  exhibits the Fraunhofer diffraction pattern, indicating a homogeneous supercurrent density distribution. The first four side lobes are plotted in Figure 4.24b, where the line is drawn according to Equation (4.12) and the points are extracted from experiments. The observed pattern of  $I_c^m$  quantitatively coincides

with the theoretical prediction [89]. The period of each lobe corresponds to a flux quantum. The experimentally measured value for the period is  $0.25 \pm 0.05$  mT, which has a good agreement with the theoretically predicted value 0.26 mT according to  $\Delta B = \Phi_0/(L+2\lambda)W$ . The parameters used in the calculation are as follows:  $\lambda = 0.38$   $\mu\text{m}$  [75],  $L = 1$   $\mu\text{m}$ , and  $W = 5$   $\mu\text{m}$ . The London penetration depth of Al we used is consistent with the values reported in literatures (200  $\sim$  500 nm) [75, 90, 91].

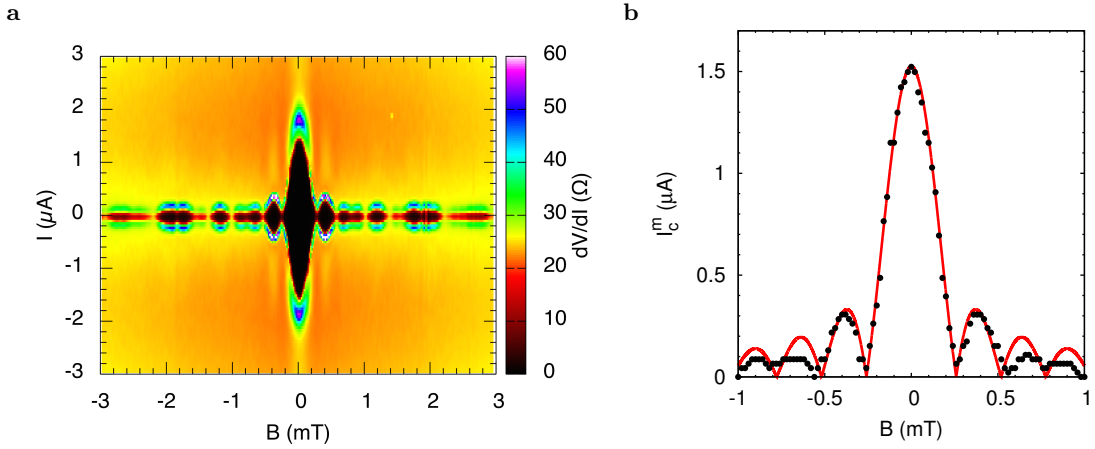


**Figure 4.24:** Fraunhofer diffraction pattern (sample BL12C). (a) The dependence of the critical current on the magnetic field. The color scaled plot is the differential resistance with respect to the magnetic field  $B$  and the current  $I$ . The dark region corresponds to the superconducting state. The measurements have been done at  $V_{bg} = 20$  V and  $V_{tg} = 1.5$  V. (b) Comparison of the theoretical and experimentally measured maximum critical currents in the range of  $B = -1 \sim 1$  mT. The black-filled circles are the experimental data and the red solid curve is according to Equation (4.12).

For  $B > 1$  mT, the current  $I_c^m$  can survive but does not obey the theory given by Equation (4.12). A remnant of  $I_c^m$  is observed for  $B > 1$  mT (vanishes completely  $\sim 5$  mT).

As described in Section 4.1.7, the trajectories of the electron or hole bend in the magnetic field. The Andreev reflection cannot sustain in the bulk when the magnetic field is larger than the critical value of 1 mT. Because the phase difference between the incident electron and the reflected hole is large enough, the reflected hole does not trace back the path of the electron (see Figure 4.11c) [64]. The Andreev reflection only occurs at the edge of the graphene flake, which gives rise to the random pockets in Figure 4.24a for  $B > 1$  mT. The suppression of the Andreev reflection in a higher magnetic field is further observed in the evolution of the subharmonic gap structure in the magnetic field, as shown in Figure 4.25. As the magnetic field increases, the peaks located at  $2\Delta/3e$ ,  $2\Delta/2e$ ,  $2\Delta/e$  vanish in sequence. The dependence of the multiple Andreev reflection on

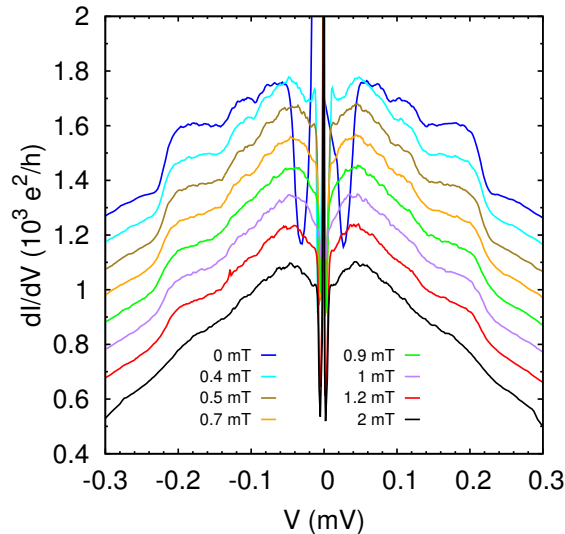


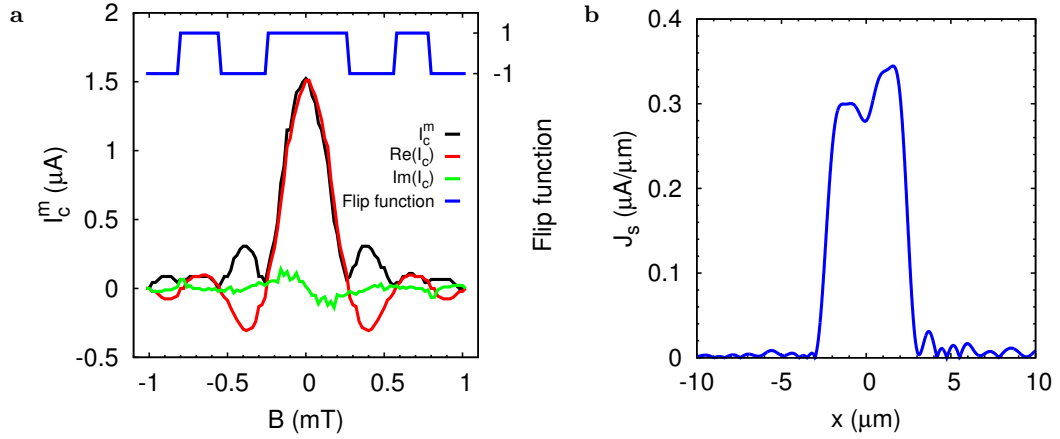
**Figure 4.25:** The evolution of the subharmonic gap structures in the low magnetic field (sample BL12C).

the magnetic field is in good agreement with the variation of  $I_c^m$  in the magnetic field, as seen in Figure 4.24a.

The spatial distribution of the critical current density  $J_c(x)$  can be determined by measuring the dependence of  $I_c^m$  on the magnetic field [92]. Here, we perform a complex Fourier transform to derive the current distribution  $J_c(x)$  according to Equation (4.11). It is essential to recover the complex supercurrent  $I_c$  from the measured  $I_c^m$  [90], which can be approximately realized when the current density  $J_c(x)$  is symmetrical with respect to the midpoint of the junction. This assumption requires that the value of  $I_c^m$  at each minimum goes to zero, so that the imaginary part of  $\text{Im}(I_c)$  vanishes and the real part becomes dominant  $I_c = \text{Re}(I_c)$ . Then,  $I_c$  is restored approximately by multiplying  $I_c^m$  with a flip function that changes sign between the adjacent lobes, as shown in Figure 4.26a. Applying the inverse Fourier transform to  $I_c$ , we obtain the supercurrent density

$$J_c(x) = \left| \frac{1}{2\pi} \int_{-W/2}^{W/2} I_c(k) e^{-ikx} dk \right|. \quad (4.41)$$

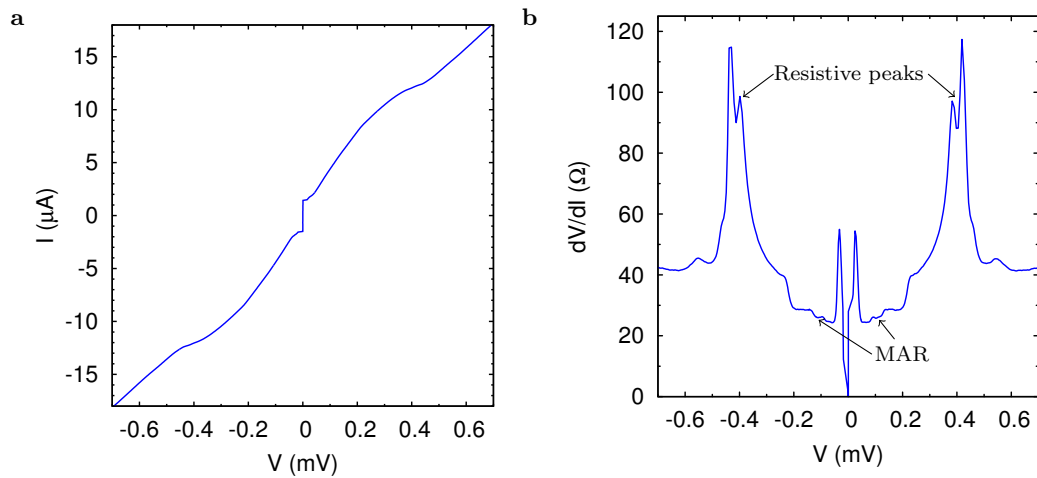
The spatial distribution of the supercurrent density  $J_c(x)$  is depicted in Figure 4.26b. The codes for calculation is attached in Appendix B. The critical supercurrent density shows a plateau around  $0.3 \sim 0.35 \mu\text{A } \mu\text{m}^{-1}$  within the range of the junction and decreases to nearly zero out of the junction. The half width of the plateau is consistent with the junction width of  $5 \mu\text{m}$ .



**Figure 4.26:** The critical current density along the junction. (a) Principle of the complex Fourier transformation. The complex critical current is recovered by apply a flip function (blue curve) to the experimentally measured maximum current (black curve). The real and imaginary components of the recovered critical current are shown by the red and green curves, respectively. (b) The critical current density obtained using Equation (4.11).

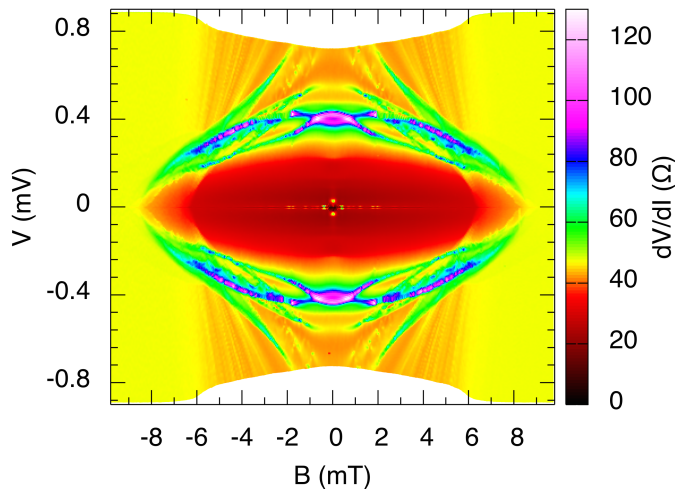
#### 4.10 Resistance peaks above $2\Delta$

Figure 4.27a and Figure 4.27b present the  $I - V$  curve and the corresponding differential resistance  $dV/dI$ , respectively. The experimental data are measured at  $V_{bg} = 20$  V and  $V_{tg} = 1.5$  V. The  $I - V$  curve exhibits a non-linear behavior before it reaches its linear limit at high bias voltage. The non-linear characteristic is shown more clearly in the differential resistance  $dV/dI$  versus  $V$  curve. For  $V < 2\Delta/e$ , the non-linearity originates from the multiple Andreev reflection, which displays as a series of resistance minima at  $V = 2\Delta/ne$ . For  $V > 2\Delta/e$ , a few highly resistive peaks occur near  $V = \pm 0.4$  mV.



**Figure 4.27:** (a) The  $I - V$  curve measured for the sample BL12C with  $V_{bg} = 20$  V and  $V_{tg} = 1.5$  V. (b) The corresponding differential resistance versus voltage.

To figure out the origin of these resistive peaks above  $2\Delta$  in Figure 4.27b, we examine the dependence of the peaks on the magnetic field. Figure 4.28 illustrates the differential resistance as a function of the bias voltage  $V$  and the magnetic field  $B$ , which is measured at  $V_{bg} = 20$  V and  $V_{tg} = 1.5$  V. With increasing magnetic field, the series of the peaks at high voltage firstly diverge and cross with each other, then converge, and finally vanish around  $B = 10$  mT. It is interesting to note that the peaks disappear together with the induced superconductivity, which has a critical field of  $\sim 10$  mT. This phenomenon has been observed in SNS junctions using single-layer graphene [93], bilayer graphene [94], and InN [95].



**Figure 4.28:** The differential resistance as a function of the magnetic field and the voltage for the sample BL12C.

We further investigate the effect of  $V_{bg}$  and  $V_{tg}$  on the resistive peaks. Figure 4.29a shows the differential resistance versus voltage for various back-gate voltages with a constant top-gate voltage of  $V_{tg} = 2$  V. The curves are measured for the sample BL12D in the nnnn regime. We note that, with an increase of the back-gate voltage, the positions of the resistive peaks move close to  $V = 2\Delta/e$  and the separation between each peak decreases slightly. The positions of the three-most pronounced peaks as a function of the back-gate voltage is portrayed in Figure 4.29b. It shows that the back-gate voltage strongly affects the positions of those peaks rather than their separation. The trend that the positions of the peaks vary with the back-gate voltage is similar to the relation between the normal state resistance  $R_n$  and  $V_{bg}$ . In addition, a comparison of Figure 4.29a with Figure 4.27b shows that the number of the peaks is sensitive to the length of the samples. More peaks occur in the shorter sample BL12D in comparison with the sample BL12C. In addition, the previous results, reported by Bordaz [94], show that more than ten peaks are observed for a shorter device with a length of 310 nm.

In a conventional Josephson junction, similar phenomena have been found and termed Tomasch resonance [96, 97] and McMillan-Rowell resonance [98, 99]. Both are related

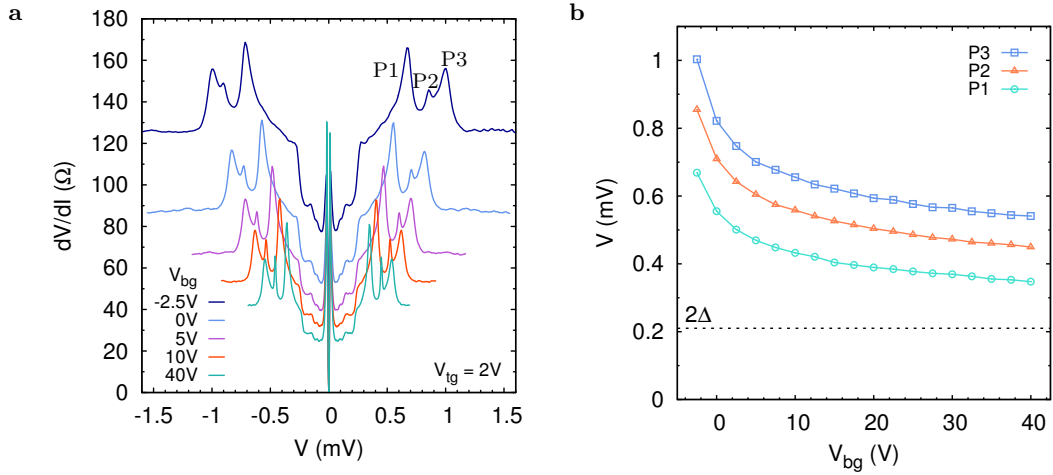


**Figure 4.29:** (a) The differential resistance versus voltage curves for various back-gate voltages with the  $V_{tg}$  fixed at 2 V (Sample BL12D). (b) The positions of the three-most pronounced peaks in (a) vary with respect to the back-gate voltage.

to the geometry of the junction. Tomasch resonance originates from the interference of quasiparticles in the S side. An electron-like quasiparticle is incident on the S/N interface and reflected back as a hole-like quasi-particle due to the local perturbation of the energy gap. The interference occurs between the incident electron-like quasiparticle and the reflected hole-like counterpart. This gives rise to a series of resistance peaks at voltages [97]

$$eV_n = \sqrt{(2\Delta)^2 + (nhv_F^S/2d_s)^2}, \quad (4.42)$$

where  $n$  is an integer,  $v_F^S$  is the Fermi velocity in the superconductor, and  $d_s$  is its thickness. The McMillan-Rowell resonance originates from the interference in the normal metal. The incident electron from the normal side goes through the first Andreev reflection at the N/S interface. The reflected hole cannot interfere with the incident electron, so that it is reflected as a hole at the opposite interface. When the reflected hole arrives at the N/S interface again, it undergoes the second Andreev reflection and returns to the electron state, which interferes with the incident electron. The interference generates the resistive peaks with the spacing [98]

$$\Delta V = hv_F^N/4ed_N, \quad (4.43)$$

where  $v_F^N$  is the Fermi velocity in the normal metal and  $d_N$  is its thickness.

Unfortunately, neither Tomasch resonances nor McMillan-Rowell resonances can explain the resistance peaks observed in the present work. In the case of Tomasch resonances, the positions of the peaks predicted by Equation (4.42) do not fit to our measurement since they are independent of the gate voltage. In the case of McMillan-Rowell resonances,  $\Delta V$  increases with  $v_F^N$  in bilayer graphene which can be tuned by the gate voltage. Thus

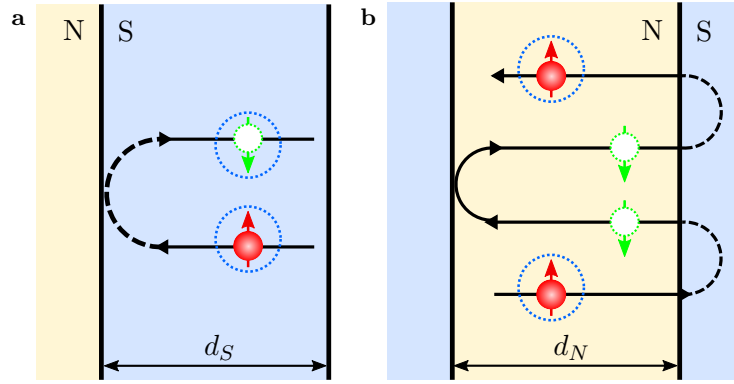


**Figure 4.30:** The schematics of the Tomasch resonances (a) and the McMillan-Rowell resonances (b). Figures adapted from Ref. [100].

both models fail to describe the resistance resonance in our experiment. We therefore assume that the resistance peaks are due to the interference from the graphene side, which is similar to the McMillan-Rowell resonances, since the number of the resistance peaks is linked to the length of bilayer graphene and their positions are associated with the normal state resistance. Nevertheless, a new model is required to determine the resonances in a Josephson junction using graphene as the normal metal.

## 4.11 Conclusion

The induced supercurrent has been observed in ballistic Josephson junctions based on bilayer graphene. The largest  $I_c R_n$  product of  $0.72\Delta/e$  is realized for a  $1 \mu\text{m}$  long distance. The supercurrent density is homogeneous along the junction, which is demonstrated by the measurement of the Fraunhofer diffraction pattern. The on- and off-states for the supercurrent are controlled by operating the dual-gates. The influence of anti-Klein tunneling on the suppression of the supercurrent is most likely to govern the proximity-induced superconductivity in bilayer graphene. In addition, we have discussed the resistive peaks at higher energies ( $> 2\Delta$ ) and have noticed that they are associated with the induced superconductivity.

# Conclusions

In this thesis, we have investigated the transport properties of bilayer graphene p-n-p junctions at cryogenic temperatures. We benefit from the advanced sample fabrication techniques, in particular the van der Waals assembly of graphene between two hBN films, which allows us to produce high quality devices. This type of devices enables ballistic transport over long distances,  $L \gtrsim 8.8 \mu\text{m}$  in our case, enabling us to probe a variety of quantum transport phenomena in the ballistic regime.

Fabry-Pérot interference of electrons has been directly observed from conductance measurements. The amplitudes of the oscillations are large, which is the signature of ballistic interference in p-n junctions. At low magnetic fields, i.e. when no quantum Hall effect is observed, we have studied the influence of the interlayer asymmetry on the Fabry-Pérot interference. We found that the phase shifts in the interference patterns occur at low energies, but vanish at high energies. This corresponds to that the Berry phase has changed from  $\pi$  to  $2\pi$  when tuning the Fermi level from the band edge to high energies. Therefore, it is evident that a transition from the single-layer-like Klein tunneling to bilayer-like anti-Klein tunneling takes place .

The samples are contacted with Ti/Al leads, allowing to probe the induced superconductivity in bilayer graphene p-n junctions. In the unipolar regime, a large supercurrent  $I_c$  has been observed, reaching  $1.72 \mu\text{A}$  at the charge carrier density of  $2.23 \times 10^{12} \text{ cm}^{-2}$ . The corresponding  $I_c R_n$  product is  $0.72\Delta/e$ , which is very high for a  $1\text{-}\mu\text{m}$  long device. At finite voltages, we observe multiple Andreev reflections. In the bipolar regime, the angular transmission probability of charge carriers affects the phase coherent Andreev reflections as well. Hence, the supercurrent decreases or even switches off. By modulating the electrical field, we tune the Fermi level to the band edges. The superconductivity is completely suppressed because of a band gap opening. Hence, we can realize the supercurrent on- and off-state by controlling the electrical field, which is crucial for applications of superconducting transistors.

In this thesis, we have revealed some questions whose answers need further understanding. In p-n junctions, multiple Andreev reflection is reduced dramatically due to the

---

small angular transmission probability. Yet, the very existence of multiple Andreev reflection illustrates that the phase-coherent Andreev reflection can survive in the p-n junctions. The break-down of the Andreev bound states, for example in the bipolar regime of the Sample BL12D, only occurs at the zero-voltage state. This phenomenon remains presently unexplained. Another question may call for theoretic explanation as well. We found that the  $I - V$  curves exhibit highly resistive gate-tunable peaks at finite voltage where  $V > 2\Delta$ . The peaks may be related to the interactions between this highly tunable superconducting circuits and the electromagnetic environment of the samples. However, this needs further investigations.

## Appendix A

# Matlab codes for calculating angular transmission probabilities in bilayer graphene

The following codes has been used to calculate the angular transmission probabilities in gapless bilayer graphene in Chapter 3. The corresponding results are presented in Figure 3.4.

```
clear all
clf

%-----parameters-----

me      = 9.1093821545e-31; %unit Kg
h_bar   = 1.05457172647e-34; %unit J*s
m       = 0.0355*me;

E       = 20e-3*1.60217656535e-19; % unit J
V0      = 50e-3*1.60217656535e-19; % unit J
a       = 200e-9; %unit nm

M       = zeros(8,8);
b       = zeros(8,1);
k       = sqrt(2*m*E)/h_bar;
q       = sqrt(2*m*abs(V0-E))/h_bar;
i       = sqrt(-1);
```

```

fp=fopen('output.dat','w');

for phi=(-pi/2):(pi/2000):(pi/2)

a3=zeros(8,1);

kx      = k*cos(phi);
ky      = k*sin(phi);
theta   = asin(ky/q);
qx      = q*cos(theta);

kappax  = k*sqrt(1.0 + sin(phi)*sin(phi) );
lambdax = q*sqrt(1.0 + sin(theta)*sin(theta) );

s       = sign(E);
s1      = sign(E-V0);
h1      = (sqrt(1.0 + sin(phi)*sin(phi)) - sin(phi) )^2;
h2      = (sqrt(1.0 + sin(theta)*sin(theta)) - sin(theta) )^2;

%-----matrix M-----
% b1 c1 a2 b2 c2 d2 a3 d3
% 1  2  3  4  5  6  7  8
M(1,1) = e^(-i*kx*(-a));
M(1,2) = e^(kappax*(-a));
M(1,3) = -e^(i*qx*(-a));
M(1,4) = -e^(-i*qx*(-a));
M(1,5) = -e^(lambdax*(-a));
M(1,6) = -e^(-lambdax*(-a));
M(1,7) = 0.0;
M(1,8) = 0.0;

M(2,1) = -i*kx*e^(-i*kx*(-a));
M(2,2) = kappax*e^(kappax*(-a));
M(2,3) = -i*qx*e^(i*qx*(-a));
M(2,4) = i*qx*e^(-i*qx*(-a));
M(2,5) = -lambdax*e^(lambdax*(-a));

```

```

M(2,6) = lambdax*e^(-lambdax*(-a));
M(2,7) = 0.0;
M(2,8) = 0.0;

M(3,1) = s*e^(-i*(2.0*phi + kx*(-a)) );
M(3,2) = -s*h1*e^(kappax*(-a));
M(3,3) = -s1*e^(i*(2.0*theta + qx*(-a)) );
M(3,4) = -s1*e^(-i*(2.0*theta + qx*(-a)) );
M(3,5) = s1*h2*e^(lambdax*(-a));
M(3,6) = (s1/h2)*e^(-lambdax*(-a));
M(3,7) = 0.0;
M(3,8) = 0.0;

M(4,1) = -i*kx*s*e^(-i*(2.0*phi + kx*(-a)) );
M(4,2) = -kappax*s*h1*e^(kappax*(-a));
M(4,3) = -i*qx*s1*e^(i*(2.0*theta + qx*(-a)) );
M(4,4) = i*qx*s1*e^(-i*(2.0*theta + qx*(-a)) );
M(4,5) = lambdax*s1*h2*e^(lambdax*(-a));
M(4,6) = -lambdax*(s1/h2)*e^(-lambdax*(-a));
M(4,7) = 0.0;
M(4,8) = 0.0;
% b1 c1 a2 b2 c2 d2 a3 d3
% 1 2 3 4 5 6 7 8

M(5,1) = 0.0;
M(5,2) = 0.0;
M(5,3) = e^(i*qx*a);
M(5,4) = e^(-i*qx*a);
M(5,5) = e^(lambdax*a);
M(5,6) = e^(-lambdax*a);
M(5,7) = -e^(i*kx*a);
M(5,8) = -e^(-kappax*a);

M(6,1) = 0.0;
M(6,2) = 0.0;
M(6,3) = i*qx*e^(i*qx*a);
M(6,4) = -i*qx*e^(-i*qx*a);

```

```

M(6,5) = lambdax*e^(lambdax*a);
M(6,6) = -lambdax*e^(-lambdax*a);
M(6,7) = -i*kx*e^(i*kx*a);
M(6,8) = kappax*e^(-kappax*a);

M(7,1) = 0.0;
M(7,2) = 0.0;
M(7,3) = s1*e^(i*(2*theta + qx*a));
M(7,4) = s1*e^(-i*(2*theta + qx*a));
M(7,5) = -s1*h2*e^(lambdax*a);
M(7,6) = -(s1/h2)*e^(-lambdax*a);
M(7,7) = -s*e^(i*(2*phi + kx*a));
M(7,8) = (s/h1)*e^(-kappax*a);

M(8,1) = 0.0;
M(8,2) = 0.0;
M(8,3) = i*qx*s1*e^(i*(2*theta + qx*a));
M(8,4) = -i*qx*s1*e^(-i*(2*theta + qx*a));
M(8,5) = -lambdax*s1*h2*e^(lambdax*a);
M(8,6) = lambdax*(s1/h2)*e^(-lambdax*a);
M(8,7) = -i*kx*s*e^(i*(2*phi + kx*a));
M(8,8) = -kappax*(s/h1)*e^(-kappax*a);

b(1,1) = -e^(i*kx*(-a));
b(2,1) = -i*kx*e^(i*kx*(-a));
b(3,1) = -s*e^(i*(2*phi + kx*(-a) ));
b(4,1) = -i*kx*s*e^(i*(2*phi + kx*(-a) ));
b(5,1) = 0.0;
b(6,1) = 0.0;
b(7,1) = 0.0;
b(8,1) = 0.0;

a3=inv(M)*b;
t=abs(a3(7,1));
T=t**2;

```

```
fprintf(fp, '%e %e\n', phi, T);  
endfor  
  
fclose(fp);
```



## Appendix B

# Matlab codes for extracting the Josephson current density

The spatial distribution of Josephson current along the junction is calculated with the complex Fourier transformation. The resulting Josephson current density is shown in Figure 4.26b.

```
clear all;

%Flip the Ic to obtain complex Ic

%read data
M1=dlmread('Ic_B.dat');
a1=size(M1);

%Ic minima position
N=[];
p=0;
for q=0:1:a1(1)
if (M1(k,2)<1e-9)
p=p+1;
    N(p,1)=q;
end
end

%flip Ic
b=size(N);
```

```
i=1;
j=1;
flip=1;
fp1=fopen('Ic_flip.dat', 'w');
while (i<=a1(1))

while (i<=N(j))
Icflip=M1(i,2)*flip;
fprintf(fp1,'%e %e %e \n',M1(i,1), M1(i,2), Icflip);
i+=1;
end
j+=1;
flip=-1*flip;
end

fclose(fp1);

%Fourier transform of complex Ic to obtain the real and imaginary
%components

clear all;
M2=dlmread('Ic_flip.dat');
a2=size(M2);

fp2=fopen('Fraunhofer_f.dat', 'w');

for k=0:1:(a2(1)-1)
Xk_real = 0;
Xk_imag = 0;
for n=0:1:(a2(1)-1)
xn      = M2(n+1,3); %xn=Ic
Xk_real = Xk_real + xn*cos(2*pi*k*n/a(1));
Xk_imag = Xk_imag - xn*sin(2*pi*k*n/a(1));

end

fprintf(fp2,'%e %e %e %e\n',k, Xk_real, Xk_imag,
sqrt(Xk_real^2+Xk_imag^2));
end
```

```

fclose(fp2);

% Inverse fourier transformation to recover Ic together with its real
%and imaginary components
clear all;
M3=dlmread('Fraunhofer_f.dat');
a3=size(M3);

fp3=fopen('Ic_B_DFTfit.dat', 'w');

for n=0:1:299
xn_real = 0;
xn_imag = 0;
for k=0:1:(a3(1)-1)
Xk_real = M3(k+1,2);
Xk_imag = M3(k+1,3);
xn_real = xn_real + Xk_real*cos(2*pi*k*n/300)/300;
xn_imag = xn_imag - Xk_imag*sin(2*pi*k*n/300)/300;

end
xn      = xn_real+xn_imag;
ampxn   = sqrt(xn_real**2+xn_imag**2);
B=n*0.02; %0.02 is measurement step for B
fprintf(fp, '%e %e %e %e %e %e\n', n, xn_real, xn_imag, xn, ampxn, B);
end

fclose(fp3);

% Calculate the current density Jc

clear all;
M4=dlmread('Ic_B_DFTfit.dat');
a4=size(M4);

fp4=fopen('current_density.dat', 'w');

L=1e-6;
lambda=0.38*1e-6;

```

```
h=6.62606957*1e-34;
e=-1.602176565*1e-19;
Phi0=h/2/e;
alpha=2*pi*(L+2*lambda)/Phi0;

for n=0:1:1000
x=(n-500)*1e-8; %unit m
%the origin of x is in the center of the junction
J_real=0;
J_imag=0;
for k=1:1:a4(1)
B = M4(k,6)*1e-3;
Ic_real = M4(k,2)*1e-6; % unit A
Ic_imag = M4(k,3)*1e-6; % unit A
J_real = J_real + (Ic_real*cos(alpha*B*x)+Ic_imag*sin(alpha*B*x))*
(alpha*2*1e-5)/(2*pi);
J_imag = J_imag + (Ic_imag*cos(alpha*B*x)-Ic_real*sin(alpha*B*x))*
(alpha*2*1e-5)/(2*pi);
end
J = sqrt(J_real**2+J_imag**2);
fprintf(fp4, '%e %e %e %e \n',x, J_real,J_imag, J);
end

fclose(fp4);
```

# Bibliography

- [1] P. R. Wallace. The band theory of graphite. *Physical Review*, 71(9):622, 1947.
- [2] K. S. Novoselov, A. K. Geim, S. V. Morozov, D. Jiang, Y. Zhang, S. V. Dubonos, I. V. Grigorieva, and A. A. Firsov. Electric field effect in atomically thin carbon films. *Science*, 306(5696):666–669, 2004.
- [3] K. S. Novoselov, A. K. Geim, S. V. Morozov, D. Jiang, M. I. Katsnelson, I. V. Grigorieva, S. V. Dubonos, and A. A. Firsov. Two-dimensional gas of massless Dirac fermions in graphene. *Nature*, 438(7065):197–200, 2005.
- [4] K. I. Bolotin, K. J. Sikes, Z.D. Jiang, M. Klima, G. Fudenberg, J. Hone, P. Kim, and H. L. Stormer. Ultrahigh electron mobility in suspended graphene. *Solid State Communications*, 146(9):351–355, 2008.
- [5] Y.-M. Lin, C. Dimitrakopoulos, K. A. Jenkins, D. B. Farmer, H.-Y. Chiu, A. Grill, and Ph. Avouris. 100-GHz transistors from wafer-scale epitaxial graphene. *Science*, 327(5966):662–662, 2010.
- [6] F. Schwierz. Graphene transistors. *Nature Nanotechnology*, 5(7):487–496, 2010.
- [7] M. I. Katsnelson, K. S. Novoselov, and A. K. Geim. Chiral tunnelling and the Klein paradox in graphene. *Nature Physics*, 2(9):620–625, 2006.
- [8] A. F. Young and P. Kim. Quantum interference and Klein tunnelling in graphene heterojunctions. *Nature Physics*, 5(3):222–226, 2009.
- [9] E. McCann and M. Koshino. The electronic properties of bilayer graphene. *Reports on Progress in Physics*, 76(5):056503, 2013.
- [10] J. B. Oostinga, H. B. Heersche, X. Liu, A. F. Morpurgo, and L. M. K. Vandersypen. Gate-induced insulating state in bilayer graphene devices. *Nature Materials*, 7(2):151–157, 2008.
- [11] E. V. Castro, K. S. Novoselov, S. V. Morozov, N. M. R. Peres, J. M. B. Lopes dos Santos, J. Nilsson, F. Guinea, A. K. Geim, and A. H. Castro Neto. Biased bilayer

- graphene: semiconductor with a gap tunable by the electric field effect. *Physical Review Letters*, 99(21):216802, 2007.
- [12] A. Varlet, M.-H. Liu, V. Krueckl, D. Bischoff, P. Simonet, K. Watanabe, T. Taniguchi, K. Richter, K. Ensslin, and T. Ihn. Fabry-Pérot interference in gapped bilayer graphene with broken anti-Klein tunneling. *Physical Review Letters*, 113(11):116601, 2014.
- [13] C. R. Dean, A. F. Young, I. Meric, C. Lee, L. Wang, S. Sorgenfrei, K. Watanabe, T. Taniguchi, P. Kim, K. L. Shepard, and J. Hone. Boron nitride substrates for high-quality graphene electronics. *Nature Nanotechnology*, 5(10):722–726, 2010.
- [14] L. Wang, I. Meric, P. Y. Huang, Q. Gao, Y. Gao, H. Tran, T. Taniguchi, K. Watanabe, L. M. Campos, D. A. Muller, J. Guo, P. Kim, J. Hone, K. L. Shepard, and C. R. Dean. One-dimensional electrical contact to a two-dimensional material. *Science*, 342(6158):614–617, 2013.
- [15] P. A. M. Dirac. The quantum theory of the electron. *Proceedings of the Royal Society of London A: Mathematical, Physical and Engineering Sciences*, 117(778):610–624, 1928.
- [16] A. K. Geim and K. S. Novoselov. The rise of graphene. *Nature Materials*, 6(3):183–191, 2007.
- [17] K. S. Novoselov, D. Jiang, F. Schedin, T. J. Booth, V. V. Khotkevich, S. V. Morozov, and A. K. Geim. Two-dimensional atomic crystals. *Proceedings of the National Academy of Sciences of the United States of America*, 102(30):10451–10453, 2005.
- [18] J. Tworzydło, Björn Trauzettel, M. Titov, A. Rycerz, and C. W. J. Beenakker. Sub-Poissonian shot noise in graphene. *Physical Review Letters*, 96(24):246802, 2006.
- [19] Y. Zhang, Y.-W. Tan, H. L. Stormer, and P. Kim. Experimental observation of the quantum Hall effect and Berry’s phase in graphene. *Nature*, 438(7065):201–204, 2005.
- [20] A. B. Kuzmenko, I. Crassee, D. Van Der Marel, P. Blake, and K. S. Novoselov. Determination of the gate-tunable band gap and tight-binding parameters in bilayer graphene using infrared spectroscopy. *Physical Review B*, 80(16):165406, 2009.
- [21] R. E. Doezema, W. R. Datars, H. Schaber, and A. Van Schyndel. Far-infrared magnetospectroscopy of the Landau-level structure in graphite. *Physical Review B*, 19(8):4224, 1979.

- [22] Y. Zhang, T.-T. Tang, C. Girit, Z. Hao, M. C. Martin, A. Zettl, M. F. Crommie, Y. Ron Shen, and F. Wang. Direct observation of a widely tunable bandgap in bilayer graphene. *Nature*, 459(7248):820–823, 2009.
- [23] T. Taychatanapat and P. Jarillo-Herrero. Electronic transport in dual-gated bilayer graphene at large displacement fields. *Physical Review Letters*, 105(16):166601, 2010.
- [24] T. Ohta, A. Bostwick, T. Seyller, K. Horn, and E. Rotenberg. Controlling the electronic structure of bilayer graphene. *Science*, 313(5789):951–954, 2006.
- [25] P. Blake, E. W. Hill, A. H. Castro Neto, K. S. Novoselov, D. Jiang, R. Yang, T. J. Booth, and A. K. Geim. Making graphene visible. *Applied Physics Letters*, 91(6):063124, 2007.
- [26] A. C. Ferrari, J. C. Meyer, V. Scardaci, C. Casiraghi, M. Lazzeri, F. Mauri, S. Piscanec, D. Jiang, K. S. Novoselov, S. Roth, and A. K. Geim. Raman spectrum of graphene and graphene layers. *Physical Review Letters*, 97(18):187401, 2006.
- [27] L. M. Malard, J. Nilsson, D. C. Elias, J. C. Brant, F. Plentz, E. S. Alves, A. H. Castro Neto, and M. A. Pimenta. Probing the electronic structure of bilayer graphene by Raman scattering. *Physical Review B*, 76(20):201401, 2007.
- [28] S. J. Haigh, A. Gholinia, R. Jalil, S. Romani, L. Britnell, D. C. Elias, K. S. Novoselov, L. A. Ponomarenko, A. K. Geim, and R. Gorbachev. Cross-sectional imaging of individual layers and buried interfaces of graphene-based heterostructures and superlattices. *Nature Materials*, 11(9):764–767, 2012.
- [29] F. Mueller, R. N. Schouten, M. Brauns, T. Gang, W. H. Lim, N. S. Lai, A. S. Dzurak, W. G. van der Wiel, and F. A. Zwanenburg. Printed circuit board metal powder filters for low electron temperatures. *Review of Scientific Instruments*, 84(4):044706, 2013.
- [30] Y.-W. Tan, Y. Zhang, K. Bolotin, Y. Zhao, S. Adam, E. H. Hwang, S. Das Sarma, H. L. Stormer, and P. Kim. Measurement of scattering rate and minimum conductivity in graphene. *Physical Review Letters*, 99(24):246803, 2007.
- [31] O. Klein. Die Reflexion von Elektronen an einem Potentialsprung nach der relativistischen Dynamik von Dirac. *Zeitschrift für Physik*, 53(3-4):157–165, 1929.
- [32] F. Sauter. Über das Verhalten eines Elektrons im homogenen elektrischen Feld nach der relativistischen Theorie Diracs. *Zeitschrift für Physik*, 69(11-12):742–764, 1931.

- [33] A. V. Shytov, M. S. Rudner, and L. S. Levitov. Klein backscattering and Fabry-Pérot interference in graphene heterojunctions. *Physical Review Letters*, 101(15):156804, 2008.
- [34] M. I. Katsnelson. *Graphene: Carbon in two dimensions*. Cambridge University Press, 2012.
- [35] T. Tudorovskiy, K. J. A. Reijnders, and M. I. Katsnelson. Chiral tunneling in single-layer and bilayer graphene. *Physica Scripta*, 2012(T146):014010, 2012.
- [36] J. C. Slonczewski and P. R. Weiss. Band structure of graphite. *Physical Review*, 109(2):272, 1958.
- [37] V. V. Cheianov and V. I. Fal’ko. Selective transmission of Dirac electrons and ballistic magnetoresistance of n-p junctions in graphene. *Physical Review B*, 74(4):041403, 2006.
- [38] F. Bernardini, V. Fiorentini, and D. Vanderbilt. Spontaneous polarization and piezoelectric constants of III-V nitrides. *Physical Review B*, 56(16):R10024, 1997.
- [39] K. S. Novoselov, E. McCann, S. V. Morozov, V. I. Fal’ko, M. I. Katsnelson, U. Zeitler, D. Jiang, F. Schedin, and A. K. Geim. Unconventional quantum Hall effect and Berry’s phase of  $2\pi$  in bilayer graphene. *Nature Physics*, 2(3):177–180, 2006.
- [40] D. Xiao, J. Shi, and Q. Niu. Berry phase correction to electron density of states in solids. *Physical Review Letters*, 95(13):137204, 2005.
- [41] J. E. Avron, A. Elgart, G. M. Graf, and L. Sadun. Geometry, statistics, and asymptotics of quantum pumps. *Physical Review B*, 62(16):R10618, 2000.
- [42] M. V. Berry. Quantal phase factors accompanying adiabatic changes. *Proceedings of the Royal Society of London A: Mathematical, Physical and Engineering Sciences*, 392(1802):45–57, 1984.
- [43] D. Xiao, M.-C. Chang, and Q. Niu. Berry phase effects on electronic properties. *Reviews of Modern Physics*, 82(3):1959, 2010.
- [44] A. Varlet, M.-H. Liu, D. Bischoff, P. Simonet, T. Taniguchi, K. Watanabe, K. Richter, T. Ihn, and K. Ensslin. Band gap and broken chirality in single-layer and bilayer graphene. *arXiv preprint arXiv:1508.02648*, 2015.
- [45] A. F. Young. *Quantum transport in graphene heterostructures*. PhD thesis, Columbia University, 2011.

- [46] R. T. Weitz, M. T. Allen, B. E. Feldman, J. Martin, and A. Yacoby. Broken-symmetry states in doubly gated suspended bilayer graphene. *Science*, 330(6005):812–816, 2010.
- [47] K. Zou and J. Zhu. Transport in gapped bilayer graphene: The role of potential fluctuations. *Physical Review B*, 82(8):081407, 2010.
- [48] F. Xia, D. B. Farmer, Y. Lin, and P. Avouris. Graphene field-effect transistors with high on/off current ratio and large transport band gap at room temperature. *Nano letters*, 10(2):715–718, 2010.
- [49] L. Jing, J. Velasco Jr, P. Kratz, G. Liu, W. Bao, M. Bockrath, and C. N. Lau. Quantum transport and field-induced insulating states in bilayer graphene pnp junctions. *Nano Letters*, 10(10):4000–4004, 2010.
- [50] H. Miyazaki, K. Tsukagoshi, A. Kanda, M. Otani, and S. Okada. Influence of disorder on conductance in bilayer graphene under perpendicular electric field. *Nano Letters*, 10(10):3888–3892, 2010.
- [51] J. S. Alden, A. W. Tsen, P. Y. Huang, R. Hovden, L. Brown, J. Park, D. A. Muller, and P. L. McEuen. Strain solitons and topological defects in bilayer graphene. *Proceedings of the National Academy of Sciences*, 110(28):11256–11260, 2013.
- [52] L. Ju, Z. Shi, N. Nair, Y. Lv, C. Jin, J. Velasco Jr, C. Ojeda-Aristizabal, H. A. Bechtel, M. C. Martin, A. Zettl, J. Analytis, and F. Wang. Topological valley transport at bilayer graphene domain walls. *Nature*, 520(7549):650–655, 2015.
- [53] P. San-Jose, R. V. Gorbachev, A. K. Geim, K. S. Novoselov, and F. Guinea. Stacking boundaries and transport in bilayer graphene. *Nano Letters*, 14(4):2052–2057, 2014.
- [54] M. Koshino. Electronic transmission through AB-BA domain boundary in bilayer graphene. *Physical Review B*, 88(11):115409, 2013.
- [55] F. Xia, V. Perebeinos, Y.-M. Lin, Y. Wu, and P. Avouris. The origins and limits of metal-graphene junction resistance. *Nature Nanotechnology*, 6(3):179–184, 2011.
- [56] P. Rickhaus, R. Maurand, M.-H. Liu, M. Weiss, K. Richter, and C. Schönenberger. Ballistic interferences in suspended graphene. *Nature Communications*, 4:2342, 2013.
- [57] M. Tinkham. *Introduction to superconductivity*. McGraw-Hill, 1975.
- [58] B. D. Josephson. Possible new effects in superconductive tunnelling. *Physics Letters*, 1(7):251–253, 1962.

- [59] K. K. Likharev. Superconducting weak links. *Reviews of Modern Physics*, 51(1):101, 1979.
- [60] I. F. Quercia. Physics and applications of the Josephson effect. *Il Nuovo Cimento D*, 4(4):411–412, 1984.
- [61] G. E. Blonder, M. Tinkham, and T. M. Klapwijk. Transition from metallic to tunneling regimes in superconducting microconstrictions: Excess current, charge imbalance, and supercurrent conversion. *Physical Review B*, 25(7):4515, 1982.
- [62] T. M. Klapwijk, G. E. Blonder, and M. Tinkham. Explanation of subharmonic energy gap structure in superconducting contacts. *Physica B+C*, 109:1657–1664, 1982.
- [63] M. Octavio, M. Tinkham, G. E. Blonder, and T. M. Klapwijk. Subharmonic energy-gap structure in superconducting constrictions. *Physical Review B*, 27(11):6739, 1983.
- [64] M. B. Shalom, M. J. Zhu, V. I. Fal’ko, A. Mishchenko, A. V. Kretinin, K. S. Novoselov, C. R. Woods, K. Watanabe, T. Taniguchi, A. K. Geim, and J. R. Prance. Proximity superconductivity in ballistic graphene, from Fabry-Pérot oscillations to random Andreev states in magnetic field. *arXiv preprint arXiv:1504.03286*, 2015.
- [65] I. M. Khaymovich, N. M. Chtchelkatchev, I. A. Shereshevskii, and A. S. Mel’nikov. Andreev transport in two-dimensional normal-superconducting systems in strong magnetic fields. *Europhysics Letters*, 91(1):17005, 2010.
- [66] H. Hoppe, U. Zülicke, and G. Schön. Andreev reflection in strong magnetic fields. *Physical Review Letters*, 84(8):1804, 2000.
- [67] U. Zülicke, H. Hoppe, and G. Schön. Andreev reflection at superconductor–semiconductor interfaces in high magnetic fields. *Physica B: Condensed Matter*, 298(1):453–456, 2001.
- [68] V. E. Calado, S. Goswami, G. Nanda, M. Diez, A. R. Akhmerov, K. Watanabe, T. Taniguchi, T. M. Klapwijk, and L. M. K. Vandersypen. Ballistic Josephson junctions in edge-contacted graphene. *arXiv preprint arXiv:1501.06817*, 2015.
- [69] C. W. J. Beenakker. Specular Andreev reflection in graphene. *Physical Review Letters*, 97(6):067007, 2006.
- [70] C. W. J. Beenakker. Colloquium: Andreev reflection and Klein tunneling in graphene. *Reviews of Modern Physics*, 80(4):1337, 2008.

- [71] M. Titov and C. W. J. Beenakker. Josephson effect in ballistic graphene. *Physical Review B*, 74(4):041401, 2006.
- [72] I. Hagymási, A. Kormányos, and J. Cserti. Josephson current in ballistic superconductor-graphene systems. *Physical Review B*, 82(13):134516, 2010.
- [73] E. Sarvestani and S. A. Jafari. Josephson supercurrent in a graphene-superconductor junction. *Physical Review B*, 85(2):024513, 2012.
- [74] H. B. Heersche, P. Jarillo-Herrero, J. B. Oostinga, L. M. K. Vandersypen, and A. F. Morpurgo. Bipolar supercurrent in graphene. *Nature*, 446(7131):56–59, 2007.
- [75] J.-H. Choi, G.-H. Lee, S. Park, D. Jeong, J.-O Lee, H.-S. Sim, Y.-J. Doh, and H.-J. Lee. Complete gate control of supercurrent in graphene p–n junctions. *Nature Communications*, 4:2525, 2013.
- [76] X. Du, I. Skachko, and E. Y. Andrei. Josephson current and multiple Andreev reflections in graphene SNS junctions. *Physical Review B*, 77(18):184507, 2008.
- [77] C. Ojeda-Aristizabal, M. Ferrier, S. Guéron, and H. Bouchiat. Tuning the proximity effect in a superconductor-graphene-superconductor junction. *Physical Review B*, 79(16):165436, 2009.
- [78] I. V. Borzenets, U. C. Coskun, S. J. Jones, and G. Finkelstein. Phase diffusion in graphene-based Josephson junctions. *Physical Review Letters*, 107(13):137005, 2011.
- [79] D. Jeong, J.-H. Choi, G.-H. Lee, S. Jo, Y.-J. Doh, and H.-J. Lee. Observation of supercurrent in PbIn-graphene-PbIn Josephson junction. *Physical Review B*, 83(9):094503, 2011.
- [80] P. Rickhaus, M. Weiss, L. Marot, and C. Schönenberger. Quantum Hall effect in graphene with superconducting electrodes. *Nano letters*, 12(4):1942–1945, 2012.
- [81] W. A. Muñoz, L. Covaci, and F. M. Peeters. Tight-binding study of bilayer graphene Josephson junctions. *Physical Review B*, 86(18):184505, 2012.
- [82] Y. Takane and K.-I. Imura. Quasiclassical theory of the Josephson effect in ballistic graphene junctions. *Journal of the Physical Society of Japan*, 81(9):094707, 2012.
- [83] C. Kittel. *Introduction to solid state physics*. Wiley, 2005.
- [84] M. Octavio, W. J. Skocpol, and M. Tinkham. Improved performance of tin variable-thickness superconducting microbridges. *Magnetics, IEEE Transactions on*, 13(1):739–742, 1977.

- [85] J. C. Cuevas and A. L. Yeyati. Subharmonic gap structure in short ballistic graphene junctions. *Physical Review B*, 74(18):180501, 2006.
- [86] A. V. Galaktionov and A. D. Zaikin. Quantum interference and supercurrent in multiple-barrier proximity structures. *Physical Review B*, 65(18):184507, 2002.
- [87] M. Veldhorst, M. Snelder, M. Hoek, T. Gang, V. K Guduru, X. L. Wang, U. Zeitler, W. G. van der Wiel, A. A. Golubov, H. Hilgenkamp, and A. Brinkman. Josephson supercurrent through a topological insulator surface state. *Nature Materials*, 11(5):417–421, 2012.
- [88] K. Komatsu, C. Li, S. Autier-Laurent, H. Bouchiat, and S. Guéron. Superconducting proximity effect in long superconductor/graphene/superconductor junctions: From specular Andreev reflection at zero field to the quantum Hall regime. *Physical Review B*, 86(11):115412, 2012.
- [89] A. Barone and G. Paternò. *Physics and applications of the Josephson effect*. Wiley, 1982.
- [90] S. Hart, H. Ren, T. Wagner, P. Leubner, M. Mühlbauer, C. Brüne, H. Buhmann, L. W. Molenkamp, and A. Yacoby. Induced superconductivity in the quantum spin Hall edge. *Nature Physics*, 10:638–643, 2014.
- [91] K. Steinberg, M. Scheffler, and M. Dressel. Quasi-particle dynamics in superconducting aluminum. *arXiv preprint arXiv:0712.3391*, 2007.
- [92] R. C. Dynes and T. A. Fulton. Supercurrent density distribution in Josephson junctions. *Physical Review B*, 3(9):3015, 1971.
- [93] D. K. Efetov. *Towards inducing superconductivity into graphene*. PhD thesis, Columbia University, 2014.
- [94] Julien Bordaz. *Proximity-induced superconductivity in single-layer and bilayer graphene*. PhD thesis, Karlsruhe Institute of Technology, 2013.
- [95] B. Wu, C. Shao, S. Chu, B. Schmidt, M. Savard, S. Zhao, Z. Mi, T. Szkopek, and G. Gervais. McMillan-Rowell oscillations in a low spin-orbit SNS semiconducting junction. *arXiv preprint arXiv:1305.5140*, 2013.
- [96] W. J. Tomasch. Geometrical resonance and boundary effects in tunneling from superconducting In. *Physical Review Letters*, 16(1):16, 1966.
- [97] W. L. McMillan and P. W. Anderson. Theory of geometrical resonances in the tunneling characteristics of thick films of superconductors. *Physical Review Letters*, 16(3):85, 1966.

- 
- [98] J. M. Rowell and W. L. McMillan. Electron interference in a normal metal induced by superconducting contacts. *Physical Review Letters*, 16(11):453, 1966.
- [99] O. Neshar and G. Koren. Measurements of  $\Delta$  and  $v_F$  from Andreev reflections and McMillan-Rowell oscillations in edge junctions of  $\text{YBa}_2\text{Cu}_3\text{O}_{6.6}/\text{YBa}_2\text{Cu}_{2.55}\text{Fe}_{0.45}\text{O}_y/\text{YBa}_2\text{Cu}_3\text{O}_{6.6}$ . *Physical Review B*, 60(13):9287, 1999.
- [100] C. Visani, Z. Sefrioui, J. Tornos, C. Leon, J. Briatico, M. Bibes, A. Barthélémy, J. Santamaria, and J. E. Villegas. Equal-spin Andreev reflection and long-range coherent transport in high-temperature superconductor/half-metallic ferromagnet junctions. *Nature Physics*, 8(7):539–543, 2012.